AN ABSTRACT OF THE THESIS OF

Noah T. Matsumoto for the degree of Master of Science in Mechanical Engineering and Wood Science presented on June 20, 2008
Title: The Fracture Toughness of Medium Density Fiberboard and other Fiber Bridging Composites.

Abstract approved:

_____

John A. Nairn & Brian Bay

In many composites, fiber bridging develops as part of the fracture process. Fiber bridging invalidates many toughness evaluation methods such as the ASTM E399 and complicates the identification of crack length, which is a necessary parameter in energy methods. In order to measure the toughness of fiber bridging composites, an energy method was developed, which required the use of digital image correlation (DIC) to measure crack growth. The method showed the mode I fracture toughness of medium density fiberboard (MDF) to be highly dependent on panel density and crack growth orientation. Simply applying the ASTM E399 method on MDF showed the same dependence on crack growth orientation but produced significantly lower values of toughness. The R-curves produced by the developed energy method were used to aid in the development of numerical models of the fracture process in MDF using the material point method (MPM). Specifically, bilinear (triangular) and cubic traction laws were used to simulate the behavior of fiber bridging. The simulations provide a fiber bridging interpretation of the experimental results.

The Fracture Toughness of Medium Density Fiberboard and other Fiber Bridging Composites

by
Noah T. Matsumoto

A THESIS

submitted to

Oregon State University

in partial fulfillment of
the requirements for the
degree of

Master of Science

Presented June 20, 2008
Commencement June 2009

Master of Science thesis of Noah T. Matsumoto presented on June 20, 2008.

APPROVED:

_____

Co. Major Professor, representing Mechanical Engineering

_____

Co. Major Professor, representing Wood Science

_____

Head of the School of Mechanical, Industrial and Manufacturing Engineering

_____

Head of the Department of Wood Science and Engineering

_____

Dean of the Graduate School

I understand that my thesis will become part of the permanent collection……..

_____

Noah T. Matsumoto, Author

ACKNOWLEDGEMENTS

The author expresses sincere appreciation to following people who have made this project possible:

- Professor John Nairn – For providing me the opportunity to work under him and imparting his knowledge and experience.
- Milo Clausen – For supplying his experience, expertise and technical prowess in experimental testing and miscellaneous tasks.
- Professor Lech Muszynski – For guidance and management of the DIC systems.
- Arijit Sinha and Edward Le (my fellow lab and officemates) – for their help in many miscellaneous tasks.
- Flakeboard® – For providing the MDF panels.
- My friends and family – who provide balance and encouragement.

TABLE OF CONTENTS

TABLE OF CONTENTS (Continued)

Page

LIST OF FIGURES

LIST OF FIGURES (Continued)

Figure Page

LIST OF TABLES

TABLE OF APPENDIX FIGURES

TABLE OF APPENDIX FIGURES (Continued)

Figure Page

LIST OF APPENDIX TABLES

1. LITERATURE REVIEW

Composites

A composite is composed of two or more different materials (often very different in chemical and or physical properties) that produce a desired quality not easily obtainable in any one material alone. These qualities could include strength, stiffness, density, cost or toughness. Usually the less rigid material in the composite is called the matrix, while the more rigid material is called the reinforcement. The reinforcement can often take the form of fibers, which are discrete structures with a high aspect ratio (length/width or radius). The relative proportions of matrix and the fiber vary significantly depending on the composite.

Medium Density Fiberboard (MDF)

Medium density fiberboard (MDF) is a wood-based panel product. It is a composite composed of wood fibers held together by a very low quantity of resin (or glue). MDF has only been produced for about 35 years. Its consumption in the United States has increased ten fold in the last two decades and the demand for it is growing 2.6 times faster than all other wood products.

MDF panels are usually manufactured to a density between 500 and 800 kg/m^3. A commonly used wood fiber is pinus radiate, Wang (2001). To obtain fibers, wood is reduced to chips and then thermo-mechanically pulped. The resin, usually urea formaldehyde is added to the pulp in a blowline blending technique, where it (about 8-12 percent by weight) is injected with the fibers in a pressurized tube. They are then dried in a flash tube at high temperature before being formed and pressed into panels.

Before pressing, the fibers are dropped onto a conveyer line. Gravity causes the fibers to lay flat (called lay-down) within the plane of the final panel. The final panel is pressed between two metal platens. Pressing increases the density of the panel and also induces a density profile through its thickness. The density of the faces

is considerably higher than the core, (Wang, 2001). The final panel is usually a rectangular sheet with a thickness between 0.5 and 1 inch.

Having denser and stiffer faces (skins) gives MDF good bending and surface properties without adding significant weight. The skins may also have a higher toughness than the rest of the panel. Additionally, since the wood fibers also lay flat within the panel, anisotropy is expected between the in-plane and out-of-plane properties.

Since MDF is composed of wood fibers and wood is hygrothermal (meaning its properties are dependent on moisture content and temperature), MDF is likely to have the same characteristic. If so, its mechanical properties such as stiffness, strength and toughness will be dependent on moisture content (MC) and temperature. The expected moisture content (EMC) of wood depends on the surrounding temperature and moisture content, Boyer et. al (2003).

Though the stiffness of different MDF panels is commonly evaluated, the same cannot be said about fracture toughness. The inherent way in which MDF fractures makes evaluation of its fracture toughness difficult and will be addressed later in more detail. Once a method has been developed to bypass the problems presented by MDF's post-cracking morphology, other effects such as moisture content and direction dependence can be addressed.

Toughness

Fracture toughness is a material property that determines a material's resistance to the propagation of an existing flaw. Flaws are unavoidable and can develop in manufacturing and from normal use. Even geometric artifacts such corners, holes and other irregularities can be considered flaws. These are all examples of stress concentrators where the local stress (e.g., at the crack tip) is significantly higher than in the rest of the body. The local stress is dependent on the globally applied load, geometry of the structure and the size of the flaw. When a flaw is present, stress is concentrated and the globally defined yield strength of the material is

no longer the governing failure property. Fracture toughness will determine at what applied stress the structure will fail. Even if a material has a higher yield strength, when a flaw is present, the material with the lower fracture toughness may fail first. Here is an illustration of that concept:

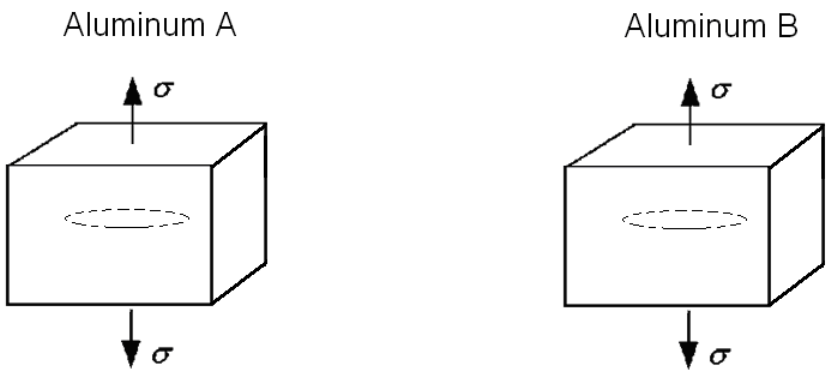

Al Alloy	Stress Max Ideal (σ-max) MPa	K_{IC}	Stress Max w/ crack (MPa)
2014-T651 (A)	485	24	***300***
2024-T352 (B)	470	34	***426***

Figure 1. Illustration of toughness governed failure.

These two aluminum alloys, 2014-T651 (A) and 2024-T352 (B) illustrate the concept. Al A and B have yield strengths 485 MPa and 470 MPa respectively. In an ideal case with no flaws, Al B would fail first at an applied stress 470 MPa. Now if both were subjected to a stress concentrator such as a penny-shaped crack with radius of 5mm, Al A would fail first at 300 MPa even though it has a higher ideal yield strength. It fails first because its toughness (K_{IC}) is lower.

Fracture mechanics defines three different modes of loading in which a crack can propagate: mode I, mode II and mode III (illustrated in Figure 2). These modes are commonly referred to as the crack opening mode, in-plane shear and out-of-plane shear, respectively, Anderson (2005). Mode I fracture is of primary interest because it is the most common way in which cracks propagate. Often cracks initially in other modes will be diverted to become mode I propagation. For example, mode II cracks in homogenous materials typically turn 45^{o} to maximize mode I component.

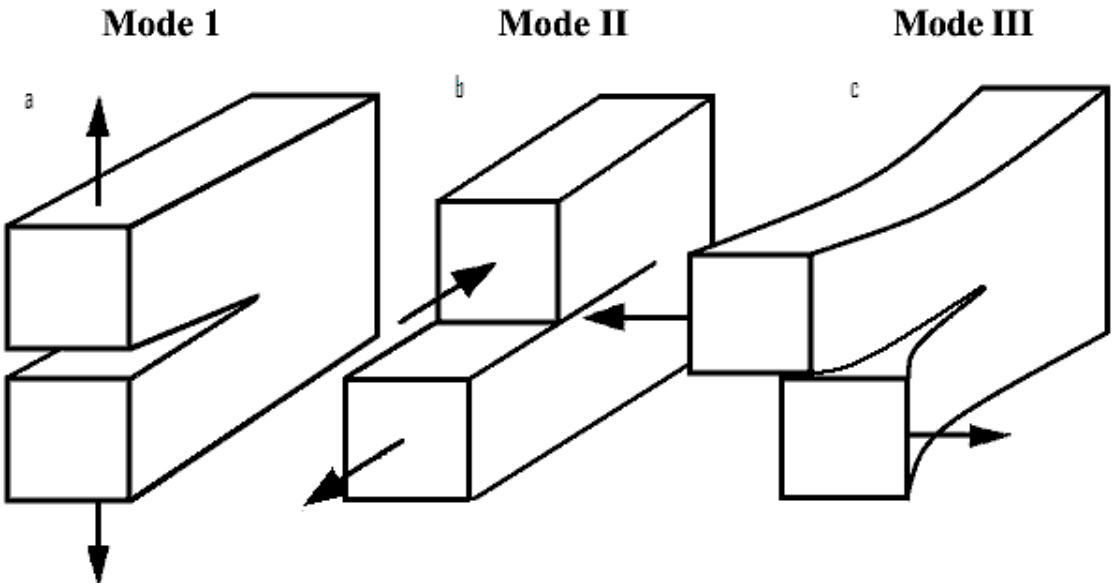

Figure 2. Fracture modes: a. Crack opening mode (mode I), b. in-plane shear (mode II), c. out-of-plane shear (mode III). (Modified from Anderson, 2005)

Stress Distribution around the Crack Tip

Most fracture mechanics problems deal with the mode I (crack opening mode), however in all three cases for a linear-elastic isotropic material, the stress distribution can be described in polar coordinates by

$$\sigma_{ij} = \left(\frac{K}{\sqrt{r}}\right) f_{ij}(\theta) + \sum_{m=0}^{\infty} A_m r_m^{\frac{m}{2}} g_{ij}{}^{m}(\theta) \qquad (1)$$

for a linear-elastic material where σ_{ij} is the stress tensor, r the distance from the crack tip and θ the angle between the line of the crack tip and the direction of r (see figure 3), K is the stress intensity factor, f_{ij} and $g_{ij}{}^{m}$ are dimensionless functions of θ (Anderson (2005), Westegaard (1939), Irwin (1957), Sneddon (1946) and Williams (1956)). If we are interested in stresses near the crack tip, the first term in the series solution is singular and dominates (as r $\rightarrow$0). For example, in mode I, the stress distribution,

$$\sigma_{yy} = \left(\frac{K_I}{\sqrt{r}}\right)\cos\left(\frac{\theta}{2}\right)\left[1+\sin\left(\frac{\theta}{2}\right)\sin\left(\frac{3\theta}{2}\right)\right] \quad (2)$$

where *yy* is the direction normal to the crack (see Figure 3).

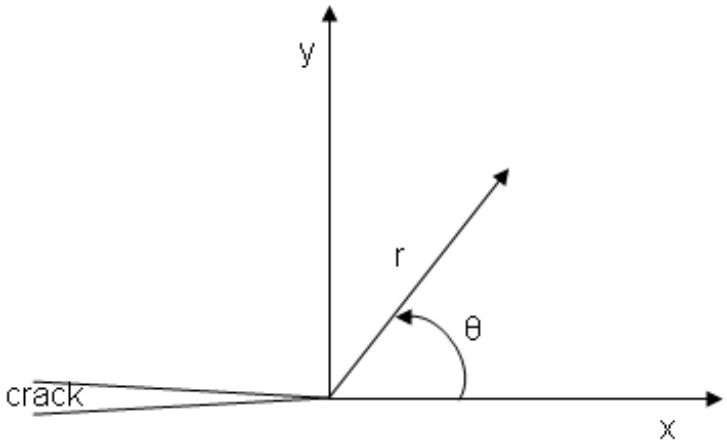

Figure 3. Coordinate system for crack tip stress distribution.

Methods for evaluating fracture toughness can be divided into two distinctive approaches: 1) the *stress intensity methods* and 2) the *energy methods*.

Stress Intensity Method

Stress intensity toughness for a linear-elastic material can be obtained through material testing using the ASTM E399 standard. The standard requires the measurement of peak load, P_{max} (or the intersection of 5% lower secant line, $P_{5\%}$) from displacement controlled loading of a fracture specimen. One of the most commonly used fracture specimen geometries is the called the compact tension specimen (CT specimen) (see Figure 4). Applying the peak load value into the corresponding mathematical stress intensity solution for the specimen geometry produces a stress intensity toughness (factor) for the material (called K_{IC} for mode I). General K_{IC} calculations follow the form:

$$K_{IC} = \frac{P_{\max}(\cap P_{5\%})}{B \cdot w} \cdot Y(a/w) \cdot \sqrt{a} \tag{3}$$

where P_{max} is the maximum load (or the intersection of 5% lower secant line, $P_{5\%}$), B is the specimen thickness, w is the crack-line width, a is the initial crack length, and $Y(a/w)$ is an associated calibration function for specimen geometry and loading conditions (note that the ASTM $f(a/w) = Y(a/w)*(a/w)^{1/2}$).

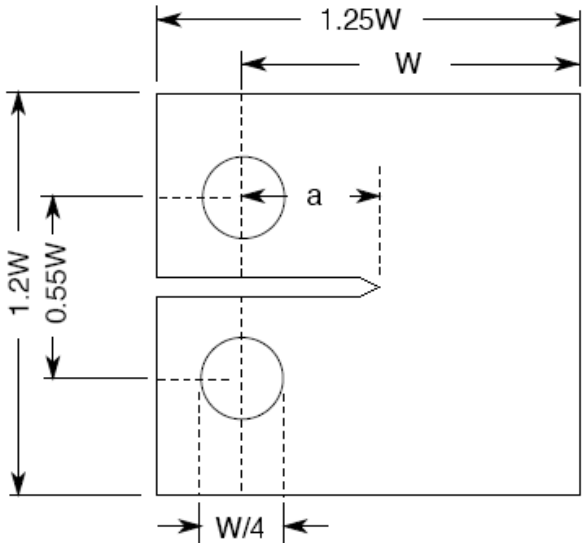

Figure 4. ASTM compact tension specimen with loading pin holes.

Calibration functions for specific geometries are obtained by numerical methods such as finite element analysis or boundary collocation (Gross, et. al, 1964) using the Williams stress function.

The ASTM E399 standard specifies the use of a specimen in *plane-strain* and *small-scale yielding* conditions which can be satisfied by

$$B, a, (w-a) \geq 2.5\left(\frac{K_{IC}}{\sigma_y}\right)^2 \tag{4}$$

(ASTM E399, 2006). Plane-strain and small-scale yielding conditions serve to limit the amount of plasticity near the crack tip.

Stress intensity toughness is a quantitative measure of how a material handles concentrated stresses. Materials with low stress intensity factors do not tolerate stress concentrations well. Using a material's stress intensity factor (K_{IC}), the required stress for failure of a specimen can be evaluated using the associated stress intensity solution for that geometry and loading conditions (i.e., solving for load, P in eqn 3).

Energy Methods

The energy approach to quantifying toughness is predicated on the principle that crack extension will occur when the energy available for crack growth is sufficient to overcome the material's inherent crack resistance. First proposed by Griffith (1920), it is essentially a thermodynamic energy balance

$$-\frac{\partial \Pi}{\partial A} = \frac{\partial Ws}{\partial A} \tag{5}$$

where Π is the potential energy supplied by the internal strain energy and external forces, W_s is the work required to create new surfaces and A is the crack area. It states that in order for crack growth to occur, the available potential energy released must be large enough to overcome the surface energy of the material. In an experiment this potential energy is usually supplied by the loading machine and stored in the chemical bonds until the force becomes large enough that the material can no longer hold it at which time cracking proceeds.

Irwin (1956) adapted Griffith's theory and defined what is called the strain energy release rate,

$$G = -\frac{\partial \Pi}{\partial A} \tag{6}$$

which is the rate of change of total potential energy (Π) with respect to crack area (A). At the precise moment of fracture, $G=G_c$ (G_{IC} in mode I) the critical energy release rate, which is a measure of toughness. During fracture experiments, a specimen will

be loaded, but until fracture occurs there is no change in area; yet the potential energy continues to increase as the load is applied. G is a measure of Π that would be released if the crack were to grow. It is not until cracking actually occurs that the critical release rate is realized where a drop in potential energy will induce the creation of surface area.

For crack propagation in any material, the strain energy release rate can also be determined from

$$G_C = \frac{W}{Area} = \frac{W_f}{B \cdot \Delta a} \tag{7}$$

where W_f is the energy used for creating the new surface, B is the specimen thickness, and Δa is the increment of crack growth associated with the energy consumption. The amount of fracture energy will depend on the material and how much crack growth is represented. An example of fracture energy is depicted in triangular area enclosed by the load-displacement curve (see Figure 5).

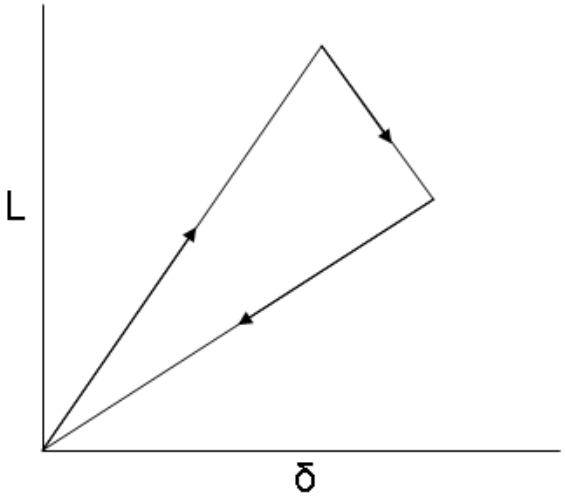

Figure 5. Fracture energy from a load-displacement curve. This is a specific case for a linear-elastic material with no plasticity where the fracture energy is the area enclosed by the triangle.

Since toughness is an intrinsic material property, similitude must exist between the energy, G_{IC} and stress intensity K_{IC} toughness. They are related via the relationship

$$G_{IC} = \frac{K_{IC}^{\ 2}}{E'} \tag{8}$$

where *E'* is the effective modulus, which depends on the stress state, Anderson (2005). For plane-strain conditions $E' = E/(1-\nu^2)$; for plane stress $E' = E$.

Compliance

The compliance of a specimen is merely the inverse of its stiffness. It is generally measured from an unloading curve. For a linear-elastic material with little plastic deformation, the compliance at any point in the load-displacement curve is defined as:

$$C = \frac{\delta}{P} \tag{9}$$

where δ is the displacement and P is the associated load. The compliance is useful in determining if cracking has initiated as well as in the evaluation of toughness. As the crack length increases, compliance will increase because the newly cracked portion of the specimen no longer contributes to carrying load, and the stiffness decreases.

Compliance vs. crack length measurements of any linear-elastic specimen with negligible plasticity can be used to determine its strain energy release rate using linear-elastic fracture mechanics (LEFM) as follows:

$$G_{IC} = \frac{P^2}{2B}\frac{dC}{da} \tag{10}$$

(Smith, 2003) for displacement controlled loading where P is the applied load, B is the thickness of the sample, and dC/da is the change in compliance with respect to crack length. Unlike the ASTM E399 method, it does not a require a specific calibration function, $Y(a/w)$, which depends on the specimen and loading geometry. Using this definition of G_{IC}, the general ASTM E399 definition of stress intensity toughness (eqn 3) and the relationship between G_{IC} and K_{IC}, a connection between compliance and the stress intensity calibration function is developed for materials governed by LEFM:

$$Y^2(a/w) = \frac{1}{2a \cdot C_o} \frac{dC(a/w)}{d(a/w)} \tag{11}$$

where $C_o = 1/(BE'w)$ and E' is the effective modulus (Matsumoto et. al, 2007). If the ASTM stress intensity approach for evaluating the toughness of a specific material is valid, it must obey this relationship.

Unloads are useful in measuring compliance. They can also show the correct energy to use in the evaluation of fracture toughness in eqn 7. Unloading curves show how much elastic energy remains in specimen after some increment of crack growth. A material that plastically deforms during fracture testing will have an unloading curve that does not return to the origin even if no cracking has occurred (though the compliance would not change). If crack growth has occurred and curves return to some residual displacement D (see Figure 6), the energy associated with that increment of crack growth (W_f) is enclosed by the loading and unloading curve ABCD. If the curve comes back to the origin (in the case of no plasticity), then the correct energy is enclosed by ABC (see Figure 6).

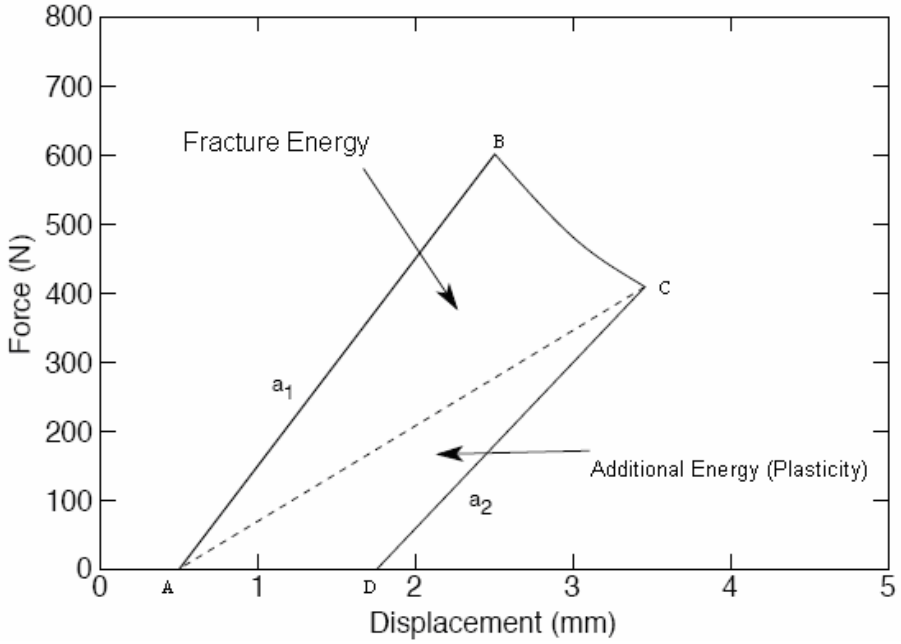

Figure 6. Possible loading and unloading curves, which defines the appropriate energy of fracture.

Fiber Bridging

In fiber bridging composites such as medium density fiberboard (MDF), methods for evaluating toughness have not been well established. Fiber bridging is a form of contact bridging which alters the expected stress distribution around the crack and can increase the actual failure load (S. Morel, 2003). During the fracture of fiber bridging composites, failure of the matrix material may proceed ahead of fibers which have not yet failed (fiber bridging) and therefore continue to carry stress (Ehart et. al 1999). Fiber bridging makes a universal definition of the crack tip difficult. The stress function (eqns 1, 2) is invalidated by fiber bridging even if the material is linear-elastic, because they assume stress-free crack surfaces. A non-visual technique to measure the crack length common in metals is electrical resistance, but this is impossible because of the low electrical conductivity of the material (ibid). Additionally, unloading to measure compliance (useful in the evaluation of toughness) maybe unreliable because bridging may interfere with the closure of specimens.

There are many models which try to account for the effects of fiber bridging in fracture mechanics. A simple bridging model suggests that the total stress,

$$K_T = K_Q + K_B \tag{12}$$

where K_T is the total resultant stress, K_Q is the intrinsic toughness at the crack tip and K_B is the stress contribution from fiber bridging (Smith, 2003). However, this is not useful in modeling or experimentation unless the magnitude of K_B is known. K_B can be dependent on crack extension/opening displacement.

Fiber Bridging and Compliance

An unloading curve of a fracture specimen may not return to the origin (even if cracking has not initiated); in metals the cause is usually plastic deformation, however the reason maybe different in fiber bridging materials. Fibers bridging may prevent complete closure by creating additional resistance between the two crack surfaces. In this case, a perfectly linear-elastic material would appear to have large amounts plasticity, and the measured compliance would be incorrect.

The unloading curve of a specimen can either: 1) return to the origin for materials with negligible amounts of plasticity, 2) return to some positive displacement in the case of plasticity or crack plane interference or 3) return to some other displacement if the specimen had various types of internal stresses (residual stresses). If an unloading curve returns at some positive displacement, to distinguish between plasticity and crack plane interference, a test proposed by Atkins and Mai (1988) can be used. In the test, the fiber bridging zone is removed before unloading. If the unloading curve now returns to the origin, fiber interference is the cause of the offset displacement. This offset is the result of resistance (friction and smashing) from the fibers to closure. As a result, the unloading curve is not a measure of compliance. However, if the curve continues to return at a positive offset, the cause is plasticity.

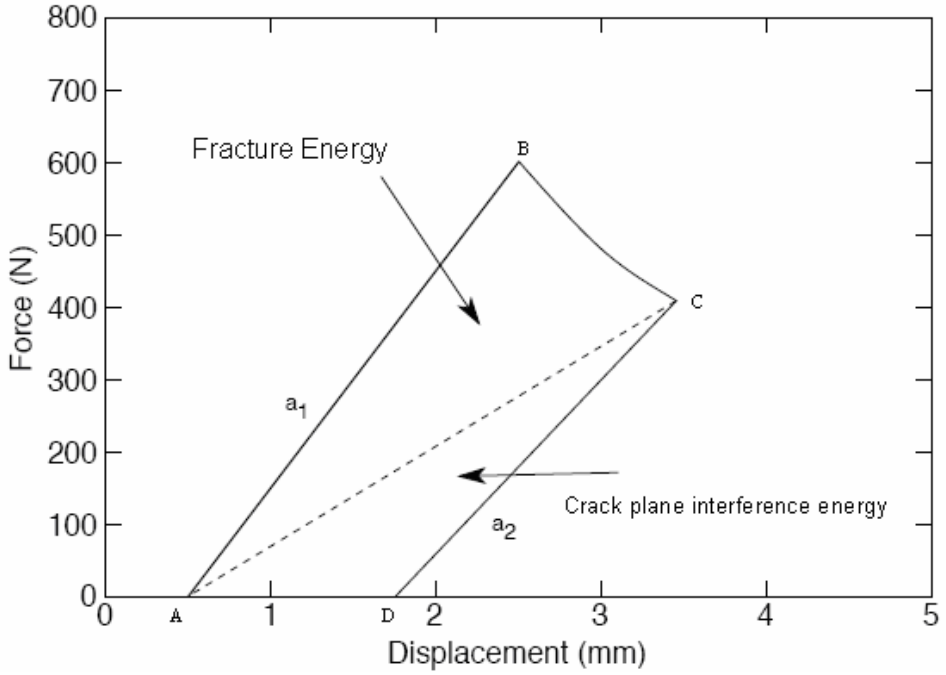

Figure 7. Typical behavior of a fiber bridging composite with crack-plane interference rather than plasticity. Here a_1 and a_2 represent the loading and unloading curves respectively, while the dashed line represents the unloading curve after removal of the process zone.

If the material is linear-elastic with no plasticity effects, the compliance is still simply described by eqn 9, and eqn 10 can be used to determine its strain-energy release rate. In the case of a linear-elastic material without plasticity (but may have crack plane interference) the correct energy envelope should be the one enclosed by ABC in load-displacement curve, see Figure 7, rather than the total area between ABCD.

Fracture Toughness of MDF

Since MDF is a fiber bridging composite, it poses all of the previously mentioned challenges related to its fracture morphology, but attempts have been made to evaluate its fracture toughness. Using the stress intensity method (using the ASTM E399 standard), Niemz et. al, (1999) obtained stress intensity factors (K_{IC}) for MDF and other wood composites. They tested MDF, OSB (parallel and perpendicular to the

strands) and chipboard and found their K_{IC} values to be 1.81, (1.25 and 2.08) and 0.68 $MPa\sqrt{m}$, respectively.

The problem with the use of the ASTM E399 method in fiber bridging composites is that it assumes a material with self-similar crack growth with stress-free fracture surfaces. In self-similar crack growth, the only changing physical characteristic is the actual crack length. Fiber bridging violates these assumptions because stress is carried across crack surfaces, and the crack process zone (region around the crack tip) changes. It invalidates the *Y(a/w)* calibration function which is specimen and loading geometry dependent. With the addition of fiber bridging, the specimen geometry has essentially changed because load carrying material now exists behind the crack tip.

Energy methods for evaluating fracture toughness are not necessarily invalidated by fiber bridging. They can account for fiber bridging. A simple energy method developed by Larson and Gustafsson (Nordtest Method (1993) see Figure 8 for specimen specifications) was used by Morris et. al (1999).

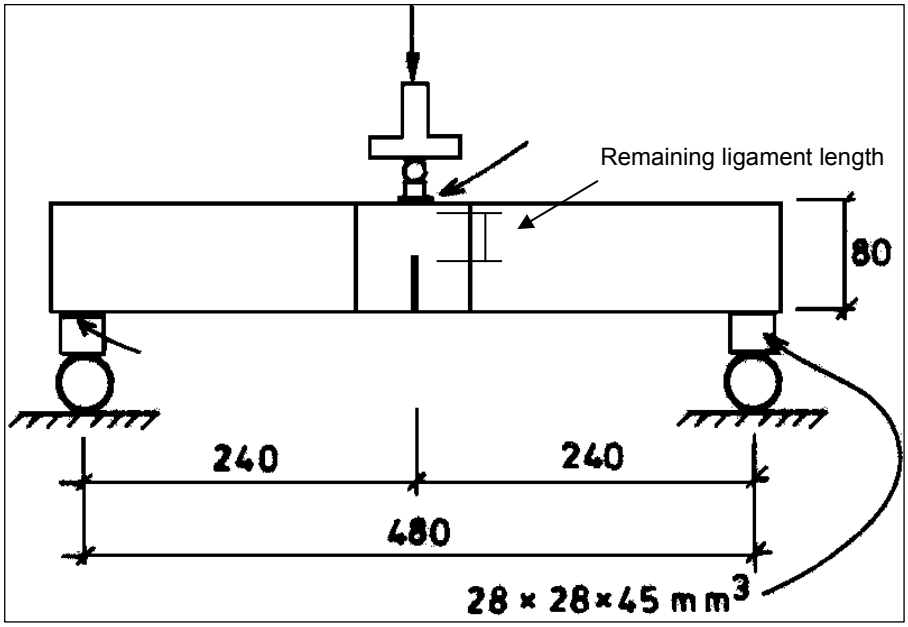

Figure 8. Nordtest specimen. Taken from Nordtest, 1998.

A crack notched was machined half way through the height of the edge-notched specimen (half the ligament length). By applying a load at the opposite end of the notch (producing bending in the specimen), the crack was propagated through the remaining ligament length. Toughness was calculated using the definition analogous to eqn 7. The energy for fracture (W_f) was evaluated by integrating the total area under the load-displacement curve. While, the associated crack growth (Δa), was the total ligament length minus the initial crack notch. They obtained a G_{IC} of 5918 J/m^2 for MDF of density 800 kg/m^3 (conditioned at 20% relative humidity).

The Nordtest (1993) method used by Morris (1999) produces only a single measurement of toughness for each specimen. This value is essentially an average of the apparent toughness between initial crack notch and the final crack length (thickness of the specimen). However, it does consider the likely variation in toughness as the crack approaches the end of the specimen. Edge effects may affect their average. Incremental toughness (toughness as function of crack length) must be measured in order to determine if variation occurs, which is not possible with the Nordtest.

Another energy method purposed by Ehart et. al (1997) evaluated the toughness of particleboard (similar to MDF in fiber bridging) incrementally using their wedge splitting specimen. They first noted that the process-zone (the region in front and behind the crack tip) varies for different crack extensions, but at some critical extension, the fiber bridging reaches equilibrium and any successive crack extension has the same process-zone. At equilibrium, a portion of fiber bridging (at the initial notch) no longer has any load carrying capacity because the fibers have completely broken (see Figure 9). That is, once the separation between the crack surfaces at the mouth became larger than the length of the fibers, they no longer had influence, and a steady-state of fiber bridging was reached.

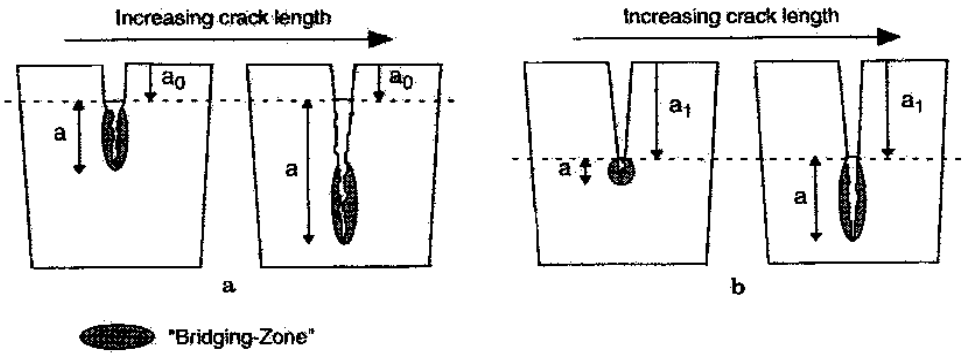

Figure 9. Cracks with different contributions from fiber bridging. a. Cracks with equivalent contributions. b. Crack lengths with different contributions. (Ehart, 1996)

Instead of evaluating the fracture toughness using a single specimen, they used multiple specimens with different notch depths each with the equilibrium amount of bridging. Since the load-displacement curves of particleboard (similar to MDF) were found to be non-linear, toughness measurements were made using the area between shifted superimposed load-displacement curves with different starting notch depths. The un-shifted, plots are displayed in Figure 10.

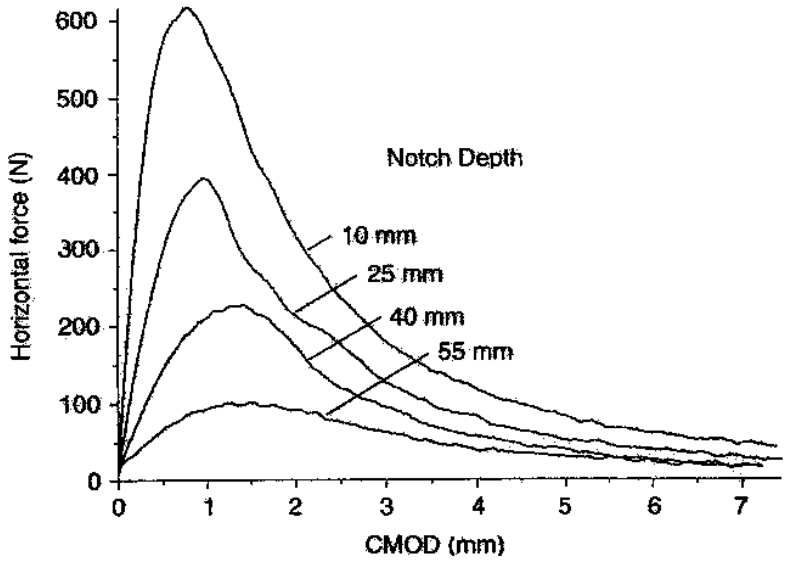

Figure 10. Load-displacement curves for various notch depths. (Ehart et. al, 1996)

The superimposed load-displacement curves were then shifted horizontally to achieve coincidence (see Figure 11). The various shifts were justified by the varying size of the plastic region for cracks of different notch depths. The energy associated with fracture was then determined as the area between the load-displacement curves of the different notched depths (see Figure 11).

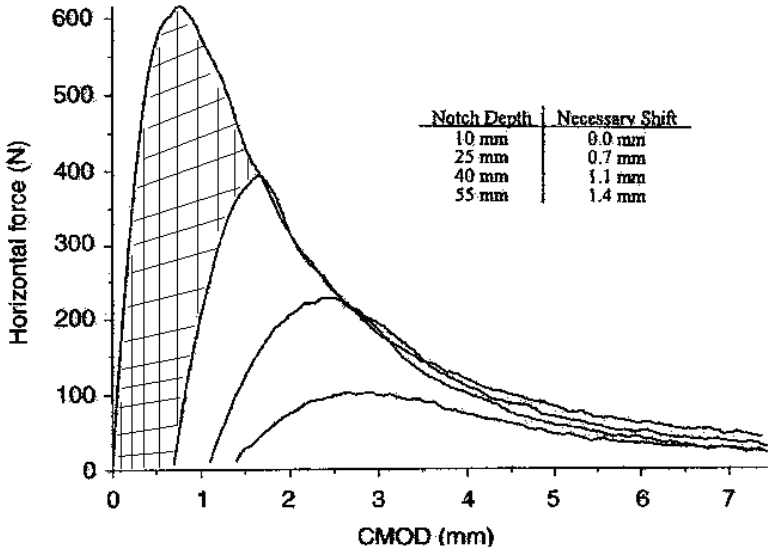

Figure 11. Shifted curves to account for differences in plasticity at various notch depths. The shaded area represents the fracture energy between a notch of 10mm and 25 mm. (Ehart et. al 1996)

Since, bridging prevents the identification of a crack length, effective crack lengths were used. Effective crack lengths were determined using finite element analysis (FEA). An effective crack length was the necessary crack length for a linear-elastic specimen with a distinct crack tip to have the same load carrying capacity. Using effective crack lengths and the associated energies from the superimposed curves (Figure 11), G_{IC} was evaluated for particleboard in crack propagation directions perpendicular and parallel to the plane of the panels. They were found to be 2930 and 240 J/m^2 respectively.

Though the method of Ehart et. al (1997) produces a incremental toughness, it is weak because of its use of effective crack lengths and in its assumption that a steady state fiber bridging zone is reached quickly. Their effective crack lengths are based in

linear-elastic non-fiber bridging analysis using FEA. However, their analysis does not consider fiber bridging which is a significant property of the particle board and MDF. They also assume the fiber bridging in their material reaches equilibrium, but have no quantitative method of confirming it. Ideally, actual crack lengths should be measured and not assumed; and a method should not have to assume that steady state fiber bridging is reached.

Digital Image Correlation

Digital image correlation (DIC), sometimes called electronic speckle photography (Sutton, 1983), or digital image processing (Samarasinghe, 1999) is a method of making full field strain or displacement measurements without contacting the specimens. It can be a useful tool in solving the difficulties in crack length identification.

A DIC system consists of a set of two digital cameras (to capture stereo images) and image processing software (such as VIC-3D® produced by Correlated Solutions®). The cameras are placed in front of the desired specimen at some angle (see Figure 17) which provides depth perception (denoted by the z-direction). Stereo images are captured either through manual triggering or at a specified rate during loading. Using the DIC software, local displacements (u,v,w) are calculated through the shift in maker positions between undeformed and deformed images. From data of local displacements, full-field strain measurements can be defined over the selected area of analysis by differentiation.

The theory behind DIC correlation is quite complex and can vary slightly based on the manufacturer of the system. The basic principles however are the same. First, the specimen to be imaged must have a random light intensity pattern (Thuvander (2000), Sutton (1983), Smarasinghe (2000)) to provide a unique set of points to track. If specimens do not have surfaces conducive to DIC imaging; patterns must be applied. This is accomplished by spraying black dots (with spray paint) or sprinkling black toner (Thuvander, Smarasinghe) onto their surfaces. If the original surface is too dark, the contrast between the black dots and surface can be poor.

Contrast can be improved by painting the surface a flat white before applying the black dots (see Figure 15).

Once the specimen is ready to be imaged, it is placed in the position prior to deformation. A digital image must first be captured in the undeformed state (called a base image). All strain and displacement measurements are made relative to this base image. After deformation (or during the deformation process) another image is taken. The base image and a single deformed image are compared to calculate displacements and strains by the DIC image processing program.

To calculate displacements and strains, image processing programs such as VIC-3D® (in the case of Correlated Solutions® system) are used. Their methods are explained well by Sutton (1983). First, both light intensity distribution of the base and deformed image are stored in arrays as a set of numbers or gray scale values. Bilinear or bicubic interpolation is performed on the data to represent it in continuous form. This interpolation allows points to be mapped between pixels, and therefore provides resolution higher than a single pixel. The representative array for the base image and deformed image is broken down into subsets. A random subset array from the base image is compared to all the subset arrays in the deformed image. Through least squares minimization, a subset in the deformed array is chosen and the associated displacement is tabulated. This process is repeated for all the subsets in the base image to obtain a displacement field. Strain fields are then calculated by taking the gradient of the displacement fields.

Using DIC, Samarasinghe (2004) obtained stress intensity factors for wood in the tangential-longitudinal opening mode using their measured displacement fields. Sih et. al (1965) developed a displacement field model for a perfectly orthotropic linear elastic material as a function of the materials stress intensity factor K_I. Using the experimentally measured displacement fields from DIC, Samarasinghe solved for the associated stress intensity factors. However, no such displacement model currently exists for fiber bridging composites such as MDF, and therefore this sort of evaluation of toughness is not possible for such materials.

Resistance Curves

Many materials exhibit an increase in toughness with crack length called a resistance curve. This resistance can occur for a variety of different reasons which include an increase in fracture energy due to the development of plasticity, the development of fiber bridging or surface roughening (Morel, 2003) and or specimen geometry. In these cases the materials toughness or critical energy release rate, G_{IC}, is defined as the steady state value where the resistance curve is constant with respect to crack length, Anderson (2005). If the time required to reach steady state is long, the rising portion of the resistance curve is significant and can be used to model the failure of finite sized specimens.

Finite Element Analysis

Finite element analysis (FEA) is the use of the finite element method (FEM) to solve physical and mathematical problems. FEM is usually governed by the principle of minimum potential energy which says that when an object deforms it will take the shape that minimizes the total potential energy. FEA proves its usefulness in structural problems with complex geometries where analytical or closed form solutions are not obtainable. If analytical solutions are obtainable (usually a product of ordinary differential equations), they are valid for any location in the system (Logan, 2000). Where FEA differs is in it reliance on a system of linear algebraic equations representative of small quadrilateral elements in a continuum. Each of the smaller, simpler elements with its own boundary conditions is represented by an equation and is solved in system with the rest of elemental equations.

FEA gives good results for static analyses and is ok for simple fracture mechanics simulations. It does not however work well for more dynamic systems, usually involving large displacements (requiring a re-meshing) or more complicated fracture mechanics models involving bridging. A more flexible numerical approach is the material point method (MPM), (Nairn, 2003).

Material Point Method

The material point method (MPM) sometimes called particle-in-cell (PIC) method is a finite element method using discreet uniform particles rather than quadrilateral elements. MPM is better suited for mechanical problems involving large deformations such as crack propagation because it requires no re-meshing after each iterative cycle (Nairn, 2003). Each particle created in the initial geometry retains information on the state of the calculation (properties such as position, velocity, stress, etc.) throughout the simulation through a Lagrangian background grid. The grid provides a platform to solve the governing dynamic equations while tracking particle properties.

Cracks and Fiber Bridging in MPM

Since MPM does not require the use of meshing and the particles are free to move on the chosen grid, it lends it self to use in fracture modeling (Nairn, 2003). In MPM, cracks are introduced by explicitly defining a series of connected crack particles. The crack tip is assigned a tip toughness $J_{tip,c}$. Since the crack particles translate through the background grid along with the material points and retain information about local stresses, fracture mechanics properties such as J-integral and stress intensity factors can be calculated (Nairn, 2008).

One method of simulating fiber bridging is through tractions laws. There are many tractions laws; two examples are bilinear and cubic, which are found in the NairnMPM source code. In principle they simulate bridging by applying an additional force/stress on crack particles based on the crack opening displacement (COD). The magnitude of the traction force for a given COD depends on the specified traction law. Once the COD exceeds some defined critical displacement, the traction breaks and no longer applies a force.

2. INTRODUCTION

The fracture toughness of a material predicts how well it will perform with a flaw or stress concentrator. When a structure contains a stress concentrator such as a hole, corner, crack or some other irregularity, failure is no longer governed by yield stress but rather by fracture toughness. The material with the lower fracture toughness will fail first, even if it has a higher yield strength. (For an illustration, see section I. Literature Review.) Thus, fracture toughness of materials is needed to perform valid and complete design analyses for structures with flaws.

Mode I crack propagation is the most studied fracture mode because it occurs most often in the real-world. Even cracks in the other two modes will often turn to convert into mode I loading (Anderson, 2005). The stress and strain distribution around the crack tip for linear-elastic materials is well defined (Irwin, 1957) but not for cracks with fiber bridging because of the unknown and variable influence of the bridging.

During the fracture of a fiber bridging composite, failure of the constituent materials does not occur simultaneously. Crack propagation may proceed with only a partial failure of the material behind the crack tip (see Figure 11).

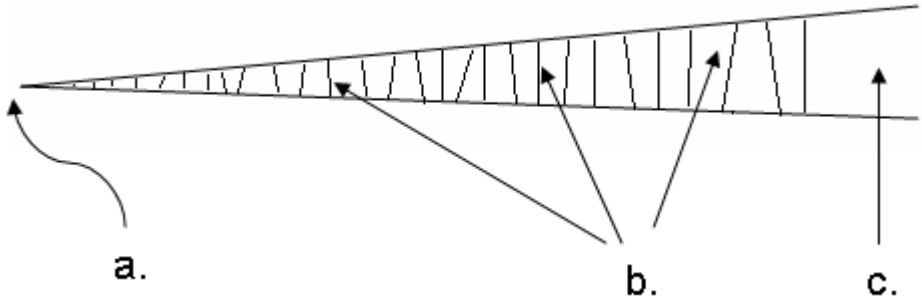

Figure 12. Representation of fiber bridging. a. actual crack tip. b. fiber bridging (incomplete failure). c. no fiber bridging (complete failure).

Left behind the crack tip are often fibers that have not completely failed and therefore continue to carry stress (Ehart et. al, 1999). They increase the failure load, and when they eventual fail, can contribute to toughness. The fracture toughness of fiber

bridging composites, such as medium density fiberboard (MDF), has not been evaluated appropriately likely because of the inherent complications bridging presents.

Fiber bridging obscures the crack tip making direct measurement of the crack-length difficult. A non-visual technique to measure the crack length common in metals is electrical resistance, but this method is impossible in many composites because of their low electrical conductivity (Ehart et. al, 1999). Another way to evaluate toughness is through measurement of compliance (obtained by unloading) at different crack lengths. However, fiber bridging might change the unloading response making it no longer an accurate measure of compliance (Atkins, et. al, 1988). A method that truly measures fracture toughness must consider the effects of fiber bridging while overcoming all the inherent challenges it poses.

Stress Intensity Factors

Using one of a number of specific specimens, the ASTM E399 method (2006) for evaluating fracture toughness produces a stress intensity factor, K_{IC} based on the maximum load during the testing procedure. It has been used to evaluate the fracture toughness of fiber bridging composites such as MDF, particle board, and OSB (Niemz, et. al, 1997 & 1999). However, the ASTM method assumes self-similar crack growth and stress-free surfaces. Fiber bridging violates these assumptions. See section 1. Literature Review and Matsumoto et. al, 2007 for more details.

Energy Methods

Energy methods can account for the effects of fiber bridging in their evaluation of fracture toughness, because the measured fracture energy carries information about the fiber bridging. Energy methods measure the strain energy release rate (G_{IC}) and are of the form

$$G_{IC} = \frac{W_f}{B \cdot \Delta a} \tag{13}$$

where W_f is the energy consumed in fracture, Δa is the associated crack growth and B is the specimen thickness. In fiber bridging materials, fracture energy, W_f can usually be obtained from load-displacement curves, but the change in crack length, Δa, is more of a challenge to evaluate for the reasons previously mentioned.

Using the Nordtest (Larsen et. al, 1993), an energy method, Morris et. al (1999) calculated the strain energy release rate for different densities of MDF at different moisture contents. The Nordtest specimen is a single edge notched specimen loaded in three-point bending until complete propagation of the crack through to the opposite edge (see section 1. Literature Review). They obtained a G_{IC} for MDF (with a density of 800 kg/m^3 conditioned at a moisture content of 20%) of 5918 J/m^2. The Nordtest method did not require the measurement of crack length during anyone point in the test and gives only an average toughness along the length of the specimen, ignoring possible edge effects of the specimen.

A more complicated energy method was used by Ehart et. al (1996) to evaluate G_{IC} of particleboard, which is similar to MDF but with much coarser wood components. They first noted that the process/bridging-zone (region in front of and behind the crack tip) varies for different crack extensions, but at some critical extension, the fiber bridging reaches equilibrium where any successive crack extension has an identical process-zone. At equilibrium, a portion of fiber bridging (at the initial notch) no longer has any load carrying capacity because the fibers have completely failed. Instead of evaluating the fracture toughness using a single specimen, they used multiple specimens with different notch depths each with the same characteristic equilibrium bridging length. Their individual load-displacement curves were superimposed on one another and shifted horizontally to achieve coincidence. The energy associated with fracture between any two crack lengths was the enclosed area between their associated curves. Since, bridging prevents the

identification of a crack length, effective crack lengths were used. An effective crack length was the necessary crack length for a linear-elastic material with a distinct crack tip to have the same load carrying capacity (which was modeled by finite element analysis).

Using effective crack lengths and the associated energies from the superimposed curves, G_{IC} was evaluated for particleboard in crack propagation directions perpendicular and parallel to the plane of the panels. They were found to be 2930 and 240 J/m^2 respectively. The use of effective crack lengths to measure toughness, however, gives an effective material property.

Use of Digital Image Correlation

A useful tool when direct measurement of crack length is not possible is digital image correlation (DIC). Stress intensity factors for wood in the tangential-longitudinal opening mode have been obtained using DIC (Samarasinghe, 2004). For a perfectly orthotropic linear-elastic material, the displacement field is a function of the stress intensity factor, K_{IC} (Sih et al., 1965). The displacement field was experimentally measured using DIC, and therefore a K_{IC} could be calculated. Unfortunately, a displacement field model does not exist for fiber bridging composites, and thus, this type of analysis is not possible. However, the displacement/strain field obtained by DIC may be used in another fashion to overcome some of the obstacles presented by fiber bridging in determining crack length.

Numerical Modeling

Numerical modeling is a potential means to better understand the fracture mechanics in materials. The material point method (MPM) is best suited for mechanical problems involving crack propagation because it requires no re-meshing as the crack length changes (Nairn, 2003). In MPM, cracks are introduced by explicitly defining a series of connected crack particles. The crack tip is assigned a tip toughness $J_{tip,c}$. Since the crack particles translate through the background grid along

with the material points and retain information about local stresses, fracture mechanics properties such as J-integral and stress intensity factors can be calculated (Nairn, 2008).

One method of simulating fiber bridging in MPM is through tractions laws. There are many tractions laws; two examples are the bilinear and cubic, which are found in the NairnMPM source code. In principle they simulate bridging by applying an additional force on crack particles based on the crack opening displacement (COD). The magnitude of the traction force for a given COD depends on the specified traction law. Once the COD exceeds some defined critical displacement, the traction breaks and no longer applies a force, analogous to breaking bridged fibers.

Goals

In the literature, no universally accepted method exists for evaluating fracture toughness of fiber bridging composites. Many methods are based on assumptions about the material which are not valid even though they may produce reasonable results. The goals of this study were to:

1. develop a valid energy method to evaluate the fracture toughness of fiber bridging composites such as MDF
2. evaluate the toughness of different densities of MDF in various material directions
3. determine the magnitude of the error associated with using the ASTM E399 stress intensity method on MDF and potentially on other fiber bridging composites
4. use the R-curves produced by the developed method to numerically simulate the effect of fiber bridging in the fracture process using the material point method

3. MATERIALS AND METHODS

Fracture Specimens

Fracture testing was performed on MDF specimens analogous to the ASTM E399 compact tension specimen (see Figure 13)

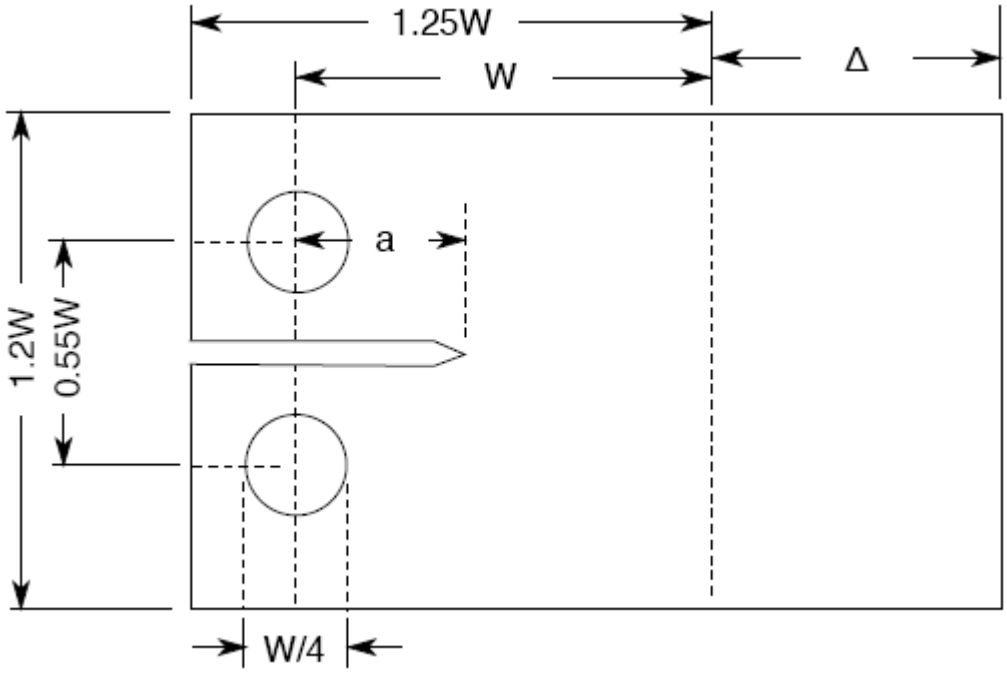

Figure 13. Extended compact tension specimen

where a =1.2" (30.48 mm), W=3" (76.2 mm), and Δ=1.25" (31.75mm). A Δ of zero is the ASTM CT specimen, but here a non-zero Δ was used to make more room from crack propagation. An Eplison® clip gauge-style extensometer was placed at the center loading line of the pin holes with two small steel pins to measure displacements. Two densities of MDF panel (4x8 ft) at two different thicknesses, B of 0.5" (12.7mm) and 0.75" (19.05mm) were obtained from Flakeboard® (Springfield, OR) at densities of 38 and 46 lbs/ft^3 (609 and 737 kg/m^3 respectively). Prior to testing, all panels were conditioned at 20^{o}C and 65% relative humidity until equilibrium. Periodic measurements of specimens' weights were made to determine equilibrium which was confirmed by stabilization of the weights.

Due to the manufacturing process of MDF, fiber alignment and a density profile through the thickness was expected. Therefore, fracture specimens were created at various orientations in the panel (see Figure 14).

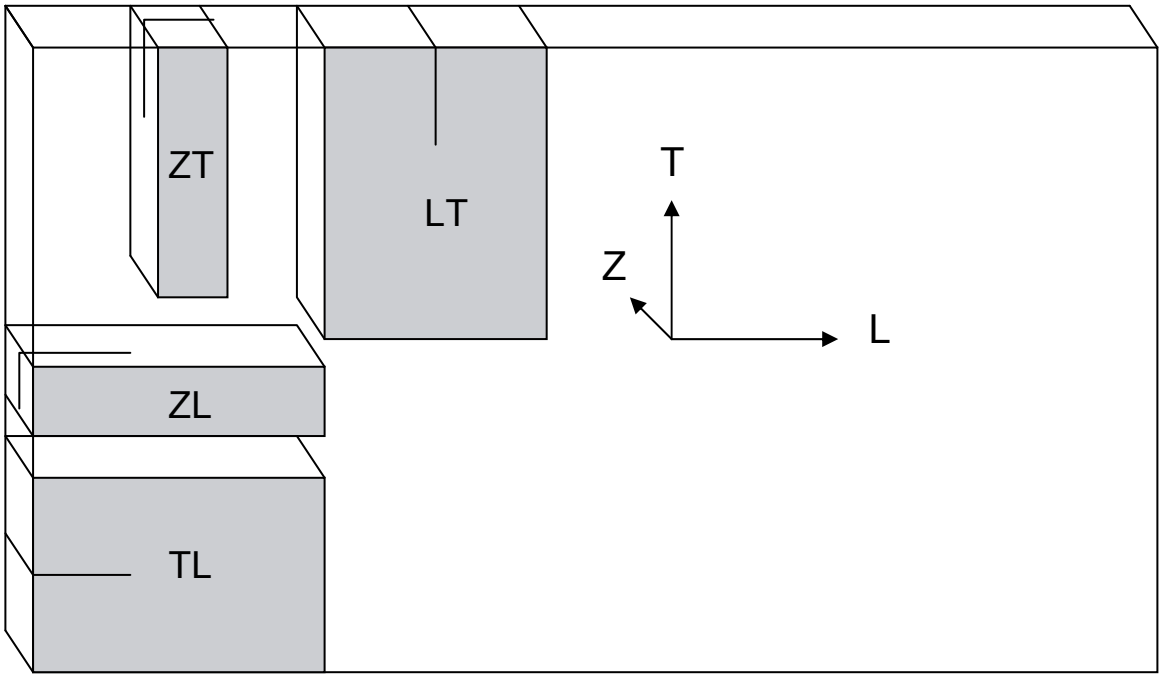

Figure 14. Example MDF panel with various specimen orientations. Note: not to scale.

Fracture specimens were created in the TL, LT, ZT and ZL directions where the second letter, (e.g. "L" in TL) represents the intended crack propagation direction and the first letter (e.g. "T" in TL) represents the direction perpendicular to the crack surface. To differentiate between the 0.5" (12.7 mm) and 0.75" (19.05 mm) specimen thicknesses, a "t" is added at end of the crack propagation nomenclature for the 0.75" thickness specimens. (A TLt specimen has a thickness of 0.75" while a TL has thickness of 0.5".) For specimens with the intended crack surfaces perpendicular to the z-direction (ZT and ZL), the specimen heights were limited to the thickness of the panel (either ½ or ¾"). To create the CT geometry (referring to Figure 14), these strips were glued between two other pieces of MDF and then cut to size. The remaining

orthogonal cracking directions, LZ and TZ were not tested, because the z-direction is short and does not allow for crack propagation experiments.

In order to perform an analysis of specimens using DIC, their surfaces must have a unique set of visual markers with good contrast relative to their background. Such a surface was created by applying a layer of flat-white spray paint and then covering it with a random pattern of black dots using flat-black spray paint (see Figure 15).

Figure 15. Specimen with random speckle pattern

Loading Experiments

A load-displacement curve was obtained from each fracture specimen through displacement controlled loading on a Sintech® loading machine at a rate of 0.5 mm/min (based on machine crosshead displacements). The load was measured using a Lebo2K® load cell with a resolution of ±2.5 N. (See Matsumoto, 2008 Figure 1B in Appendix B for fixture details).

Evaluating Toughness

Stress Intensity Methods

Using a compact tension specimen, the ASTM E399 method produces stress intensity factors for linear-elastic material and is of the form:

$$K_{IC} = \frac{P_{\max}(\cap P_{5\%})}{B \cdot w} \cdot Y(a/w) \cdot \sqrt{a} \qquad (14)$$

where P_{max} is the maximum load (or the intersection of 5% lower secant line, $P_{5\%}$), B is the specimen thickness, w is the crack-line width, a is the initial crack length, and $Y(a/w)$ is an associated calibration function for the specimen geometry and loading conditions (note that the ASTM $f(a/w) = Y(a/w)*(a/w)^{1/2}$). Here the quantity a/w represents normalized crack length, where a is the crack length and $w = W + \Delta$. From load-displacement curves, P_{max} was obtained and used to produce a K_{IC} for all specimens using a $Y(a/w)$ for the extended CT specimens developed from finite elements (which is described in the Results and Discussion). To use this stress intensity approach requires the specimen to be in plane-strain and have small-scale yielding. These conditions are satisfied by equation 4. An additional requirement, often over looked, are stress free surfaces. This condition is not met if bridging is present and will be discussed further in Results and Discussion.

Energy Methods

Energy methods can potentially be used to evaluate the fracture toughness of fiber bridging composites. An extra task in energy methods is that they rely on knowing the crack length of the specimen at various points in the test. See section 1. Literature Review.

For a linear-elastic material whose unloading curves return to the origin after crack growth (see Figure 16), G_{IC} can be defined by:

$$G_{IC} = \frac{W_f}{B \cdot \Delta a} \tag{15}$$

where B is the thickness, Δa is the crack growth and W_f is the energy of fracture which can be written as:

$$W_f = U_j P_i - U_i P_j \tag{16}$$

where P_i is the failure load, u_i is the failure displacement and a_i is the crack length (see Figure 16)

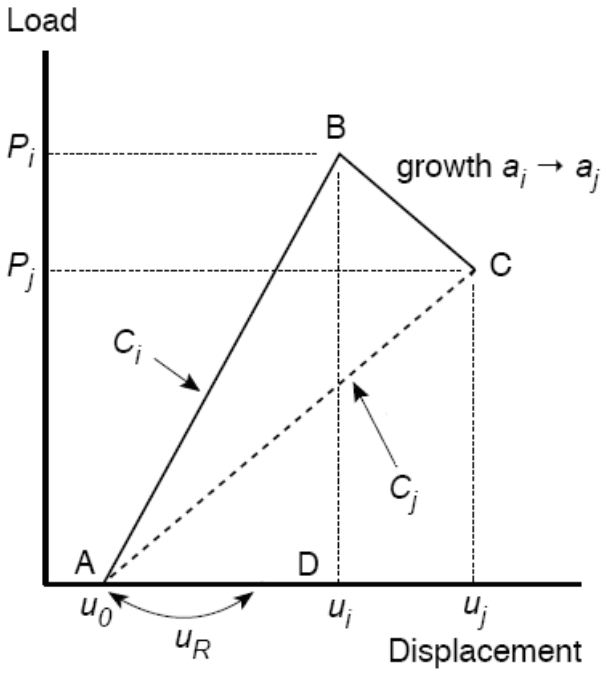

Figure 16. The load-displacement curve for a single loading and unloading envelope. CA (the dotted line) is the unloading line and defines the energy. ABC defines the energy consumed in crack growth from a_i to a_j.

or

$$W_f = P_i P_j \cdot (C_j - C_i) \tag{17}$$

where C is the compliance (see Figure 16) for a linear-elastic material without plasticity. The subscript i denotes the values at crack length a_i, while the j denotes the results at some successive crack length a_j. In the limit of small crack growth, this last form reduces to the well known linear-elastic fracture mechanics result:

$$G_{IC} = \frac{P^2}{2B}\frac{dC}{da} \tag{18}$$

Anderson, 2005.

Unloading Experiments

For a linear-elastic material with negligible plasticity, unloading curves after crack initiation should return to the origin. In MDF, they did not (see Results and Discussion for more details). If unloading curves do not return to the origin, there are three possible reasons: 1) plasticity 2) residual stresses or 3) crack plane interference (see section 1. Literature Review for further explanation). A test proposed by Atkins and Mai (1988) was necessary to distinguish between these three cases. First, a specimen was loaded at a rate of 0.5 mm/min until the crack had propagated through roughly half of the previously un-cracked ligament length and the loading paused. Then, the process zone, area in front of and behind the crack tip was removed using a combination of a small saw, razor blade and drill. The area in front and behind the crack tip along the crack line was drilled out using a 1/8th inch bit and the remaining bridging material was cut out by making small cuts with a razor blade and saw.

In an attempt to make a comparison between displacement offsets of unloading curves with and without the fiber bridging zone using the same specimens (in order to insure the same amount of cracking had occurred), modified unloading tests were performed. In these tests the crack was allowed to propagate through roughly half the available crack line (a/w = 0.64) before being unloaded slightly to show unloading stiffness and projected offset. The specimens were then returned to its displacement

(before the partial unload), the fiber bridging zone removed and then unloaded completely.

Since the unloading curves of various MDF specimens returned close to the origin after removal of the process-zone, a linear-elastic material without plasticity effects was assumed (see Results and Discussion). In which case, the compliance at any crack length a_i, is simply u_i/P_i, and the G_{IC} equation (eqn 10) for linear-elastic material with negligible plasticity is valid. However, the problem of crack identification caused by fiber bridging is still unsolved and will be addressed with DIC.

Regardless of material behavior, G_{IC} toughness and K_{IC} stress-intensity factors are related by:

$$G_{IC} = \frac{K_{IC}^{\ 2}}{E'} \tag{19}$$

(Anderson, 2005), where *E'* is the effective modulus which equals $E/(1-\nu^2)$ for plane-strain conditions or E for plane-stress conditions.

Digital Image Correlation (DIC)

Digital image correlation (DIC), sometimes called electronic speckle photography (Sutton, 1983), or digital image processing (Samarasinghe, 1999) was used to solve the crack identification problem. A DIC system such as the Correlated Solutions® version consists of a set of two digital cameras to capture stereo images and proprietary image processing software, VIC-3D®. Before testing two Dolphin® digital cameras (1024x1024 pixels), part of the Correlated Solutions® system, were positioned approximately 1.5 ft from the fracture specimen in the loading position (see Figure 17) at the angle necessary to fill each camera's imaging area fully with the specimen. Each camera was carefully focused using markers on the specimen as a guide. The aperture of each camera was adjusted such that the intensity and distribution of light entering each camera were roughly equal. After careful focusing

and adjustment of the cameras the specimen was removed from the loading position so that the image analysis software VIC-3D® could be calibrated (see Appendix A for a description of the process).

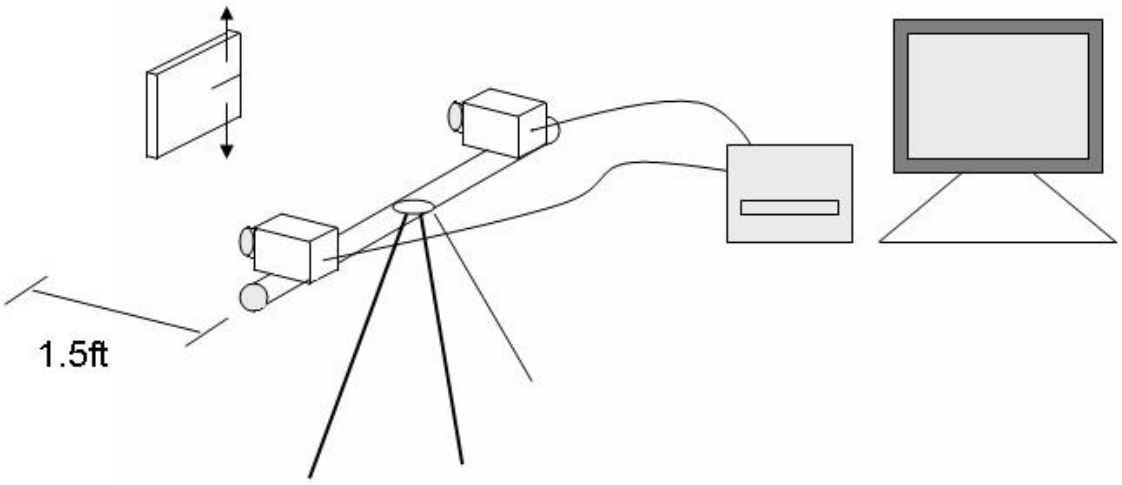

Figure 17. DIC setup.

Crack Growth from DIC

Once calibrated, the DIC software VIC-3D® is able to calculate the displacement field of a specimen at any point during loading with a corresponding image. A strain field is obtained by differentiation of the associated displacement field. The displacement field is calculated by comparing the loaded and unloaded specimen images. The amount of crack growth between any two loading points was determined by the shift between their associated strain fields in front of crack tip.

Using the software, first a reference image, called a base image with the unloaded specimen was selected. Using the software tooling, a quadrilateral area of interest (aoi) was chosen on the specimen in order to reduce computation time and define the region to be analyzed. Finally, the rest of images of the specimen throughout loading, called the deformed images, were selected for comparison with the base image for calculation of each of their respective strain fields.

A number of strain plotting tools were available in the VIC-3D® software. One was a line-plotter, which plots the values of strain for a selected line on the base image for all of the deformed images. Figure 18 shows the axial strain (ε_{yy}) in the direction of loading along the crack-line for a series increasing crack lengths (from left to right). The strain profiles along the un-cracked line were high near the crack tip and decreased as function a distance away from the perceived crack tip. Identifying an absolute crack tip was impossible due to various artifacts near the perceived crack tip, but between two images a Δa could be obtained from the shift in the strain profile along the crack-line. This Δa was used in the evaluation of toughness.

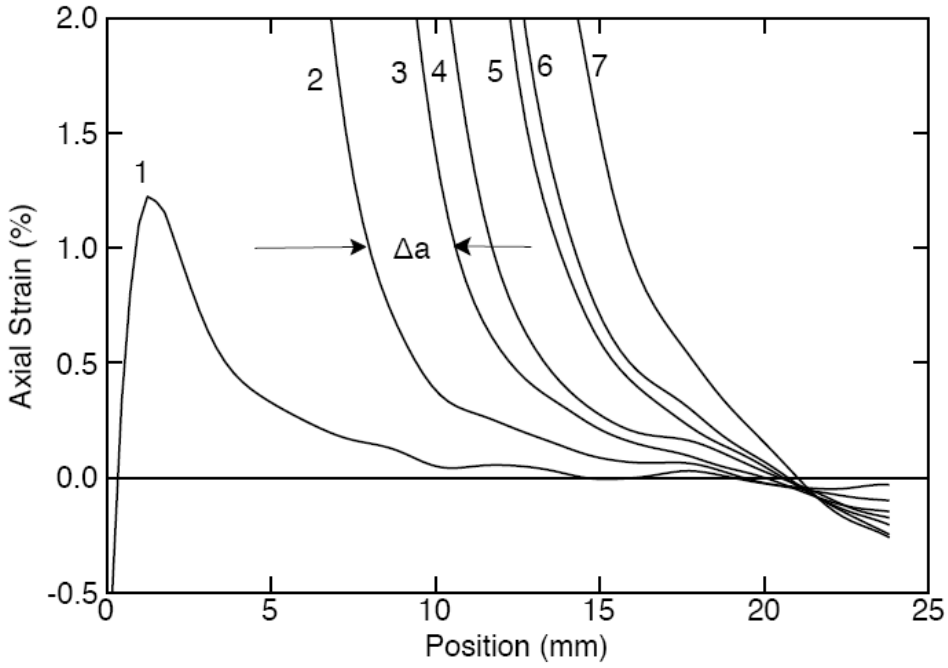

Figure 18. Strain profiles. Axial strain (ε_{yy}) as a function of position along the crack-line obtained from DIC. The associated shift between curves is analogous to crack growth.

Toughness vs. Crack Length (R-curves)

G_{IC} vs. crack length (R-curves) were obtained by using eqn 15 for multiple sets of loading points (P_i, P_j) from a single specimen's load-displacement data (represented in Figure 19) and then plotting those values as function of crack length. The associated crack growth, Δa for a set of load points was calculated using DIC in

the method previously described using the corresponding image set, (I_i,I_j). Loads and images were correlated through the time of the test.

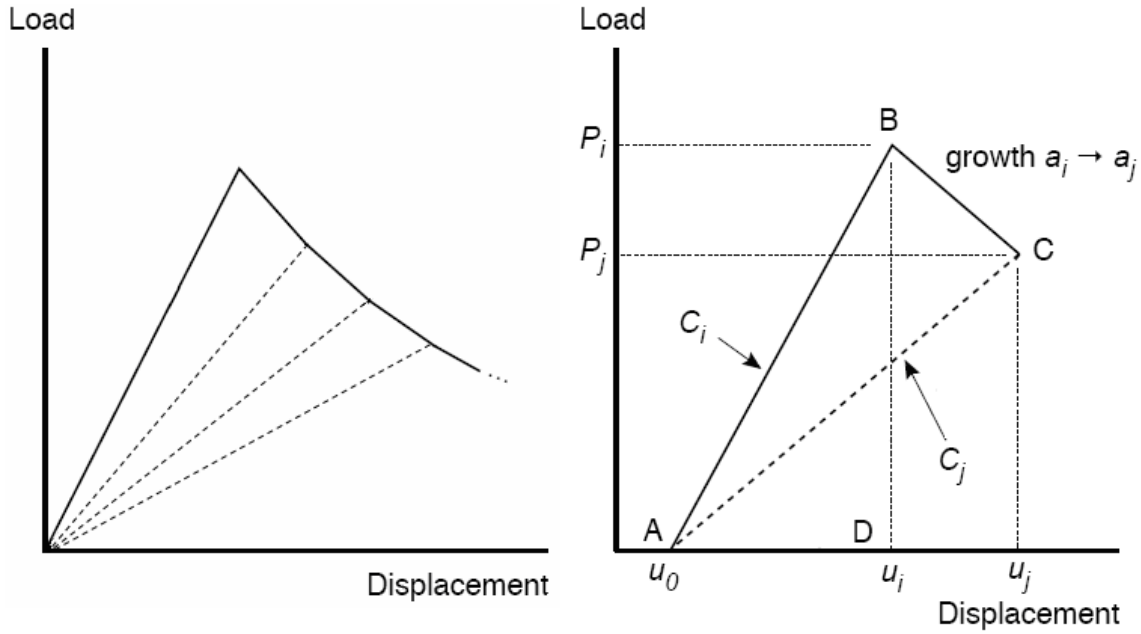

Figure 19. Load-displacement energy envelopes. Left: An example load-displacement curve with multiple energy envelopes used calculate R-curves. Right: The load-displacement curve for single loading and unloading envelope. CA (the dotted line) is the assumed unloading line and defines the energy.

Cumulative R-curve Method

Often the calculation of G_{IC} requires division by a small Δa. Division by a small number produces scatter in the data. As a crack approaches the end of specimens, the increment of crack growth between data points becomes progressively smaller and causes scatter in the associated R-curve data. A revised area method reduces some of the noise by eliminating the need to divide by Δa (Nairn, 2008). First, load and crack length vs. displacement data sets are obtained in the previously described fashion. Next, the cumulative energy released per unit specimen thickness, B is developed by integrating force displacement data, $F(x)$ up to some displacement, d represented by

$$U(d) = \frac{1}{B}\left(\int_0^d F(x)\cdot dx - \frac{1}{2}F(d)\cdot d\right) \tag{20}$$

and graphically represented by Figure 20.

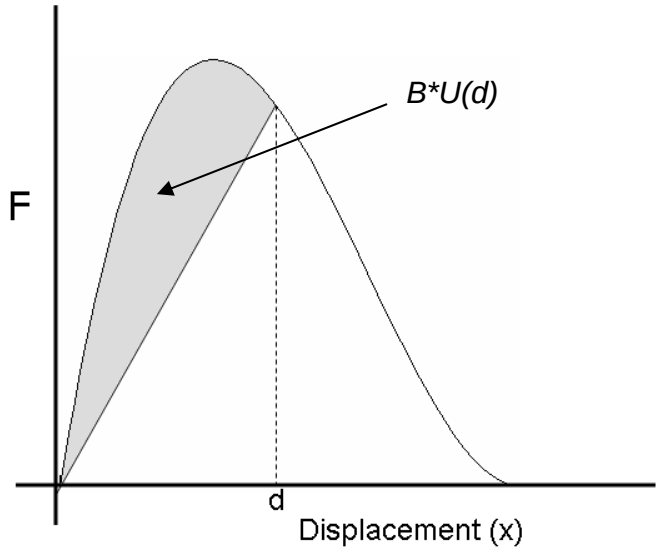

Figure 20. Graphical representation of *U(d)*.

Using *U(d)* and *a(d)* as parametric functions of displacement, the cumulative energy is re-plotted as a function of crack length giving *U(a)*. Finally, the R-curve is obtained by differentiating *U(a)*, where

$$R = \frac{dU(a)}{da} \tag{21}$$

Compliance & Calibration Function relationship

Using the general definition of K_{IC} (eqn 14), the relationship between K_{IC} and G_{IC} (eqn 19) and the general compliance definition of G_{IC} (eqn 18), a connection between compliance as a function of crack length, *C(a/w)* and the geometry dependant calibration function, *Y(a/w)* is developed:

$$Y^2(a/w) = \frac{1}{2a \cdot C_o} \frac{dC(a/w)}{d(a/w)} \tag{22}$$

where $C_o = 1/(BE'w)$ and E' is the effective modulus (Matsumoto et. al, 2007). It shows that the change in compliance as function of crack length and the calibration function for a particular specimen are related to each other by effective modulus and are both independent of the material's toughness.

ASTM comparison

The ASTM E399 method (ASTM, 2006) has been used to evaluate the stress intensity toughness (K_{IC}) for MDF (Neimz, 1998). However the fiber bridging that occurs in crack propagation implicitly violates the conditions for its validity, namely stress-free surfaces and steady-state crack propagation. But depending on the composite, the error could be insignificant and produce even conservative values. This assessment was made in MDF by applying the ASTM approach and converting those K_{IC} values to G_{IC} values (using eqn 19) and comparing them to those produced by the energy method.

To apply the K_{IC} method (eqn 14) for the extended CT specimen, its geometry dependent $Y(a/w)$ calibration was calculated using compliance vs. crack length data from finite element analysis (FEA). First a mesh of the extended CT geometry was created using an isotropic material (E = 2300MPa and v = 0.33) using NairnFEA, a FEA package (http://oregonstate.edu/~nairnj/). $C(a/w)$ points were calculated using the total strain energy, where compliance is defined as:

$$C(a/w) = \frac{2 \cdot U_s}{P^2} \tag{23}$$

and

$$U_s = \frac{1}{2} P \cdot \delta \tag{24}$$

is the total strain energy which was calculated by the code. An applied load at the pins, *P* was arbitrarily selected at 171.01 N (or 1MPa over the pin area). Repeating this process for different values of *a/w* gives *C(a/w)* data points. Those points were then fit to a polynomial and polynomial differentiated with respect to *a/w* to solve for the *Y(a/w)* using eqn 22.

Converting K_{IC} values (using eqn 19) required the specimen's effective modulus, *E*'. Instead of measuring modulus and poisson's ratio in separate tests, an effective modulus of a specimen was measured from the load-displacement curves already measured for the energy method. First, the compliance at the initial crack notch ($a/w^* = 0.282$), $C(a/w^*)_{Ex}$ was calculated from the linear region of the loading slope. $C(a/w^*)_{Ex}$ is simply a linear function of the geometry and the effective modulus which can be seen by solving eqn 22 for *dC(a/w)*, integrating with respect to *a/w*, and evaluating it at a/w^*. And thus,

$$C(a/w^*) = \frac{2}{B \cdot E'} \int Y^2(a/w) \cdot (a/w) \cdot d(a/w)\Big|_{a/w^*} \tag{25}$$

Instead integrating $Y^2(a/w)$, $C(a/w^*)$ was calculated for an arbitrary effective modulus (2300MPa/(1-0.33^2) using FEA (in the same method previously described). This compliance, $C(a/w^*)_{FEA}$ also obeys eqn 25. Dividing $C(a/w^*)_{FEA}$ by $C(a/w^*)_{Ex}$ the exp experimental effective modulus, E'_{Ex} can be found as function of the known parameters and the experimentally measured compliance, $C(a/w^*)_{Ex}$. Therefore,

$$E_{Ex}{}' = \frac{C(a/w^*)_{FEA} \cdot B_{FEA} \cdot E_{FEA}{}'}{C(a/w^*)_{Ex} \cdot B_{Ex}} \tag{26}$$

Determining when ASTM E399 is reasonable

A convenient way to tell if the ASTM method is valid for a particular material is to directly compare its experimental *dC/d(a/w)* data to the expected function obtained by solving eqn 22 for *dC/d(a/w)* using the appropriate *Y(a/w*) for the specimen geometry (Matsumoto et. al, 2007). Experimental *C(a/w)* data points were obtained from MDF specimens without unloading by again assuming a linear-elastic material with negligible plasticity. Therefore

$$C(a/w) = \frac{\delta_{a/w}}{P_{a/w}} \tag{27}$$

where the $\delta_{a/w}$ and $P_{a/w}$ are the displacement and load respectively at some crack length *a/w*. The *C(a/w)* data was measured at multiple values of *a/w*, fit to a polynomial and then differentiated for comparison with the expected *dC(a/w)/d(a/w)*.

Material Point Method (MPM)

The NairnMPM material point code package (http://oregonstate.edu/~nairnj/) was used to model crack propagation and fiber bridging in MDF. First the extended CT geometry was constructed from material points of 1.5mm. A series of connected crack particles were placed at the location of the initial crack line. The specified crack tip was given a tip toughness, $J_{tip,c}$ and bridging toughness, J_B which will be explained in more detail later. During the test, the J integral, J_{tip} is continually calculated, and when $J_{tip} \geq J_{tip,c}$, the crack tip is allowed to propagate. Propagation was modeled by adding an additional crack particle half a cell directly ahead of the previous crack and designating it as the new crack tip. Each new particle was initialized with the selected traction law to model fiber bridging.

A traction simulates fiber bridging by applying an additional stress to the crack particles. It applies a stress in the opposite direction of the crack opening

displacement. The magnitude of stress applied by the traction is related to its opening displacement (Δ) and the specified traction law. Once the Δ exceeds some defined critical displacement, δ_c the traction breaks and no longer applies additional stress to the crack particle. Two traction laws were considered, a bilinear (or triangular) and a cubic traction law.

A bilinear traction law is represented by

$$\sigma(\Delta) = \sigma_{\max} \cdot \frac{\Delta}{\delta} \tag{28}$$

for $\Delta \leq \delta$, and

$$\sigma(\Delta) = \sigma_{\max} \cdot \frac{\delta_c - \Delta}{\delta_c - \delta_{\max}} \tag{29}$$

for $\delta \leq \Delta \leq \delta_c$ (Nairn, 2008). A graphical depiction is presented in Figure 21.

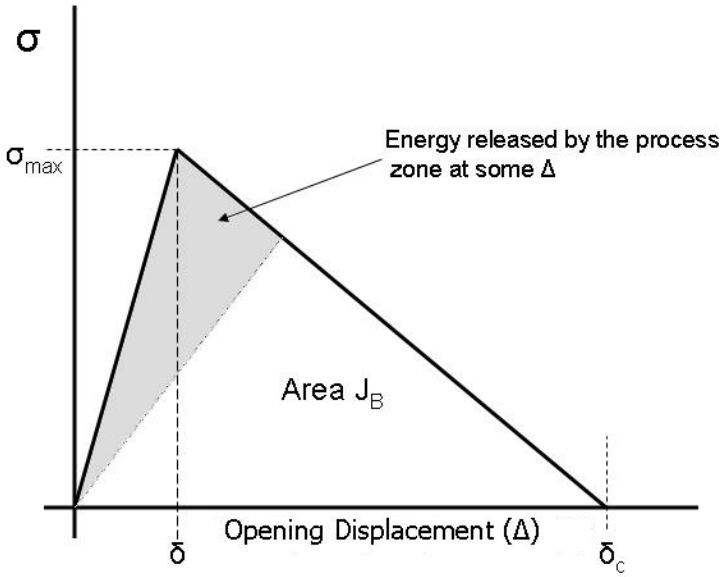

Figure 21. A graphical representation of bilinear traction laws. J_B is the specified toughness of the traction; σ_{max} is the maximum stress, and δ is the corresponding traction opening displacement, Δ. At Δ's larger than δ, energy is available for crack propagation (as an example the shaded region). The area enclosed by curve is the total strain energy available at steady-state crack propagation (J_B), which is reached when the Δ is at δ_c.

A bilinear traction model assumes no strain energy is available for crack propagation until the Δ reaches δ or equivalently when $\sigma = \sigma_{max}$ (see Figure 21). Until that point, all the energy in the tractions (process zone) is recoverable which can be seen if the traction is unloaded (which is assumed to the origin). After the Δ reaches δ, the traction does contribute to the strain energy released during crack growth. Again, unloading is assumed to the origin and the area of the enclosed envelope is the energy available for crack propagation (see Figure 21). This can be thought of as a softening regime with elastic damage mechanics (Nairn, 2008). The traction fails completely at $\Delta = \delta_c$, and energy available for crack growth is J_B or the total enclosed area.

The cubic traction law used is represented by:

$$\sigma = \frac{27 \cdot \sigma_{\max}}{4} \cdot \frac{\delta}{\delta_c}\left(1 - \frac{\delta}{\delta_c}\right)^2 \tag{30}$$

where

$$\sigma_{\max} = \frac{16 \cdot J_B}{9 \cdot \delta_c} \tag{30a}$$

and

$$\delta = \delta_c / 3 \tag{30b}$$

A cubic traction law is analogous to the bilinear one with a few slight differences. First, from the instant a cubic traction applies a stress to a crack particle, it can contribute energy for crack propagation. If a cubic traction is unloaded (assumed to the origin) at any point in displacement, it always shows some non-recoverable energy, which is the available strain energy for crack growth, and is calculated in the total energy release rate, G_{IC} (see Figure 22).

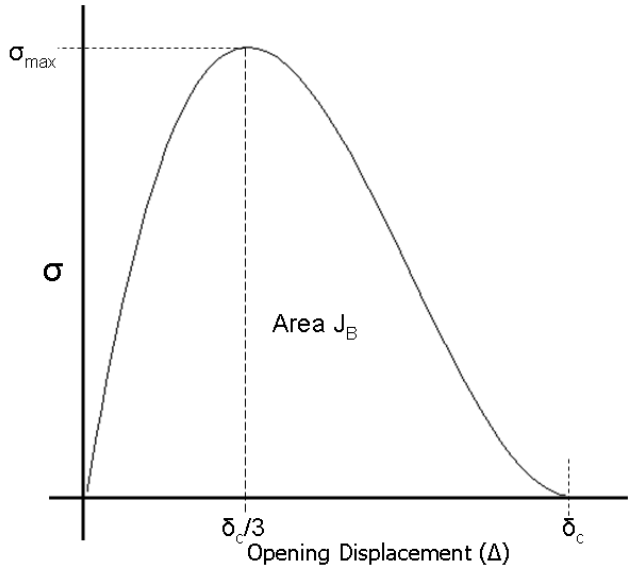

Figure 22. Representation of cubic traction laws. J_B is the specified toughness of the traction; σ_{max} is the maximum stress, and δ is the corresponding traction opening displacement, Δ which is defined as $\delta_c/3$. The area enclosed by curve is the total strain energy available at steady-state crack propagation, which is reached when the Δ is at δ_c.

In both the linear and cubic traction models, the J "toughness" associated with the bridging tractions is the area under the curve (from the origin to δ_c) called J_B. When steady-state crack propagation is reached in either model, the total toughness, G_{IC} is the sum of the tip toughness, $J_{tip,c}$ and the traction toughness J_B. Before the steady-state, the total toughness is equal to $J_{tip,c}$ plus some portion of J_B dependent on traction law and Δ (Nairn, 2008) as previously described. In general, the numerical G_{IC} R-curve can be represented as:

$$R = J_{tip,c} + \int_0^{\Delta_n} \sigma(\Delta) \cdot d\Delta - \frac{1}{2}\sigma(\Delta_n) \cdot \Delta_n \tag{31}$$

where σ is traction stress as a function of the traction opening displacement (Δ), and Δ_n is the Δ at the evaluation point (Nairn, 2008).

4. RESULTS AND DISCUSSION

Experimental Measurement of Toughness

Independent Behavioral Unloading Experiments

MDF extended CT specimens were loaded, allowed to crack, and then unloaded. Even with a small amount of crack growth, the unloading curves did not return to the origin but instead at some positive offset (see Figure 23).

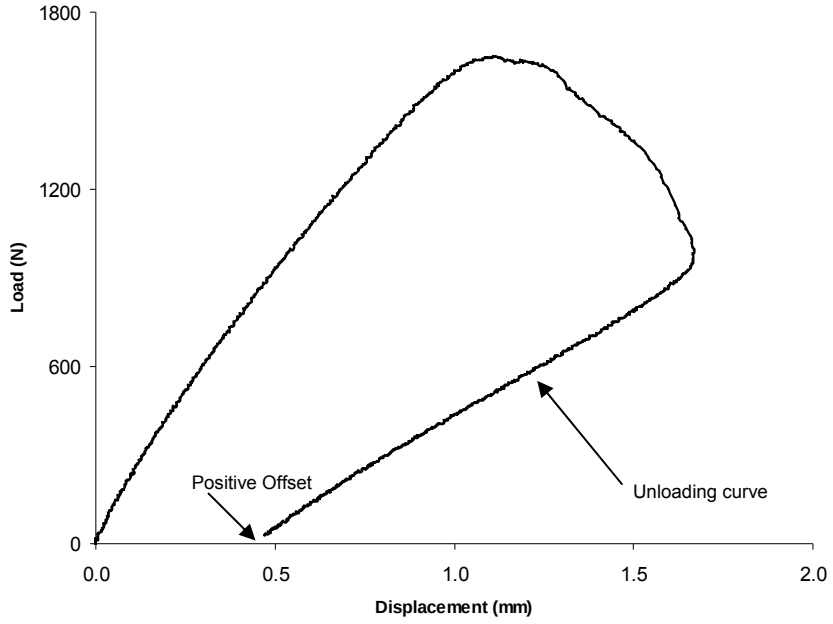

Figure 23. A typical loading and unloading curve for (TL and LT) specimens (here for 46 lb/ft^3 & 0.75" thickness). The unloading curves returned at a significant positive offset.

Using the test purposed by Atkins et al. (1988) additional specimens were loaded, allowed to crack and then unloaded after removing the fiber bridging zone. These tests produced unloading curves that returned nearly to the origin (see Figure 24). Similar curves were obtained with the modified unloading test (see Figure 25). Extrapolation of the partial unloading (with the intact fiber bridging zone) curve shows a significant displacement offset. When the specimen's bridging zone is

removed, once again the load drops significantly. More importantly, this test also shows the unloading curves return much closer to the origin, demonstrating that the fiber bridging between the two crack surfaces prevents complete closure during normal unloading.

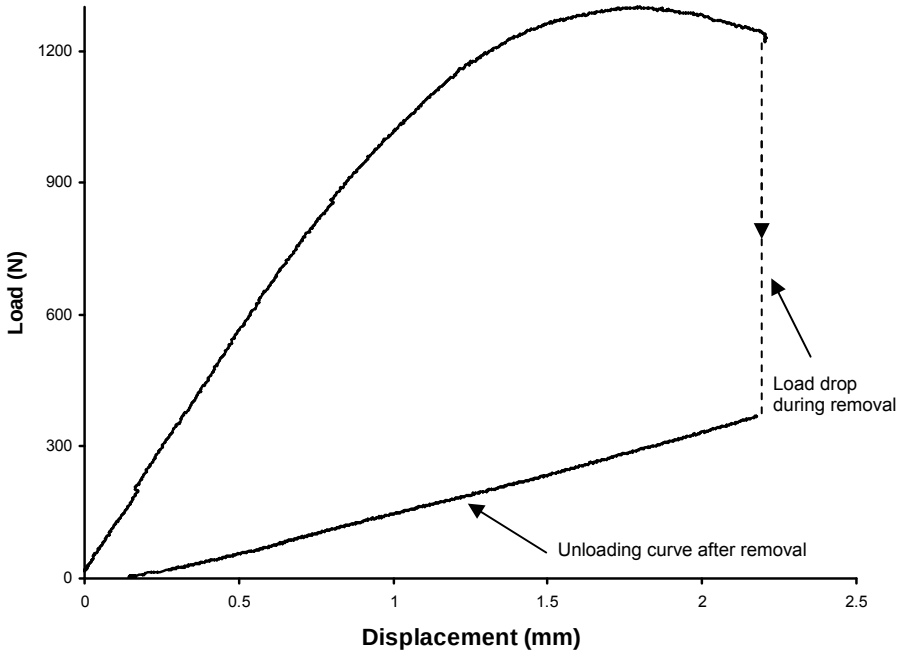

Figure 24. Unloading without bridging. A typical loading and unloading curve for (LT and TL) specimens with the fiber bridging zone removed (here specifically for a 46 LT specimen with thickness 0.5"). The dashed line represents the load drop during the removal of the zone.

The extra force required to smash these fibers and put the surfaces back together also lowers the apparent unloading compliance, making the specimen look stiffer. Without fiber bridging interference, the unloading curve of MDF specimens would return to origin which is consistent with the behavior of a linear-elastic material with negligible plasticity (Atkins et. al, 1988). This was the assumed behavior of the MDF specimens tested for the evaluation of fracture toughness.

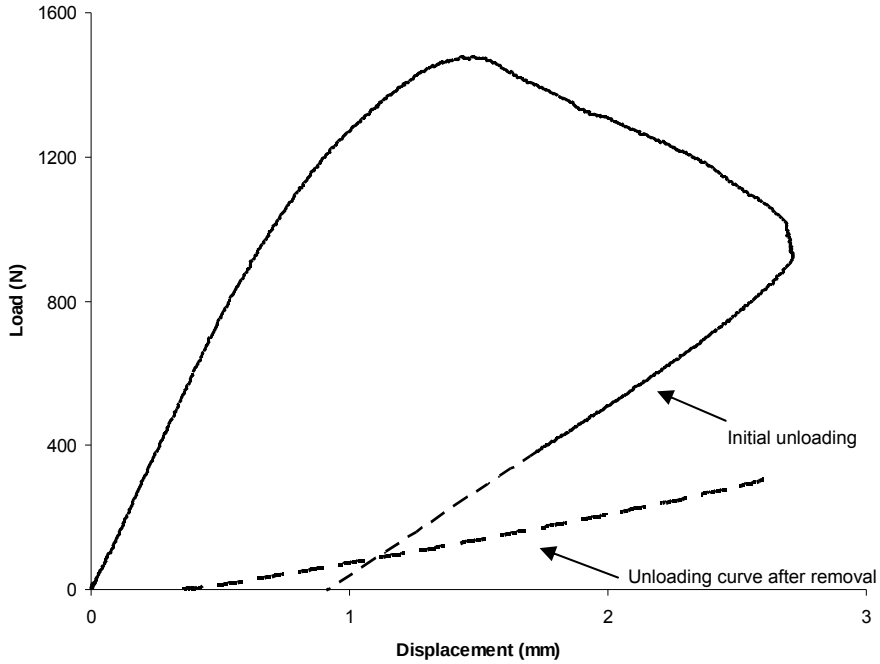

Figure 25. Modified unloading test. A curve produced by loading, partially unloading and extrapolating the curve back to find the offset (connected dashed line) for a 38LT specimen. The second dashed line is produced by first returning the specimen to the displacement before the initial unloading, removing the process zone and then unloading completely.

Fracture Energy from Load-Displacement Curves

Each load-displacement curve from a single specimen provided multiple energy envelopes from which the toughness could be calculated. At the beginning of a typical load-displacement curve was a slight adjustment phase where extensometer readings did not produce an exact linear slope because of settling in of the device (see Figure 26). Once the adjustment phase passed, the curves were linear and remained so until about 90 percent of the peak load. This region was non-linear because of micro-cracking (Ehart, 1999), the development of fiber bridging or crack blunting. After the peak, the load drops relatively slowly unlike in brittle fracture and is an indicator of the load carrying effects of fiber bridging.

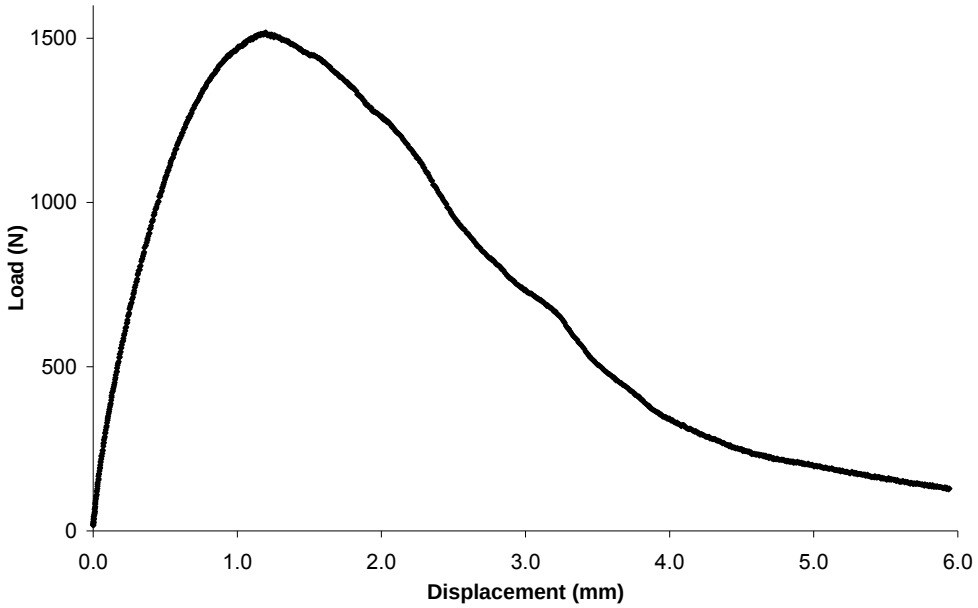

Figure 26. A typical load-displacement curve (46TL1 depicted). (See Appendix B Matsumoto (2008) for other specimens.)

From these load-displacement curves, the energy of fracture associated between any two points in loading P_i and P_j (with corresponding displacements δ_i and δ_j respectively) were easily calculated (eqn 12). To obtain the associated crack growths, Δa in order to calculate toughness, DIC was used.

Crack Growth from Digital Image Correlation

With the help of digital image correlation (DIC), having to make challenging direct measurements of crack length in the MDF specimens was avoided. By analyzing captured images (which corresponded to different points in the loading) with DIC, strain fields were calculated. Maps of the strain intensity (ε_{yy}, strain in the direction of loading) over a region of interest were produced (see Figure 27) for each image. During crack propagation the shape of the strain distribution remained relatively constant but displaced by the amount of the crack growth.

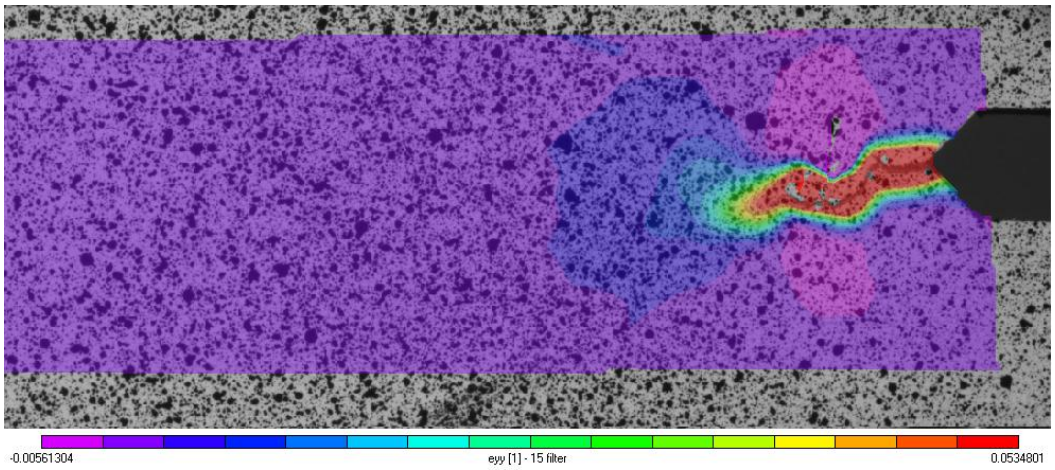

Figure 27. ε_{yy} strain contour for specimen with a crack.

Therefore, the displacement of this strain field between points in a test was a measure of growth, Δa. To measure the displacement of this characteristic distribution between loading points in the test, each of their strain "profiles", which is the value of strain (ε_{yy}) as a function of horizontal position along the crack line were plotted (see Figure 28).

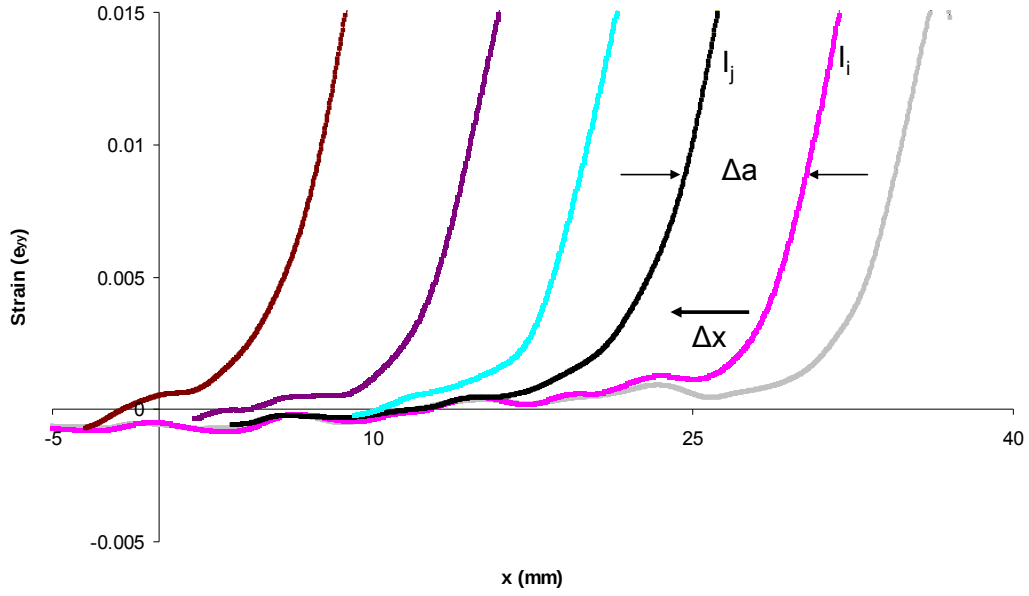

Figure 28. Experimental strain profiles produced by DIC from images corresponding to desired points in testing. The shift between any two profiles I_i and I_j, Δx is equivalent to crack growth Δa. For this specimen (46 ZTt1), the shifts were measured at a strain value of 0.006.

Each profile shows high values of strain near the crack tip (whose exact position is unknown). At points far away from the tip, the strain becomes small and eventually compressive. The shift in these profiles was assumed to be equivalent to the crack growth, Δa.

G_{IC} R-curve

From the fracture energies obtained from load-displacement data and the associated crack growths evaluated from DIC strain profiles, G_{IC} toughness vs. crack length (*a/w*) plots, or "R-curves" were produced (see Appendix B for all plots). A typical R-curve for a strong direction specimen (LT and TL*) is pictured in Figure 29 and a typical weak direction (ZT and ZL) is pictured in Figure 30.

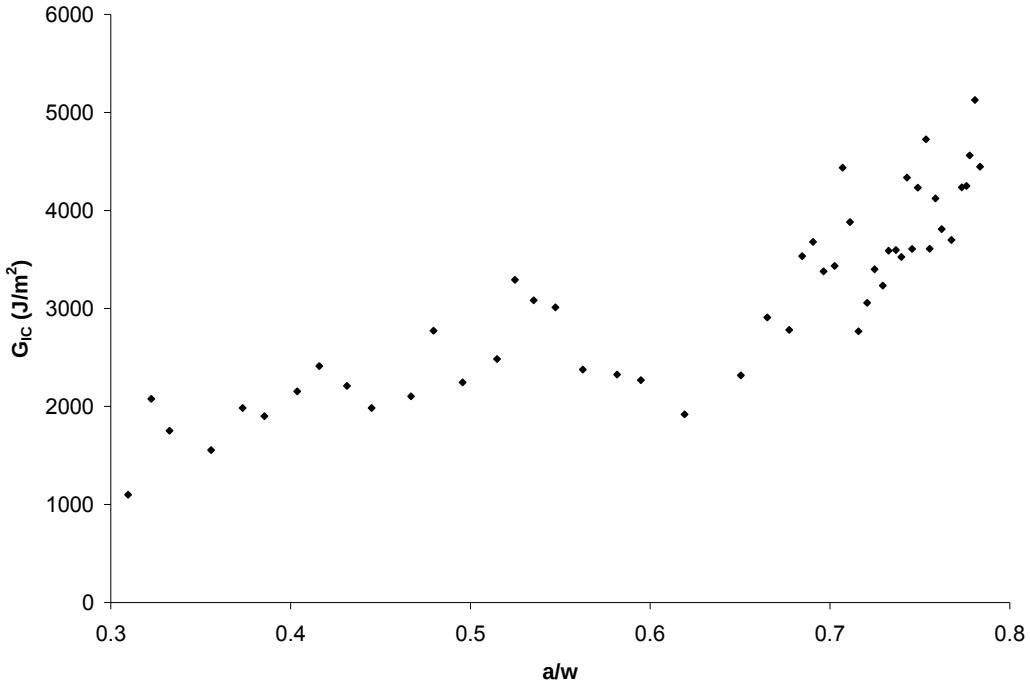

Figure 29. Typical G_{IC} vs. *a/w* plot for the strong directions (TL and LT specimens) here specifically for specimen 38 LTt1. *a/w* represents normalized crack length, where *a* is the crack length and *w*, the crack-line width which is 4.25 in (108 mm) (see Figure 13). An *a/w* of 0.28 represents the normalized length of the initial crack notch, and *a/w* = 1.0 would be a crack at the end of the specimen.

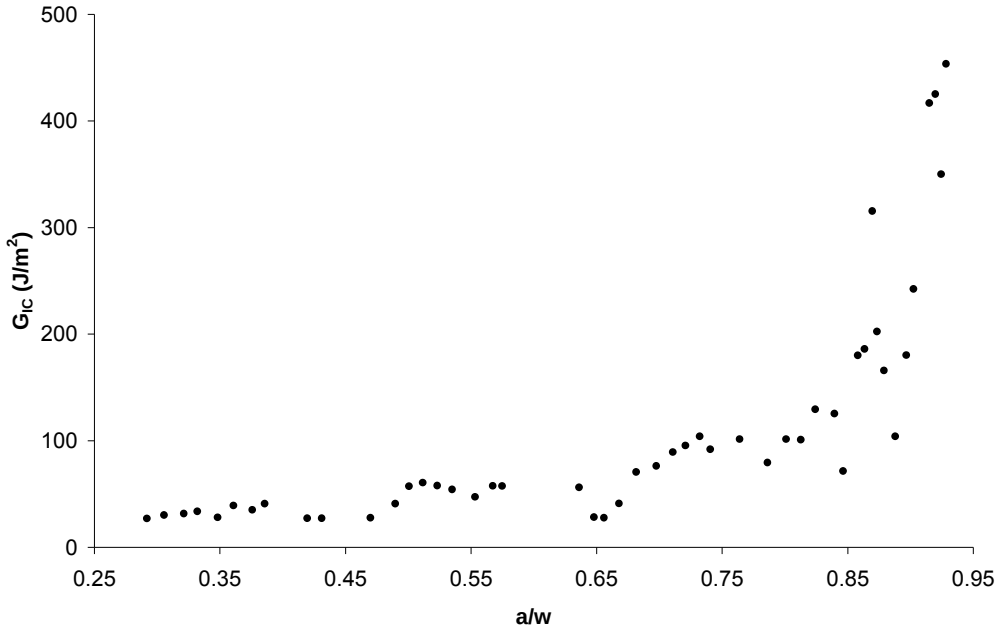

Figure 30. Typical G_{IC} vs. *a/w* plot for the weak directions (ZL and ZT specimens), specifically for 46 ZTt1.

To produce an R-curve for a single specimen required load-displacement data and coupled DIC analyzed images. Loading and simultaneous image capturing takes about 10-15 minutes. Although relatively few specimens were tested with full data, each specimen provided many experimental measurements of G_{IC}. Many specimens could not be analyzed with DIC, which included any TL specimens of 38 lb/ft^3 because in those specimens the crack turned significantly. However, the similarity between the load-displacement curves suggests that toughness properties are reproducible and much less scattered than strength tests (see Appendix B). Unlike strength tests, failure (crack propagation) occurs from a controlled flaw (i.e. the machined crack) rather than from some statistical flaw distribution.

Characterization of R-curves

For both the strong and weak crack propagation directions, from *a/w* = 0.28 till *a/w* = 0.7, G_{IC} increased in a linear fashion. A linear rise in toughness can be

attributed to fiber bridging that increases with crack extension. If these fibers absorb energy, they can be thought of as a separate material which contributes to the total toughness relative to the amount present. They do not actually increase the tip toughness of the material, but can shield the tip from driving energy for crack growth thus increasing the measured energy release rate. As the amount of fiber bridging increases, so does the total toughness. The contribution of fiber bridging to the total toughness seems to be on the order the order of 50% of the total toughness. This behavior can be reproduced in MPM models which will be presented later.

At $a/w = 0.7$, the measured toughness increased rapidly in all the specimens. A rapid increase may not correspond to the actual behavior of the material, but rather artifacts of experimental procedure. Near the edge of the specimen, the assumption of a constant strain distribution between points in the test may no longer be valid. As the crack approaches the edge, the strain field may change such that the perceived displacement is smaller, decreasing Δa and increasing the apparent toughness. Also, at large values a/w near the end of the specimen, the increment of crack growth is small. Since the calculation of G_{IC} necessitates division by a small Δa, errors may be introduced.

Often an increase in apparent toughness near the edge of a specimen is due to the loss of plastic constraint, where plastic zone interacts with the boundary. The loss of plastic constraint leads to an increase apparent toughness (Anderson, 2003). For this reason, many standards such as ASTM E399 restrict the proximity of the crack tip to the specimen edge (ASTM, 2006).

For the rapid rise in the apparent toughness near the edge of the specimens to be an actual material property suggests that the increase in toughness due to fiber bridging is at least 2-3 times higher than the inherent toughness of MDF. However, this seems unlikely because the rapid rise occurs in all specimens regardless of density, thickness or crack propagation direction (where fiber bridging effects might differ).

Cumulative R-curves

The cumulative R-curve procedure smoothes out some of experimental noise of the incremental energy method (Figure 31)

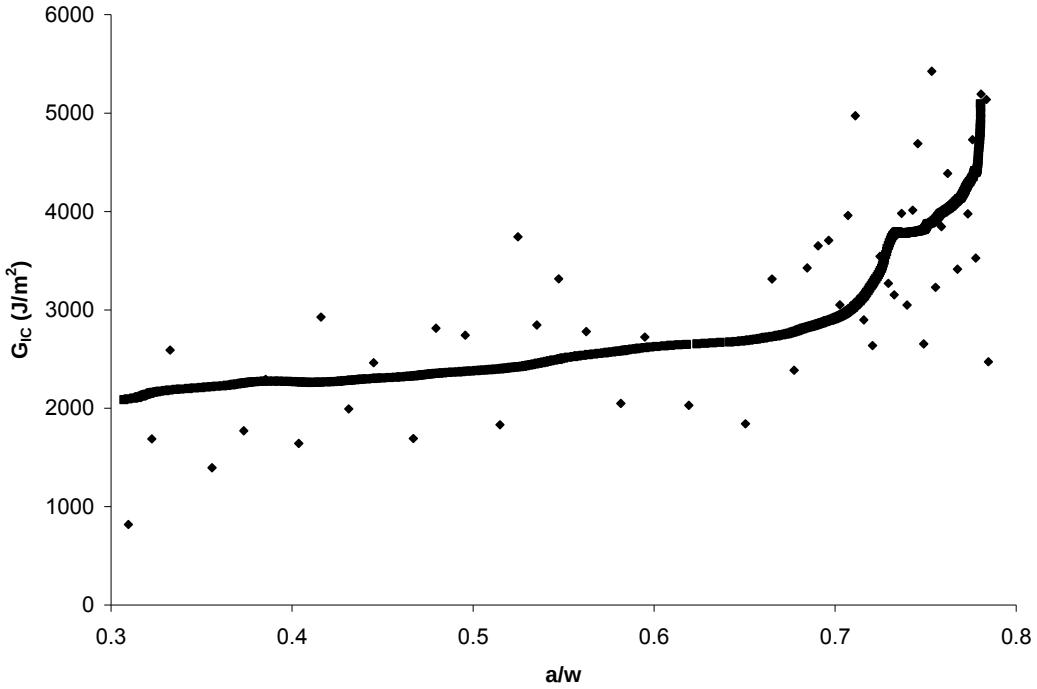

Figure 31. G_{IC} vs. *a/w* using the cumulative energy method (solid line) in comparison to traditional method (underlying data points) for 38LTt specimen.

Material Point Method (MPM) Models with Fiber Bridging

Bilinear traction laws using a $J_{tip,c}$ of 2000 J/m^2, J_B's in the range of 1100-1500 J/m^2, δ_c's in range of 2-2.5 mm and small values of δ (~0.0110-0.0126 mm) corresponding to σ_{max} ~1.1-1.25 MPa fit well to the experimental cumulative energy R-curve for specimen 38 LTt1 up to *a/w* = 0.7 (see Figure 32). Tractions with small values of δ, correspond to tractions with almost entirely linear softening. The initial linear region (Figure 21) has almost no influence on the behavior of the curve and the results are governed almost entirely by the secondary linear slope where the tractions contribute to total toughness.

Physically, the tip toughness, $J_{tip,c}$ is an initiation toughness, which is the inherent toughness of the material without any contribution from fiber bridging. At

values of *a/w* close to the initial notch (*a/w* = 0.28) the bridging is small, and the total toughness is essentially equal to $J_{tip,c}$.

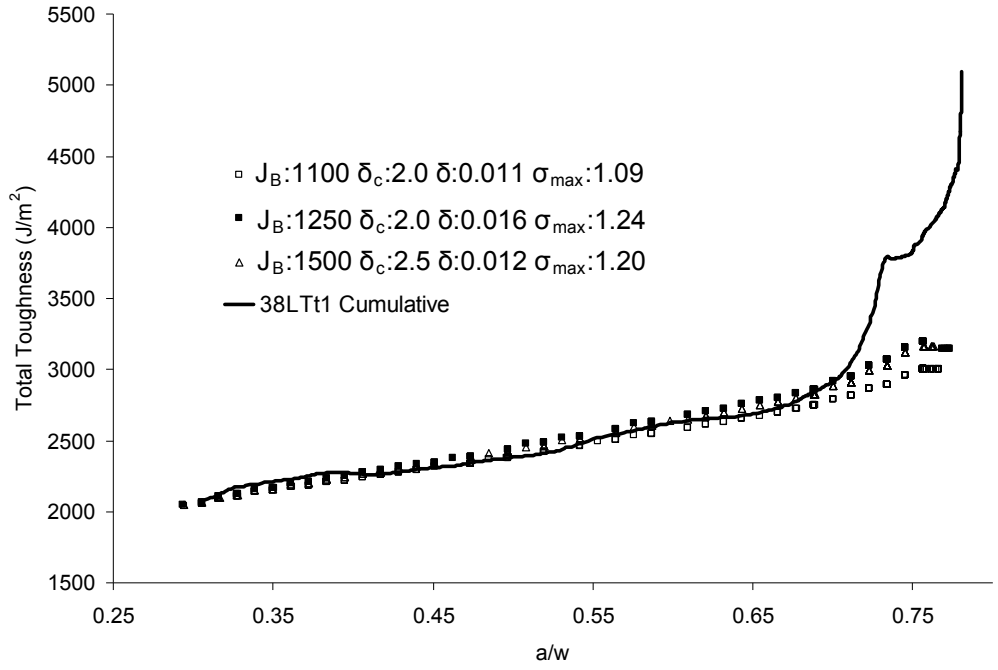

Figure 32. Bilinear traction law models using different combinations of bridging toughness (J_B) (J/m^2), critical opening displacements (δ_c) (mm), δ (mm) and associated σ_{max} (MPa) with tip toughness of 2000 J/m^2.

Cubic traction models using a $J_{tip,c}$ of about 2000 J/m^2, J_B in range of 1500-2200 J/m^2 and δ_c in the range of 2-2.5 mm fit well to the experimental R-curve for specimen 38LTt1 (see Figure 33). In comparison to the bilinear model, the cubic tractions did not fit as well to the experimental R-curve in the linear region (*a/w* = 0.28-0.7), but more closely reproduced the steep rise at values of *a/w* greater than 0.7. Both the bilinear and cubic models are in reasonable agreement with the tip toughness and critical displacement, δ_c but however differ slightly in the bridging toughness, J_B. The cubic tractions have a lesser contribution to toughness early on, but have a higher contribution near the end.

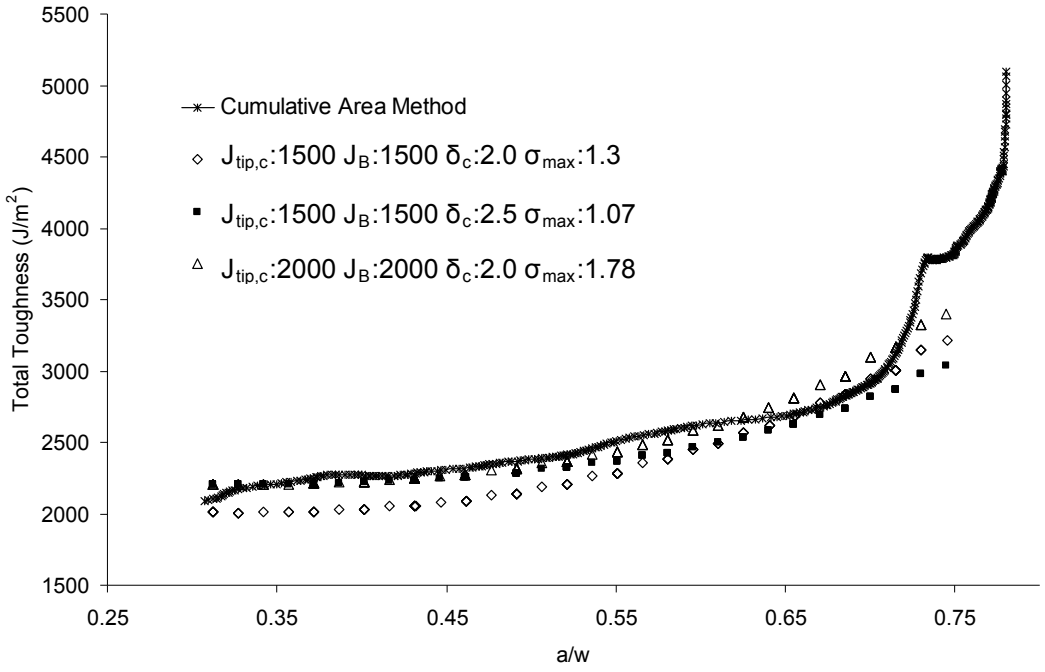

Figure 33. Cubic traction law models using different combinations of tip toughness ($J_{tip,c}$) (J/m^2), bridging toughness (J_B) (J/m^2), critical opening displacements (δ) (mm) and maximum stress (σ_{max}) (MPa).

These MPM numerical models suggest that the specimen 38LTt1 has an inherent toughness of about 2000 J/m^2. After fiber bridging develops, at steady-state (where tractions and the crack tip are propagating simultaneously, which is never actually reached in this specimen) contributes to the total toughness on the order of 1100-2200 J/m^2. Their maximum stress (σ_{max}) is on the order of ~1.07-1.78 MPa, and they completely fail when their displacement reaches the order of 2-2.5mm.

MDF Panel Toughness

To calculate a toughness for each panel and crack propagation combination, the data from each R-curve between *a/w* = ~0.4-0.7 were averaged for the different specimens (see Table 1), eliminating the region where the toughness rapidly increases and thus excluding potentially unreliable data due to the effects of edge.

Table 1. Average toughness (**J/m^2**) and *coefficient of variation* (%).

		Propagation Direction			
		LT	TL	ZT	ZL
Density (kg/m^3)	thickness (mm)	strong		weak	
609	12.7	*3070	x	**70.8**	**57.8**
		22.18	*x*	*50.31*	*35.24*
	19.05 (t)	**2930**	x	**43.6**	**85.6**
		19.50	*x*	*28.33*	*40.24*
737	12.7	**6070**	**5980	**85.6**	**87.8**
		23.85	*17.70*	*48.15*	*23.23*
	19.05 (t)	**5260**	**4920**	**70.8**	**58.0**
		22.73	*17.8*	*24.46*	*28.85*

*The average for three different specimens. ** The average of two different specimens.

The toughness in TL and LT crack propagation directions (the strong directions) for the 46 lbs/ft^3 (737 kg/m^3) density were nominally the same. The average toughness in the ZT and ZL crack propagation directions (the weak directions) were also very similar. However, strong directions were on the order of 75 times tougher than the weak directions. Only a slight variation was detected between the two thicknesses.

The toughness for the 36 lb/ft^3 (609 kg/m^3) density panels in its strong direction (LT; toughness for the TL direction could not be obtained for reasons previously mentioned) was lower than that of the higher density for both thicknesses, but compared to its weak direction, it too was significantly tougher, having a toughness roughly 50 times higher.

Interpreting the Toughness Variation

The readily apparent decrease in toughness from the higher to the lower density MDF panels is likely attributed to a lower density of wood fibers per volume and or the lower resin content. Without knowing the exact recipe to which the panels are made it is difficult do more than speculate.

Of significant interest is the drastic drop in toughness from the strong to the weak crack propagation directions in both densities of panels. This suggests that either the toughness in the MDF panels comes from the surface material sometimes called the “skins” or from the orientation of the wood fibers. The skins are noticeably

harder and denser, which is a result of the manufacturing process (see section 1. Literature Review). If the skins were removed and the remaining panel tested, the toughness would be much lower if they are source of the majority of the toughness. If the toughness is not lower, the orientation of the fibers in the panels is the likely cause of the toughness difference. In the MDF panels, the wood fibers are aligned mostly within the panel plane (see Figure 14). In TL and LT specimens, a crack must propagate through the fibers, while in the ZL and ZT directions it does not.

ASTM comparison

Calibration Functions from FEA

To verify the FEA approach to determining calibration functions, it was first applied to the ASTM CT specimen geometry. The result was then compared to the widely accepted functions in the literature (see Figure 34).

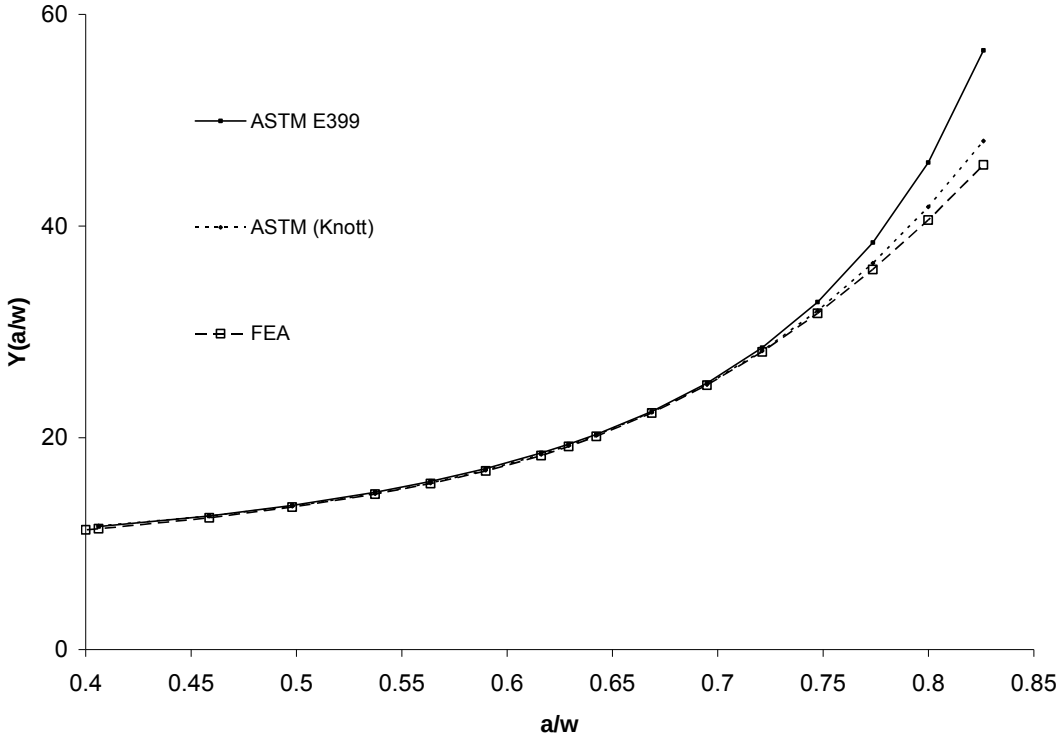

Figure 34. Comparison of calibration functions for the ASTM specimen. The solid line is from ASTM E399 (2006), the dotted line from Knott (1973) and the dashed line with squares the results from the FEA method used.

The FEA result is consistent with both the ASTM E399 (2006) and Knott (1973). The different *Y(a/w)* curves all diverge from each other at values of *a/w* greater than 0.75, where even the ASTM function is not considered valid. The FEA approach used is corroborated, lending credence to *Y(a/w)* obtained for the extended CT FEA. A calibration function of

$$Y(a/w) = 7.55 - 33.67\frac{a}{w} - 49.23\left(\frac{a}{w}\right)^2 - 38.67\left(\frac{a}{w}\right)^3 + 137.35\left(\frac{a}{w}\right)^4$$

was found for the extended CT specimen using finite element analysis (FEA). Using the ASTM E399 method and this calibration function obtained for the extended CT specimen through FEA, K_{IC} values were calculated for the various specimens and converted to G_{IC} values (see table 3) using their measured effective modulus (table 2), *E'* (eqn 19).

Table 2. Measured effective moduli, *E'* (MPa) for different specimens

Density (kg/m^3)	Direction	Thickness (mm) 12.7	19.05
609	LT	*1150,1020,1200	1330
	TL	1760	1290
737	LT	1910	2080
	TL	**3940,3610,3020	3020

*(38LT1, 38LT2, 38LT3), **(46LT, 46TL1, 46TL2)

In every case, the G_{IC} values were on the order of half of those measured from the energy method. At crack initiation, from which the peak load value is obtained for the K_{IC} methods, the specimen does not yet have the benefit of fiber bridging.

Table 3. G_{IC} toughness (J/m^2) converted from K_{IC} values.

Density (kg/m^3)	Direction	Thickness (mm) 12.7	19.05
609	LT	*1370*	*1260*
	TL	*1050*	*2060*
737	LT	*1740*	*2370*
	TL	*1970*	*1540*

(K_{IC} values were not calculated for the weak crack propagation direction specimens because the calibration function does not account for inhomogeneous stiffness.)

Applying this method to loads and the corresponding crack lengths after crack initiation shows the calculated toughness to be lower over the entire range of crack lengths (Figure 35).

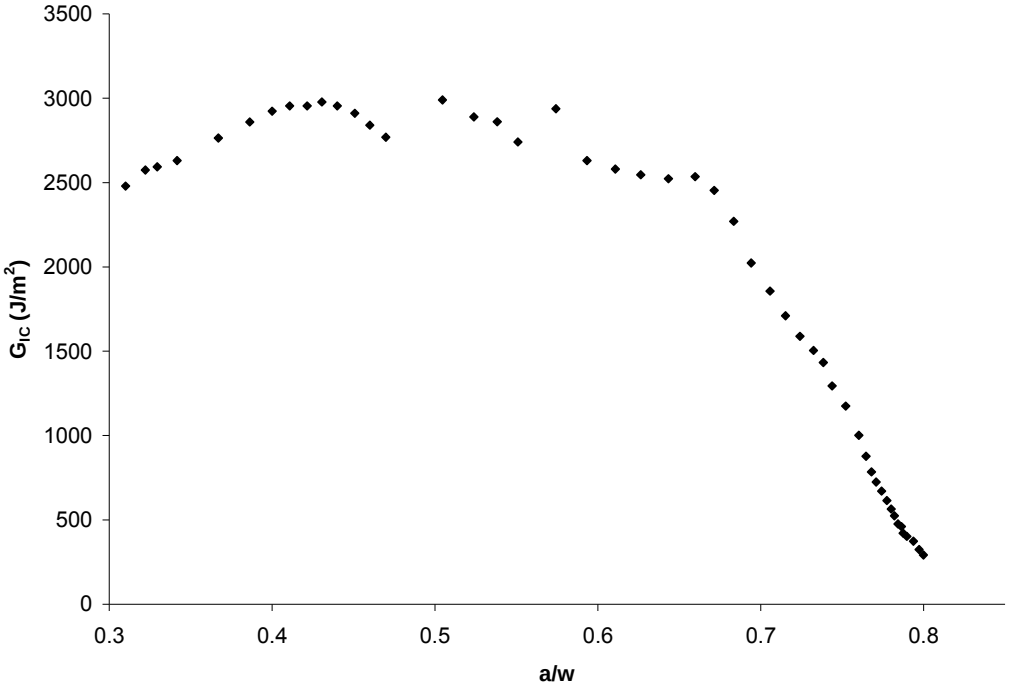

Figure 35. Calculated G_{IC} (ASTM) vs. *a/w* (46TLt1).

Like the results of the energy method, the calculated toughness increases from the initial *a/w* (~0.28) in a linear fashion to *a/w*=0.45. However, the values of toughness

are lower. At values of *a/w* greater than 0.45 the toughness actually starts to decrease which is opposite of the behavior observed in the energy method. The increasing amount of fiber bridging with crack length should increase toughness, not decrease it. The error in the ASTM method lies in the assumed calibration function, *Y(a/w)*.

The conservative values produced by the ASTM method suggest that the calibration function, which assumes no fiber bridging, is lower than the actual calibration function for MDF (see eqn 22). This also implies the actual *dC/da* is larger which is counterintuitive since the load as a function of displacement drops more slowly in MDF than for a linear-elastic material where no fiber bridging is assumed (see Figure 36). However, even though the change in compliance in the MDF curve is lower in the displacement space, the opposite is true in crack length space.

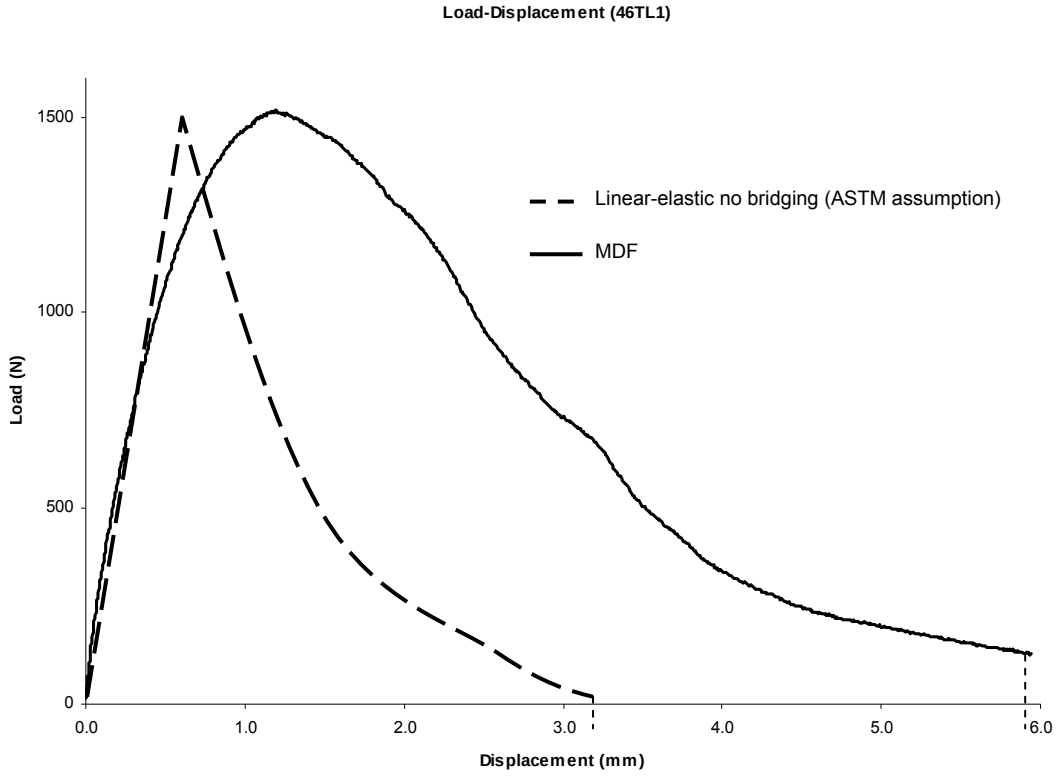

Figure 36. A comparison of an observed MDF load-displacement curve and symbolic linear-elastic curve assuming no fiber bridging (Ehart et. al, 1996). The curve of the linear-elastic specimen which assumes no bridging, decreases much more quickly in load-displacement space.

In reality, the actual *dC/da* and the one derived from *Y(a/w)* without fiber bridging are very similar at lower values of *a/w* (see Figure 37). At large values of *a/w* the experimental *dC/da* for MDF is actually higher (see Figure 37), at which point the ASTM E399 method is even more conservative. The change in compliance with respect to crack length (dC(a/w)/d(a/w)) was obtained by the method described in section 2. Materials and Methods.

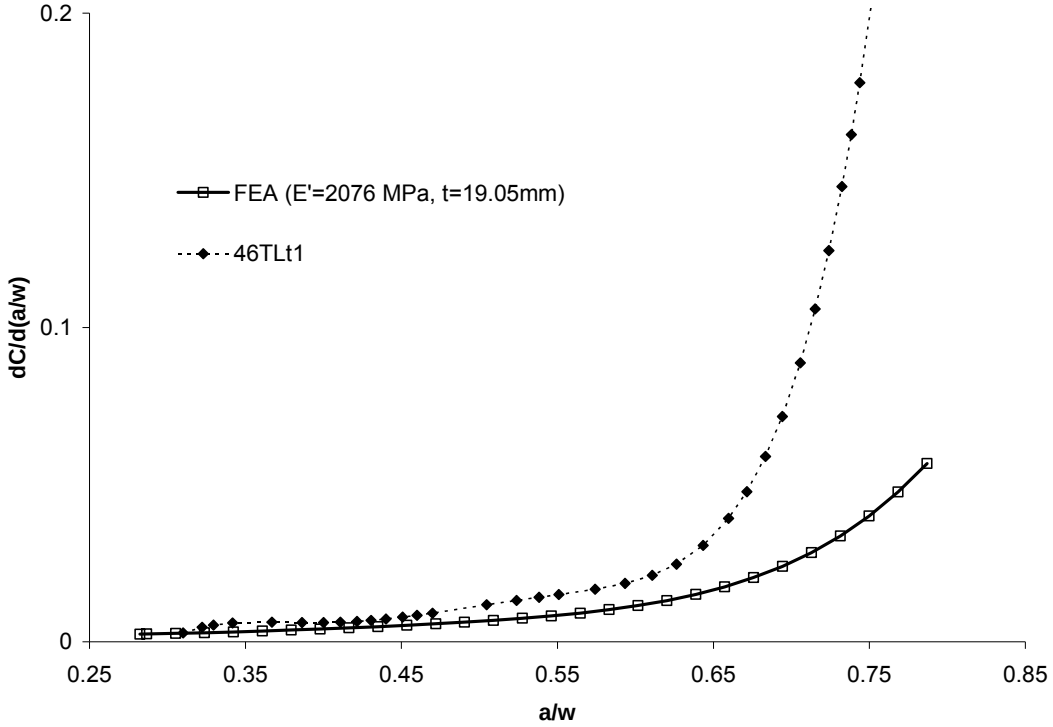

Figure 37. Comparison of experimentally measured *dC/d(a/w)* for specimen 46TLt1 with the *dc/d(a/w)* assuming no fiber bridging.

5. CONCLUSIONS

Medium density fiberboard represents one of the most challenging cases of evaluating fracture toughness. The fiber bridging that develops in its fracture process creates many experimental challenges. A new energy method was developed to overcome these challenges and used to evaluate the mode I fracture toughness of MDF with the following conclusions:

1. An energy method is required to measure the true toughness and R-curve behavior of MDF panels or other fiber bridging materials with analogous behaviors.
2. Measuring the crack length after crack propagation is a major challenge but can be solved using the displacement of strain-profiles along the crack line obtained through digital image correlation.
3. Unloading curves after crack propagation in MDF do not return to the origin and are not a measure of compliance because of fiber bridging interference. The correct fracture energy is one of a linear-elastic material with negligible plasticity, which was determined by unloading tests where the fiber bridging zone was removed.
4. Using the energy method proposed in this study, R-curves (G_{IC} vs. a/w) for MDF were developed showing its toughness to rise almost linearly from the initial crack notch to $a/w = 0.7$.
5. The R-curve behavior of a MDF specimen (38LTt1) was simulated with both bilinear and cubic traction laws in MPM. These numerical models suggest that the specimen has an inherent toughness ($J_{tip,c}$) in the range of 2000-2200 J/m^2, and bridging toughness in the range of 1100-2000 J/m^2. The bridging fibers have a σ_{max} on the order 1-2 MPa and completely fail at a displacement, δ_c between 2-2.5 mm.
6. The toughness of the higher density MDF panels (737 kg/m^3) was about twice that of the lower density panels (609 kg/m^3). Only a slight difference was

detected between the two thicknesses (12.7 and 19.05 mm) of the same densities. However, a significant difference was observed between the "strong directions" and the "weak directions" in both densities of panels. The toughness in the strong direction for the lower density panels was on the order of 50 times higher than that of its weak directions and for the higher density panel about 75 times. The large difference suggests that the toughness of MDF comes either from the outer "skins" or from fiber-alignment in the plane of the panels.

7. Finite element analysis can be used to determine compliance as a function of crack length for different fracture specimens. Compliance as a function of crack length can then be used to accurately calculate a calibration function for these specimens for use in the ASTM E399 method.
8. Applying the ASTM E399 on MDF which assumes a linear-elastic material with no fiber bridging for the initial crack notch gives conservative values of toughness in comparison to the energy method. At longer crack lengths with significant amounts of fiber bridging, it is even more conservative. This implies that the calibration function (and therefore *dC/da*) for MDF should be higher than the one assumed for a linear-elastic material with no fiber bridging.

Experimental Method Symbols

a - crack length
B - thickness specimen
Δ - extension to ASTM CT specimen
E - modulus elasticity
E' - effective modulus ($E/(1-\nu^2)$)
ε_{yy} - strain in direction of loading
Δx - displacement of crack profile
Δa - change in crack length (crack growth)
W - ASTM CT specimen scaling factor
w - extended CT scaling factor ($W + \Delta$)
a/w - normalized crack length
t - denotes specimen of 19.05 mm thickness
G_{IC} - strain energy release rate in mode I
K_{IC} - stress intensity factor in mode I
C - compliance
W_f - fracture energy
ν - poisson's ratio
P_{max} - maximum load from load-displacement curves
$P_{5\%}$ - load at intersection of 95% of slope
i (subscript) - denotes quantity at crack length i
j (subscript) - denotes quantity at crack length j
P_i - load at crack length i
P_j - load at crack length j later
C_i - compliance crack length i
C_j - compliance crack length j later
U_i - displacement at crack length i
U_j - displacement at crack length j later
$U(d)$ - cumulative energy with respect to displacement
R - G_{IC} as a function of crack length
C_o - $1/BE'w$
$U(a)$ - cumulative energy with respect to crack length
$\delta_{a/w}$ - displacement at a/w
$P_{a/w}$ – load at a/w
$Y(a/w)$ - calibration function
$C(a/w^*)_{Ex}$ - experimental compliance at a/w^*

Numerical Symbols (un-italic)

Finite Elements Analysis

U_s - strain energy calculated from FEA
P - applied load
δ - displacement at loading pin
$C(a/w^*)_{FEA}$ – compliance at crack length a/w* calculated by FEA for a given specimen geometry and effective modulus

Material Point Method

Δ - traction opening displacement
$J_{tip,c}$ - defined material tip toughness
J_B - defined bridging toughness
δ - displacement at peak stress in tractions laws
δ_c - displacement failure
σ - traction stress
σ_{max} - maximum traction stress

6. BIBLIOGRAPHY

Anderson, T.L. (2005). "Fracture Mechanics, Fundamentals and Applications." *CRC Press: Taylor and Frances Group*, Boca Raton, FL, 122-125, 310-311.

Annual book of ASTM Standards (2006), "Standard Test Method for Plane-Strain Fracture Toughness of Metallic Materials," *ASTM Designation: E399-05a.*

Annual book of ASTM Standards (2006), "Standard Test Method for Plane-Strain Fracture Toughness of Metallic Materials," *ASTM Designation: E1820-05a.*

Atkins, A.G., Mai, Y-W. (1988). "Elastic and Plastic Fracture Mechanics: metals polymers, composites, biological materials." *John Wiley and Sons*, Ellis Horwood Limited, Market Cross House, Cooper Street, Chichester, West Sussex, PO19 1EB, England, 108-113.

Bower, J.L., Shmulsky, R. and Haygreen, JG. (2003). "Forest Products and Wood Science-An Introduction." 4th Edition. Ames, IA: *Iowa State Press*.

Ehart, R.J., Stanzl-Tschegg, S.E., Tschegg, E.K. (1996). "Characterization of crack propagation in particleboard." *Wood Science and Technology* 30, 307-321.

Correlated Solutions Inc. *Vic 3D User Manual*. West Columbia, SC.

Ganev, S., Gendron G., Cloutier, A., Beauregard, R. (2005). "Mechanical Properties of MDF as Function of Density and Moisture Content." *Wood and Fiber Science*, Vol. 37, 2, 314-226.

Griffith, A.A. (1920). "The Phenomena of Rupture and Flow of Solids." *Philosophical transactions*, Series A, Vol. 221, pp. 163-198.

Gross, B., Srawley, J.E., Brown, W.F. (1964). "Stress Intensity Factors for a Single-Edge-Notched Tension Specimen by Boundry Collocation of a Stress Function." NASA Lewis Research Center.

Hashemi, S., Kinloch A.J., William, J.G. (1990). "The analysis of interlaminar fracture in uniaxial fibre reinforced composites." *Proc R Soc Long*, A:347, 173-199.

Investment New Zealand. *Medium Density Fiberboard Subsector Profile*. (http://www.investmentnz.govt.nz/section/14282.aspx, 2005-2008)

Irwin, G.R. (1957). "Analysis of Stresses and Strains near the End of a Crack Traversing a Plate." *Journal of Applied Mechanics*, Vol. 24, pp.361-364.

Knott, J.F. (1973), "Fundamentals of Fracture Mechanics." *Butterworths & Co. Ltd*, London, England, 88 Kingsway,WC2b 6AB, 132.

Larson, H.J., Gustafsson, P.J. (1993). "Determination of Fracture Energy of Wood for Tension Perpendicular to the grain." *Draft NORDTEST Method*, Lund Institute of Technology, Lund Sweden.

Logan, D.L. (2000). "A First Course in the Finite Element Method." *Thomson Learning: Brooks/Cole*, Pacific Grove California,1.

Matsumoto, N., Nairn, J. (2007). "Fracture Toughness of MDF and other Materials with Fiber Bridging." *Proc. of 22nd Ann. Tech. Conf. of the American Society of Composites*, Sept 17-19, Seattle, WA.

Morel, S., Mourot, G. and Schmittbuhl, J.(2003) "Influence of the specimen geometry on R-curve behavior and roughening of fracture surfaces." *International Journal of Fracture* 121, 23-24.

Morris, V.L., Hunt, D.G, Adams, J.M. (1999). "The Effects of Experimental Parameters on the Fracture Energy of Wood-based Panels" *Journal of the Institute of Wood Science* 85, 32-38.

Nairn, J.A. (2003). "Material point method calculations with explicit cracks." *Computer Modeling Engineering & Sciences*, v4, 649-664.

Nairn, J.A (2008). "Analytical and Numerical Modeling True R Curves for Cracks with Process Zones Using J Integral Methods," (Pre-printing)

Niemz, P., Diener, M. and Pöhler, E. (1997). "Untersuchungen zur Ermittlung der Bruchzähigkeit an MDF-Platten," *Holz als Roh- und Werkstoff*, V 55 #5, 327-330.

Niemz, P., Diener, M. and Pöhler, E. (1999). "Vergleichende Untersuchungen xur Ermittlung der Bruchzahigkeit an Holzwerkstoffen," *Holz als Roh- und Werkstoff*, V 57, 222-224.

Razi, P.S., Raman, A. (2000). "Studies on impact fracture properties of wood-polymer compsites." *Journal of Composite* Matierals, v34, n 12, p980-997

Rice, J.R. (1968). "A Path Independent Integral and the Approximate Analysis of Strain Concentration by Notches and Crack." *Journal of Applied Mechanics*, Vol. 35, pg. 379-386.

Sadeq, S (2002). "Soil structure interaction in transparent synthetic soils using digital image correlation." PhD thesis, Polytechnic Univ., Brooklyn, NY.

Samarasinghe, S. Kulasiri, G.D. (2000). “Displacement fields of wood in tension based on image processing: Part 1.” *Silva Fennica*, 34(3), 251-259.

Smith, I., Landis, E., Gong, M. (2003). “Fracture and Fatigue in Wood.” *John Wiley & Sons Ltd*, West Sussex PO19 8SQ, England, 161-166.

Sutton, M.A., Wolters, W.J., Peters, W.H., Rawson, WF., and McNeil, S.R. (1983). “Determination of displacement using an improved digital image correlation method.” *Image and Vision Computing*, 1(3), 133-139.

Thuvander, F., Sjodahl, M., Berglund, L.A. (2000). “Measurement of crack tip strain field in wood at the scale of growth rings.” *Journal of Materials Science* 35, 6267-6275.

Wang, S.,Winistorfer, P.,Young, T.A., Helton, C. (2001). “Step-closing pressing of medium density fiberboard; Part 1. Influences on the vertical density profile.” *Holz als Roh- und Werkstoff* 59 (2001) 19-26.

7. APPENDICES

Appendix A: Materials and Methods Supplement

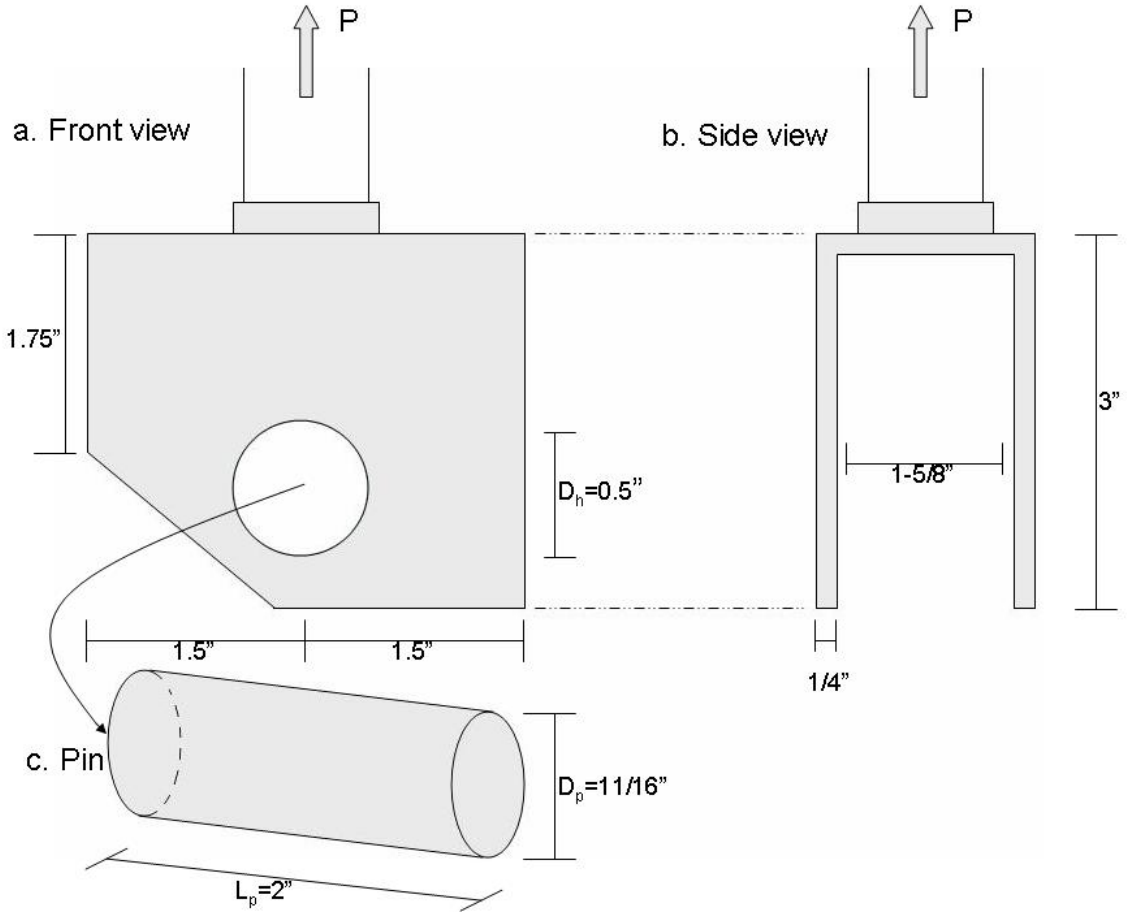

Figure A1. Loading fixtures. One of a set of two symmetric loading fixtures and loading pin (all fabricated out of steel).

DIC Calibration

After carefully focusing and adjusting the cameras, the specimen was removed from the loading position so that the image analysis software VIC-3D® could be calibrated. Calibration was performed by positioning a calibration target (see Figure 2A) at various positions in the viewing area and taking images using VIC-Snap®. The square calibration target was white with rows and columns of equally spaced black dots which served as reference points and dimensions for the correlation software.

Calibration targets approximately one-fourth of the camera's viewing area were found to be an ideal size.

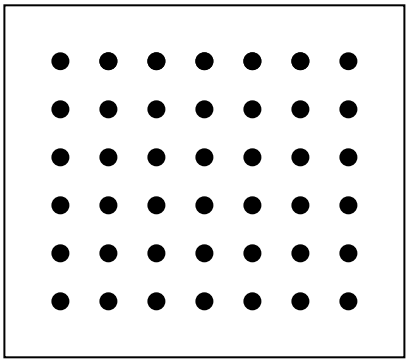

Figure A2. DIC sample calibration target.

A set of calibration images consisted of roughly 25 different images of the calibration target. The target was placed at every point in the viewing area at the intended specimen location (the focal plane) and in, in front of, behind and at different angles to the focal plane of the cameras. The dimensions of the dot spacing were input into VIC-3D® software and the images extracted for calibration analysis. Extraction was performed by an algorithm contained in the software that locates the dots in the image. By adjusting the threshold manually, some images that were not extracted by the auto-extract function could be extracted. An extracted set of images represents a solution set for VIC-3D® calibration. A report of the global and individual images' standard deviations (STD) from the calibration solution was given by the software. If an image had a standard deviation above 0.04, re-extraction was attempted. If re-extraction did not change the STD to the acceptable level, the image was not used as part of the solution set. Once a solution set's STD was satisfactory, the calibration was accepted to be used to calculate the stain field.

DIC Resolution

The resolution of the DIC setup depends on a number of different factors which include the robustness of the correlation software, the specimen speckle pattern, the pixel resolution of the digital cameras, the lighting, camera angle and distance to

the specimen and area of analysis. These factors change slightly for each specimen tested resulting in slight variation of resolution levels. The minimum detectable strain level (ε_{yy}) was assessed by taking the standard deviation of the strain values over the region of interest for several specimens and associated test setups and found to be in the range of 71-115 micro strain (10^{-6}).

Appendix B: Plots

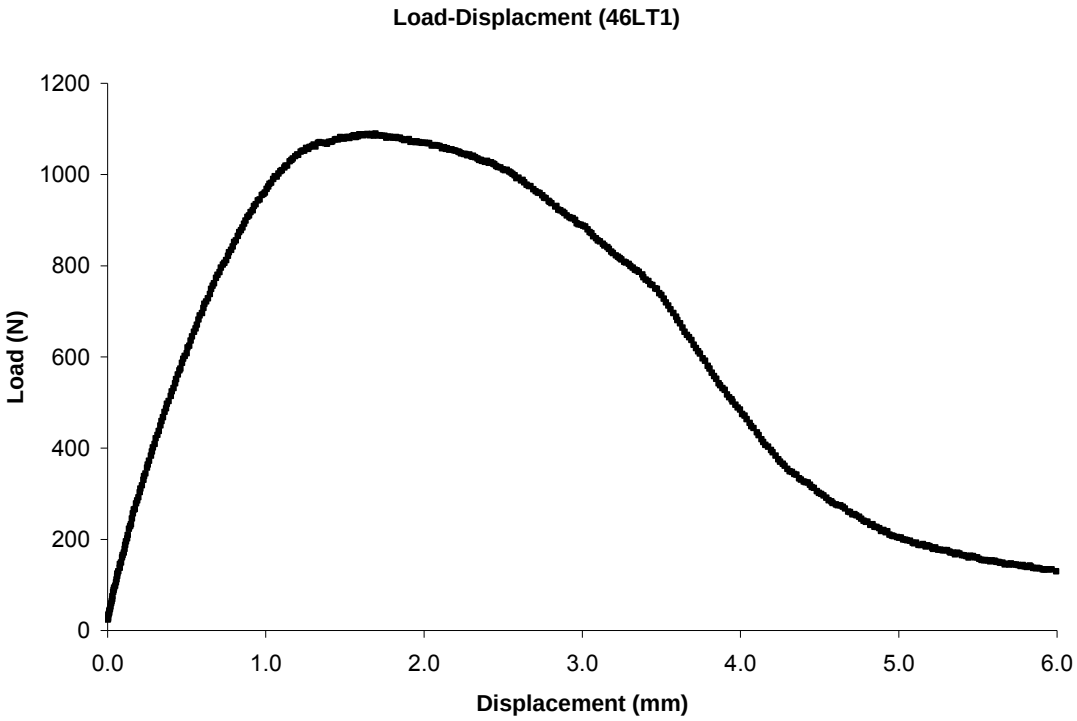

Figure B1. Load-displacement curve (46LT1)

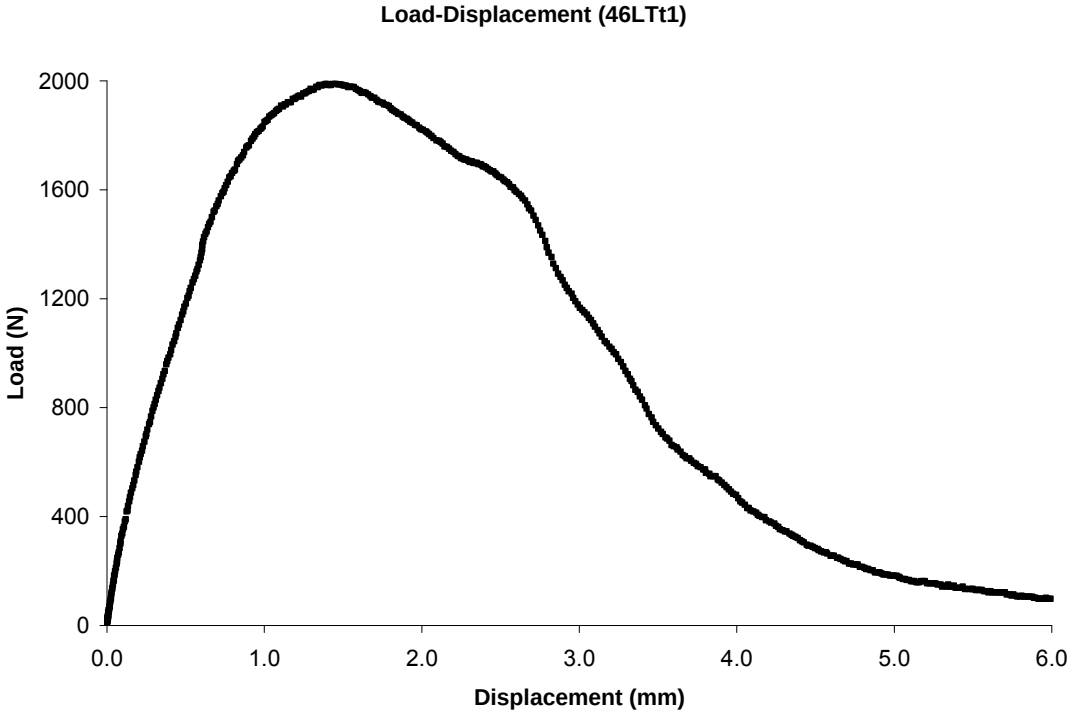

Figure B2. Load-displacement curve (46LTt1)

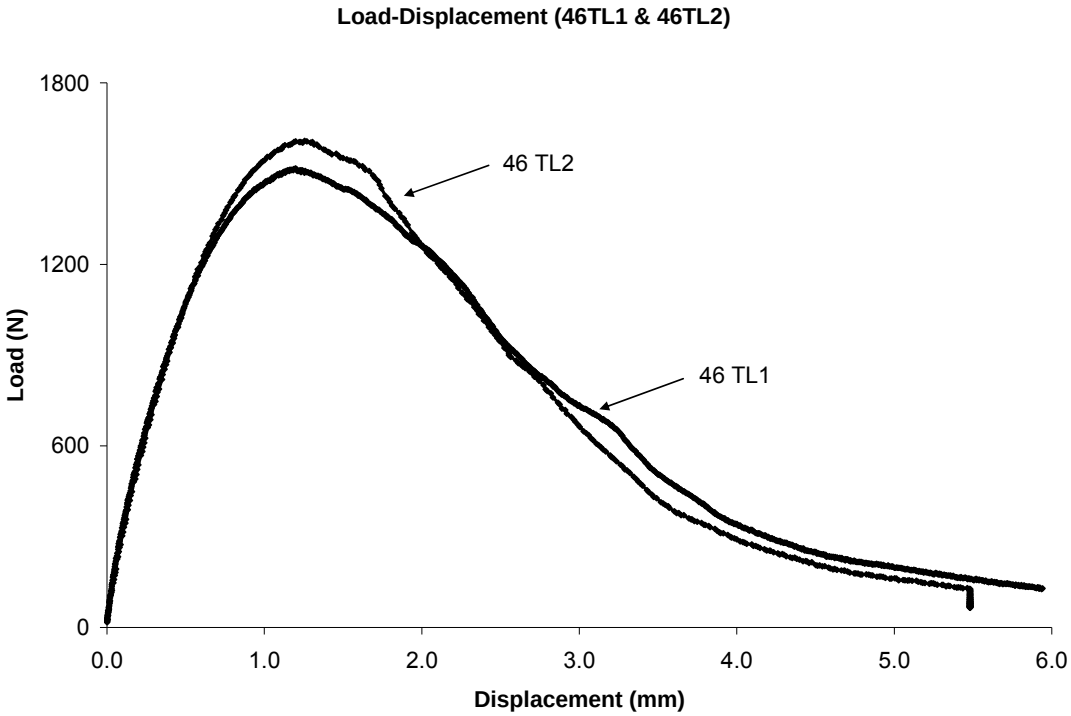

Figure B3. Load-displacement curve (46TL1 & 46TL2)

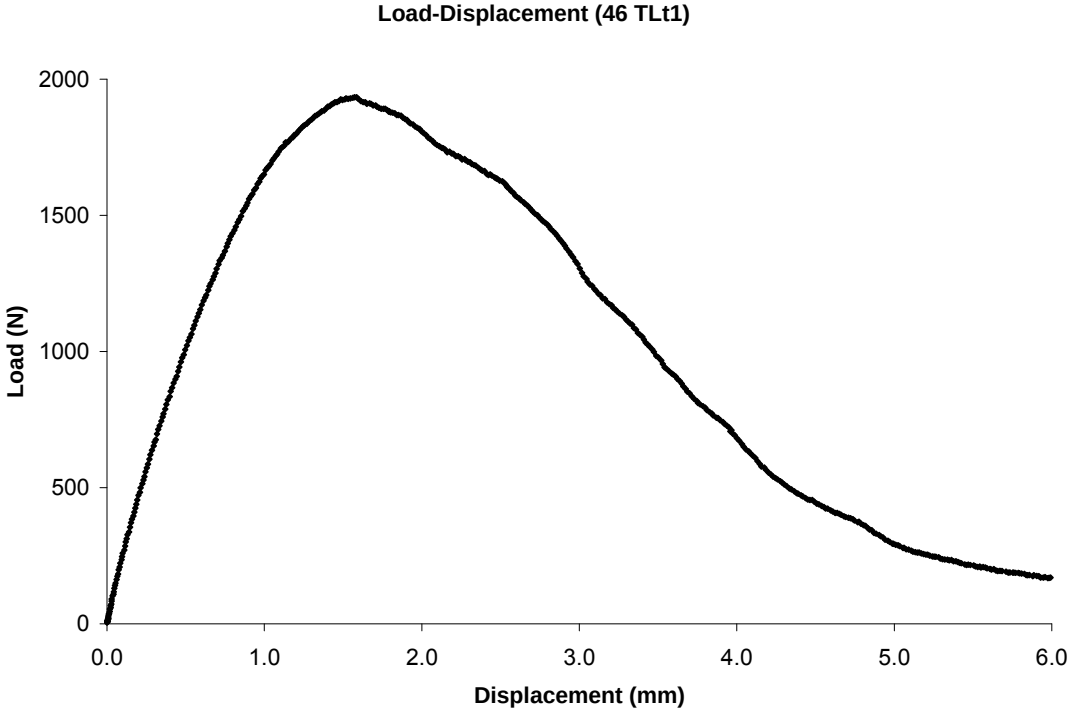

Figure B4. Load-displacement curve (46TLt1)

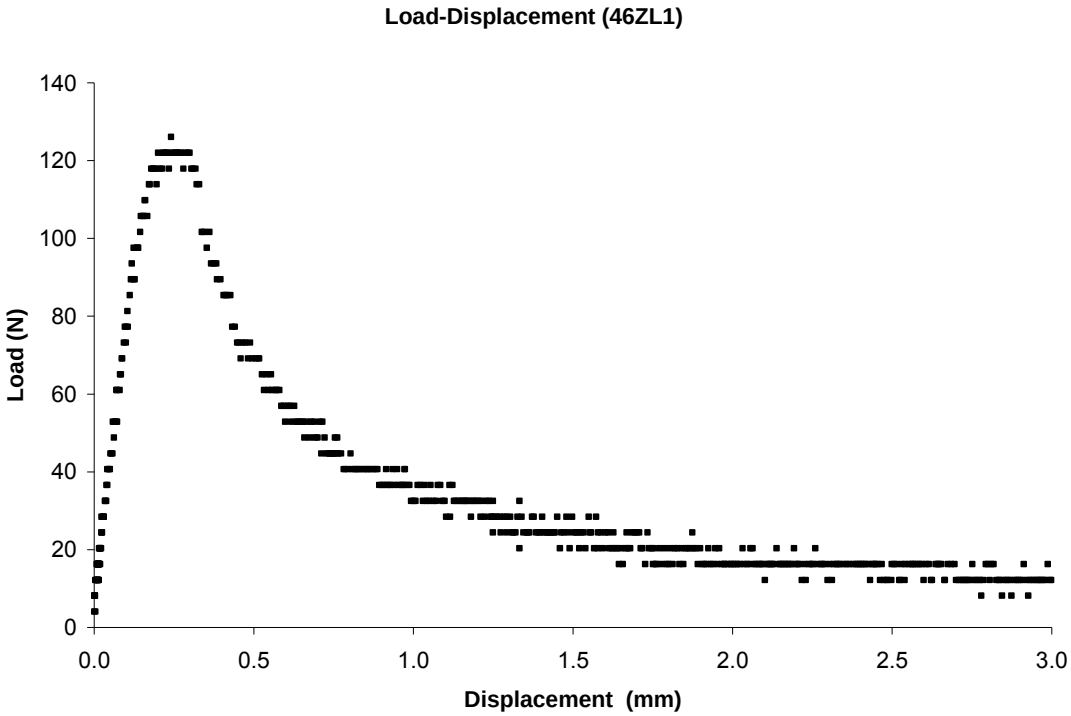

Figure B5. Load-displacement curve (46ZL1)

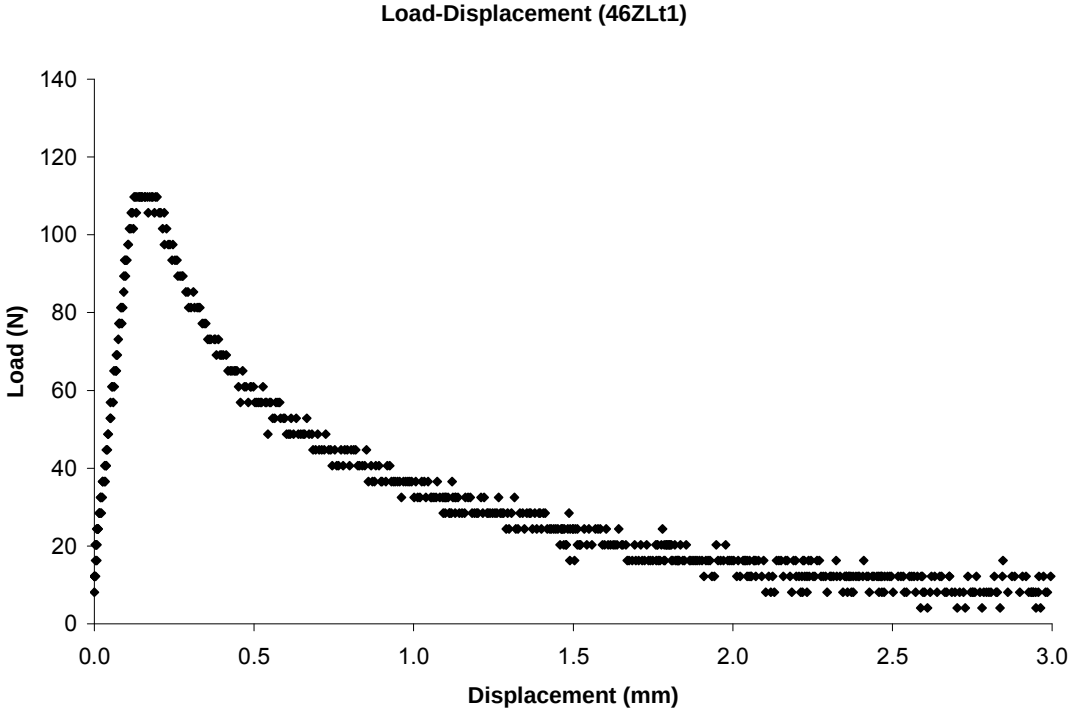

Figure B6. Load-displacement curve (46ZLt1)

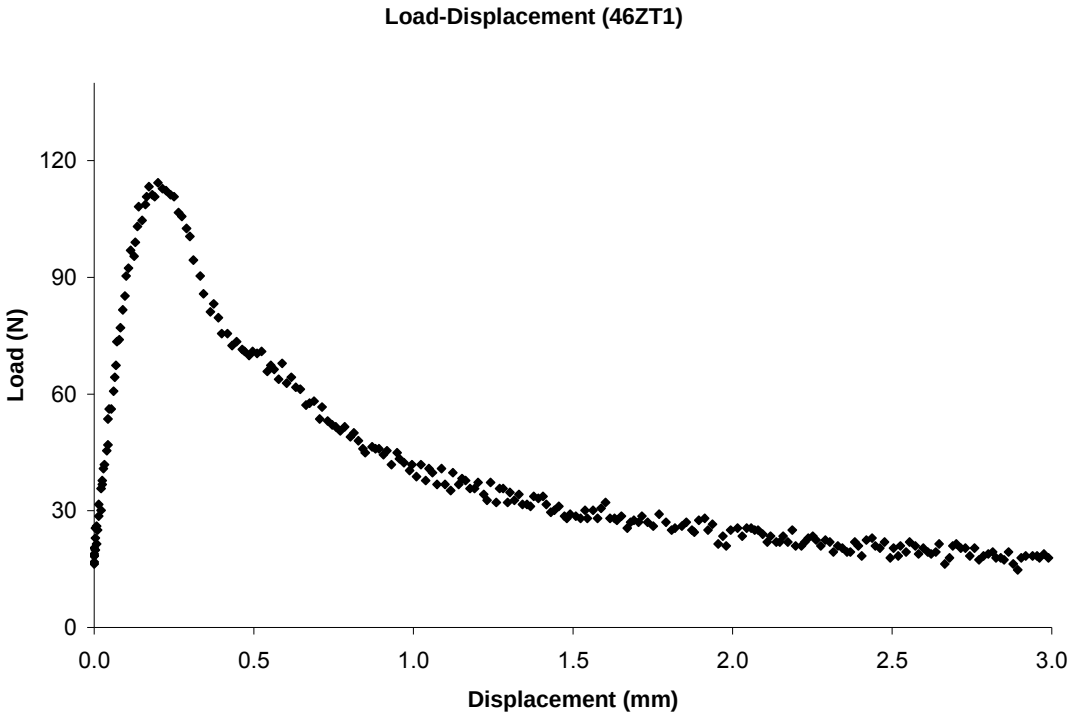

Figure B7. Load-displacement curve (46ZT1)

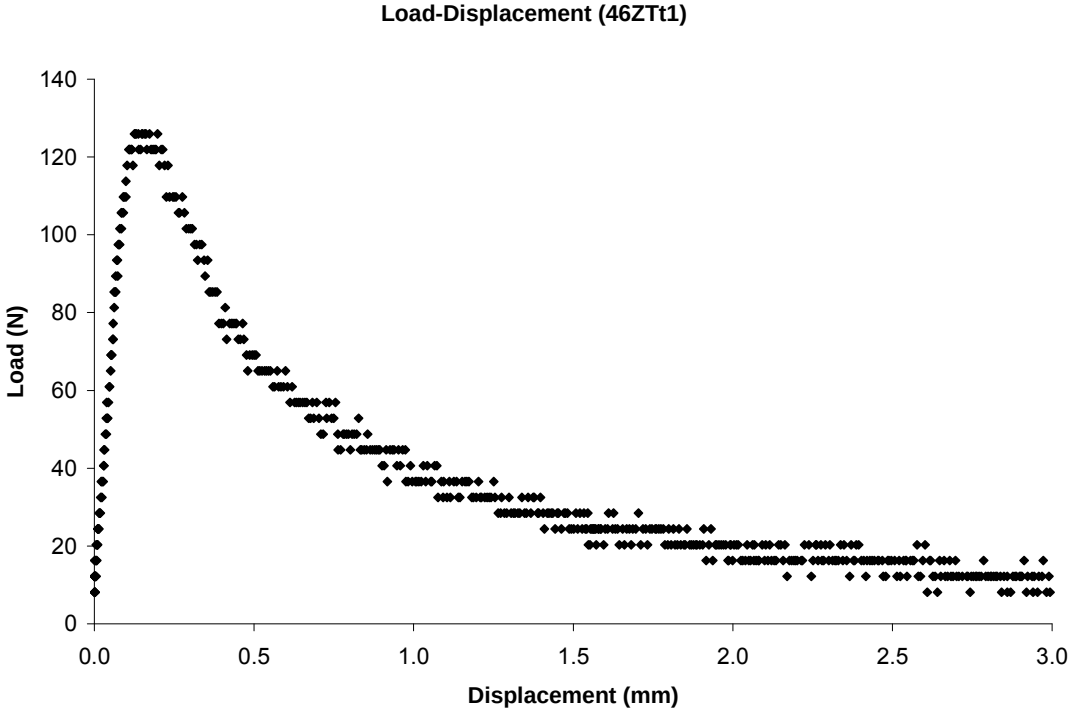

Figure B8. Load-displacement curve (46ZTt1)

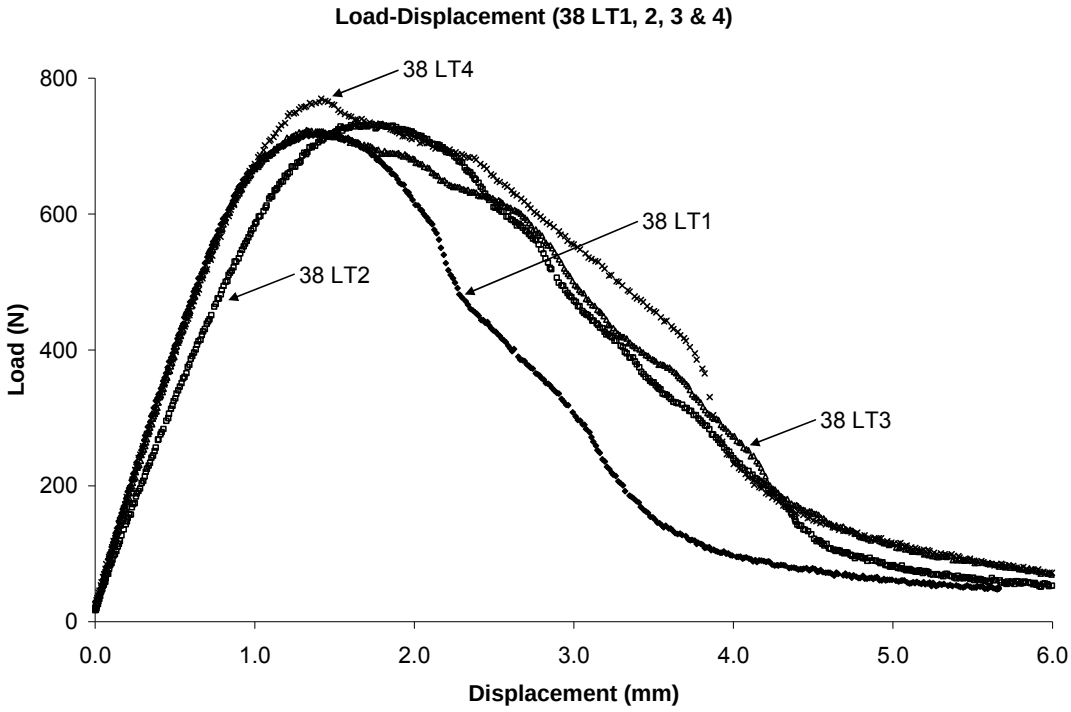

Figure B9. Load-displacement curve (38LT1, 2, 3 & 4)

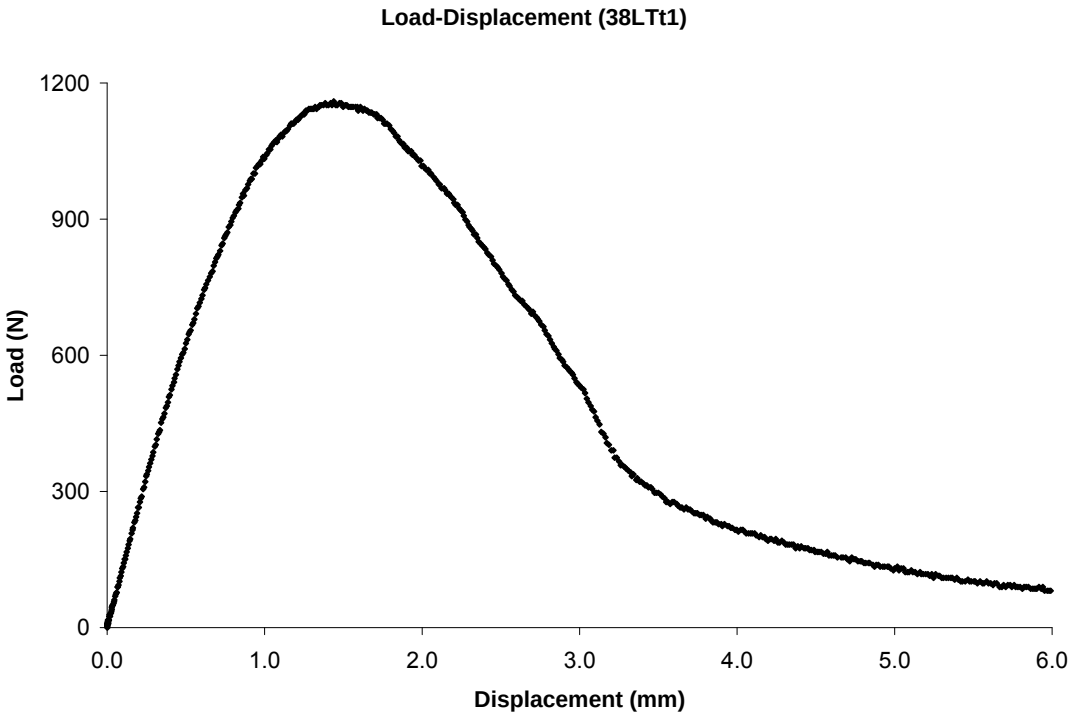

Figure B10. Load-displacement curve (38LTt1)

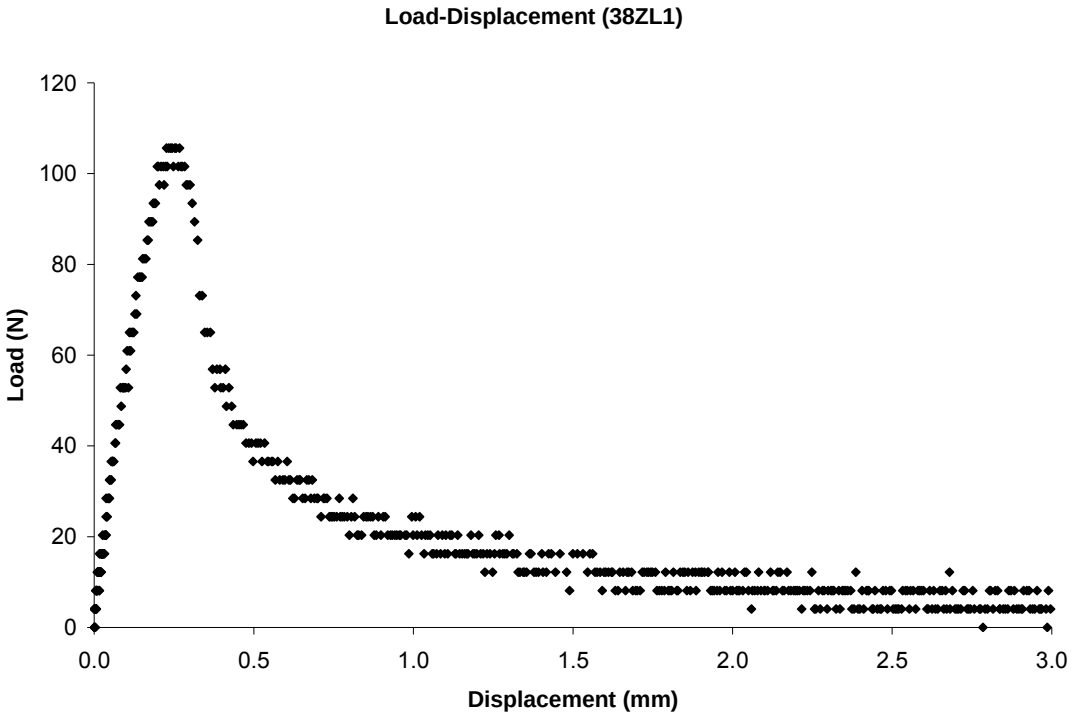

Figure B11. Load-displacement curve (38ZL1)

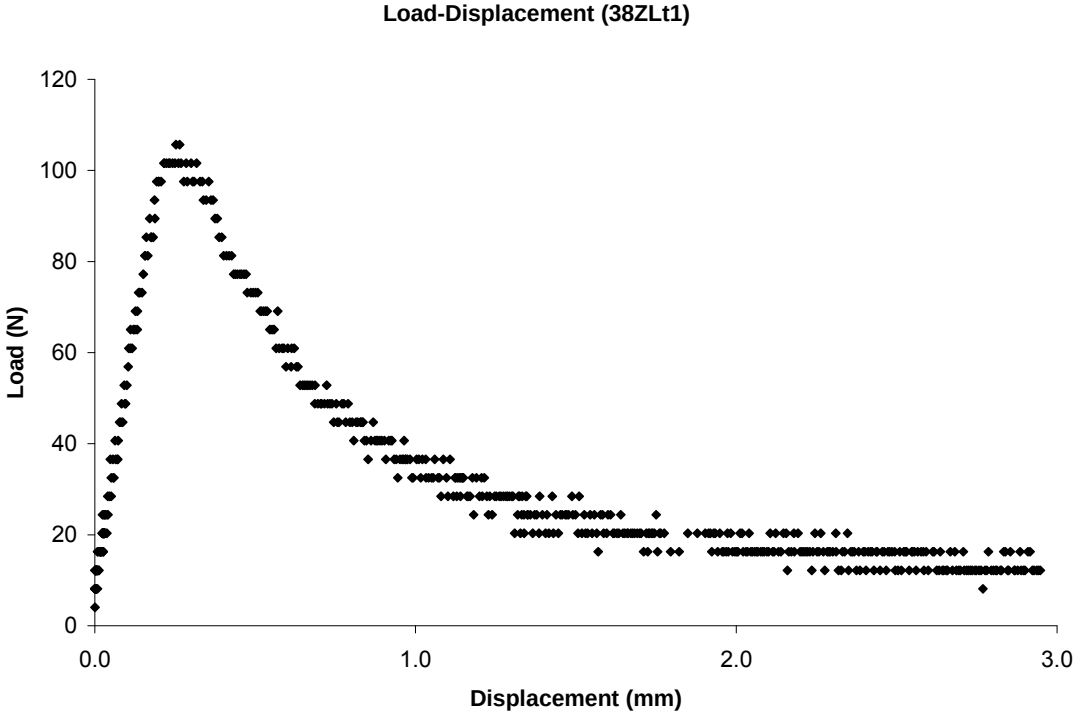

Figure B12. Load-displacement curve (38ZLt1)

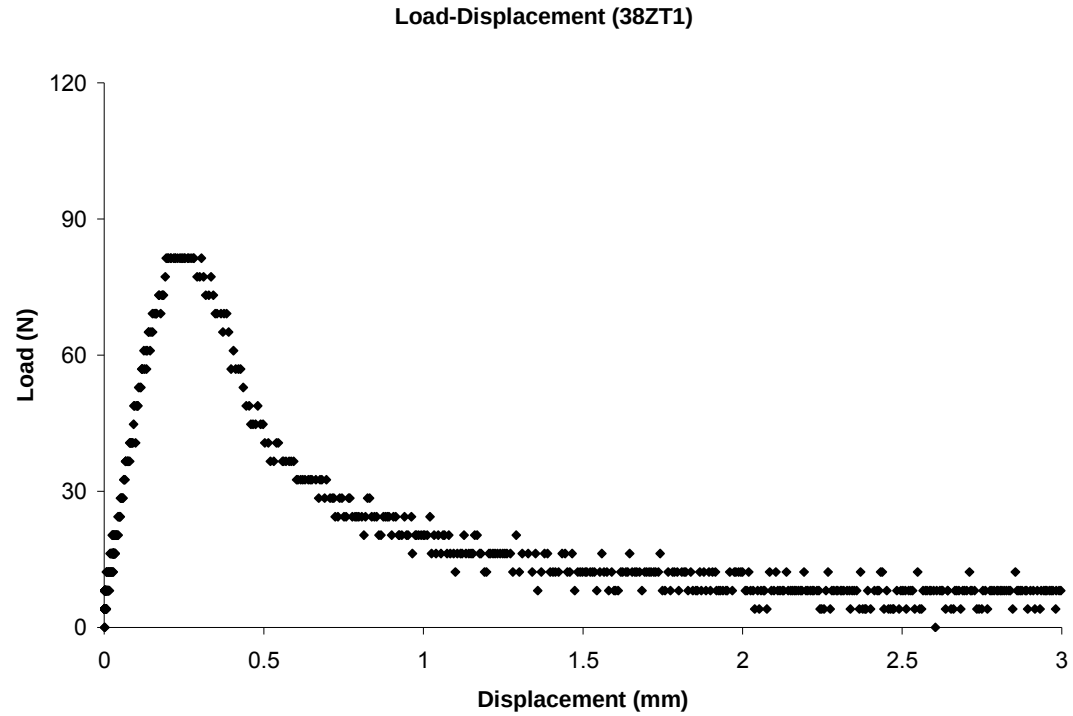

Figure B13. Load-displacement curve (38ZT1)

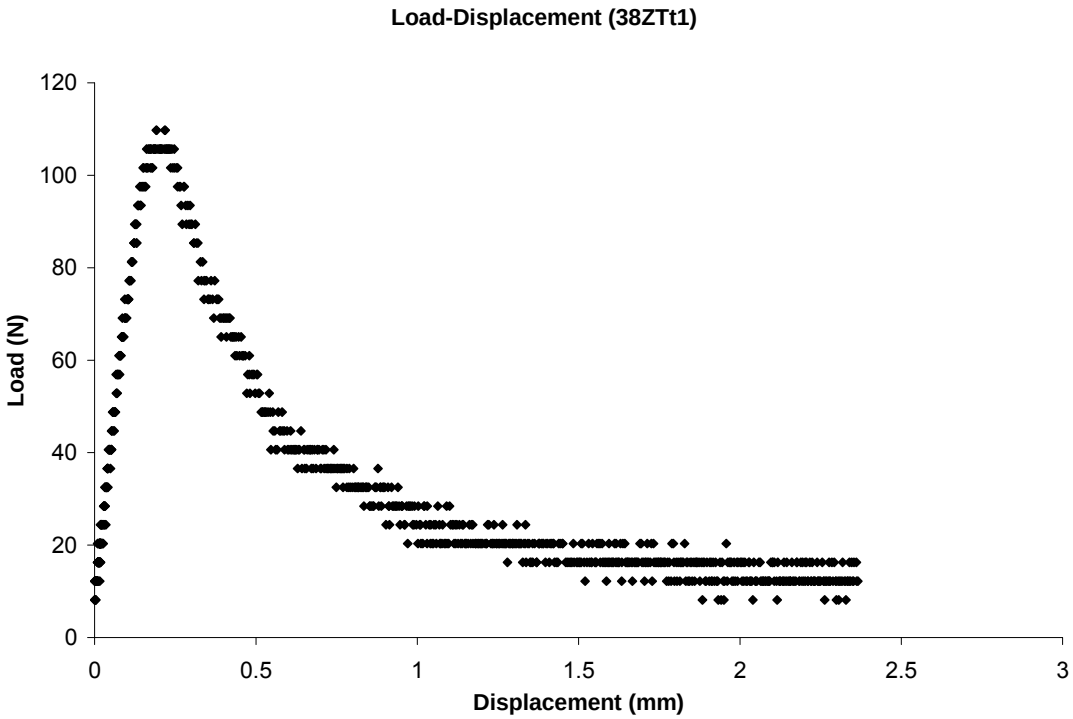

Figure B14. Load-displacement curve (38ZTt1)

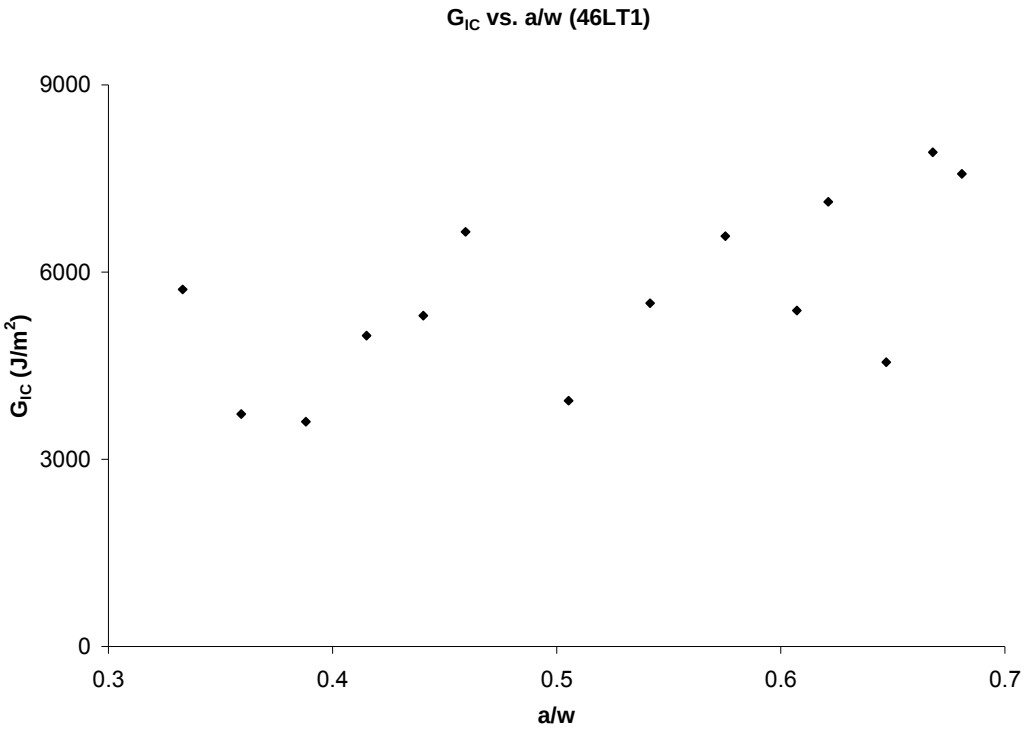

Figure B15. G_{IC} vs. a/w (46LT1)

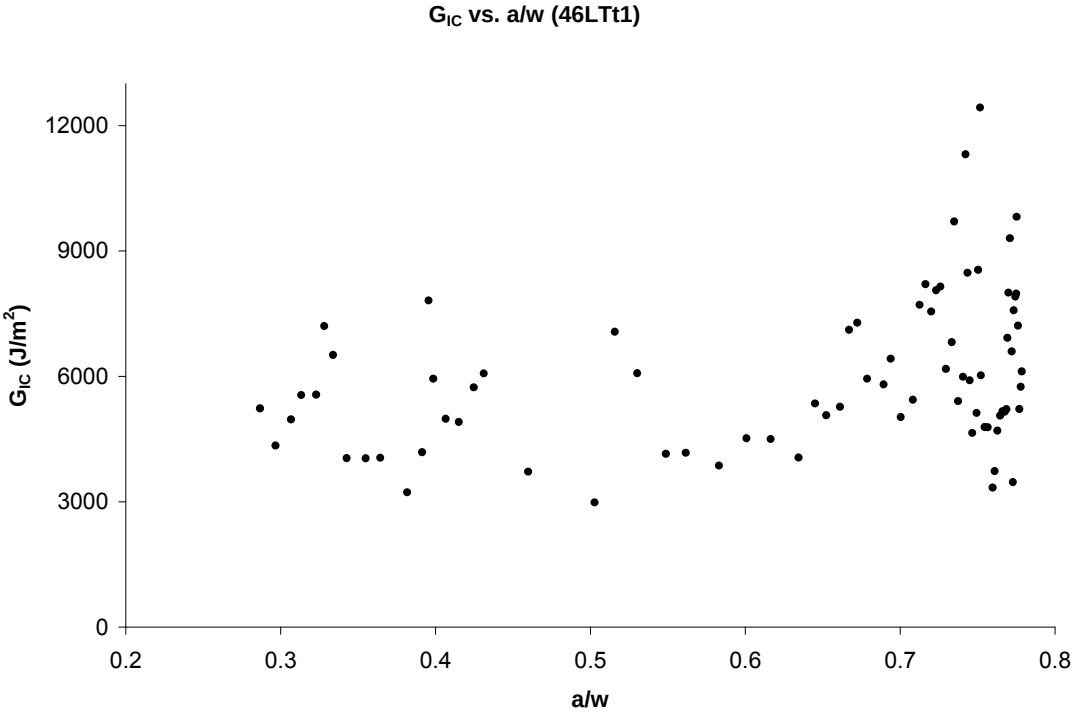

Figure B16. G_{IC} vs. a/w (46LTt1)

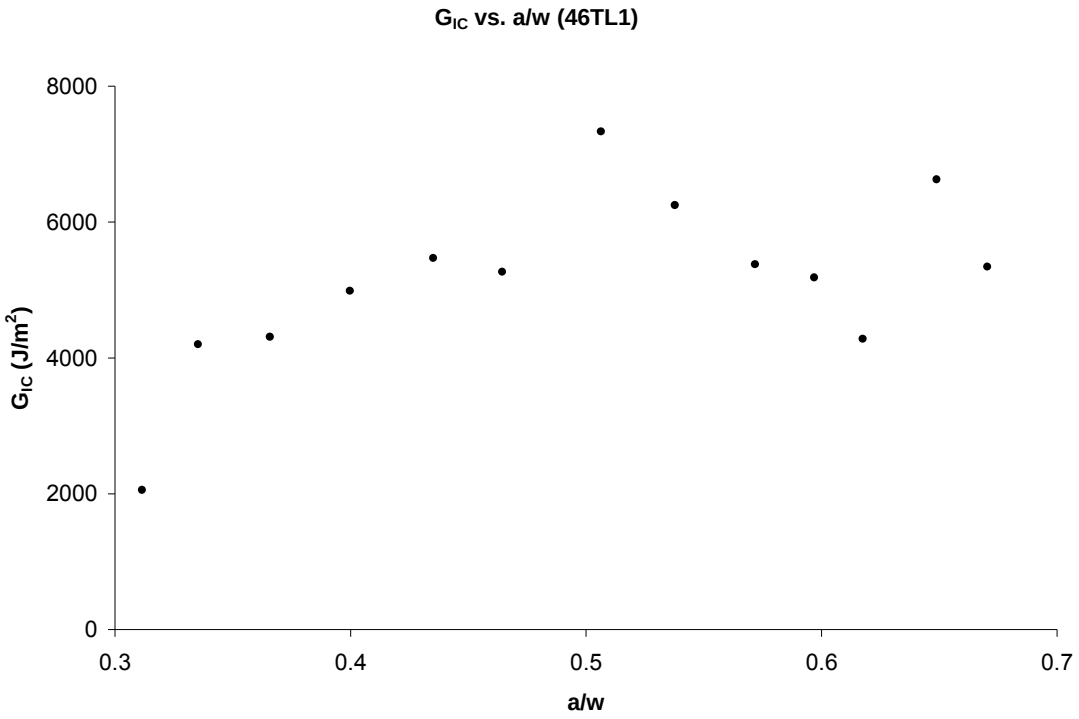

Figure B17. G_{IC} vs. a/w (46TL1)

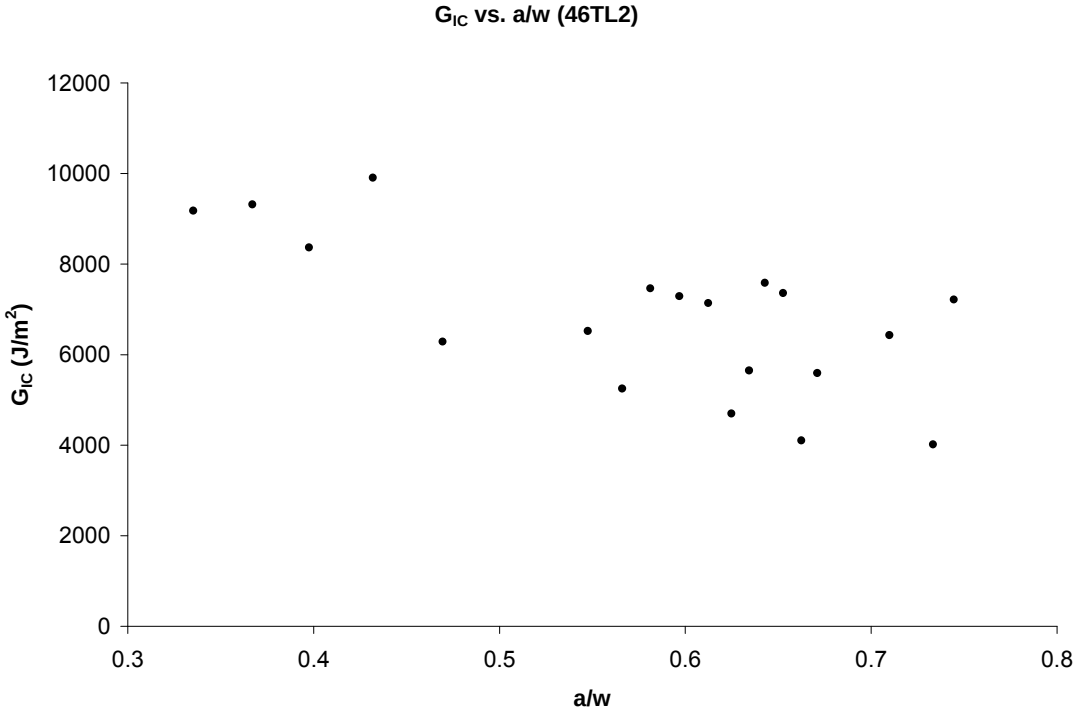

Figure B18. G_{IC} vs. a/w (46TL2)

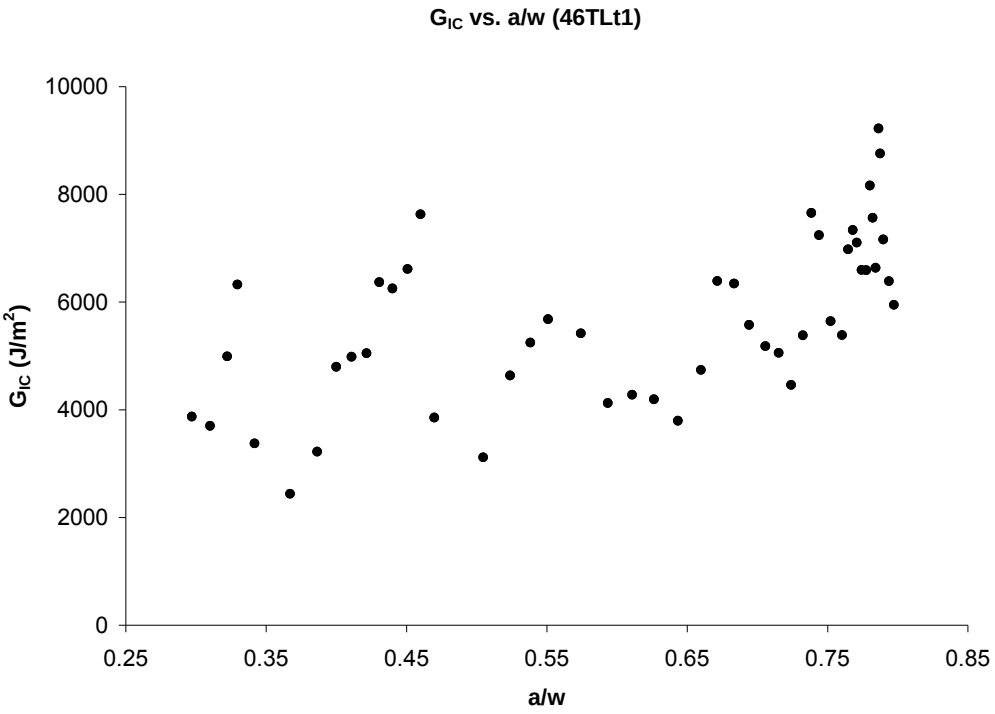

Figure B19. G_{IC} vs. a/w (46TLt1)

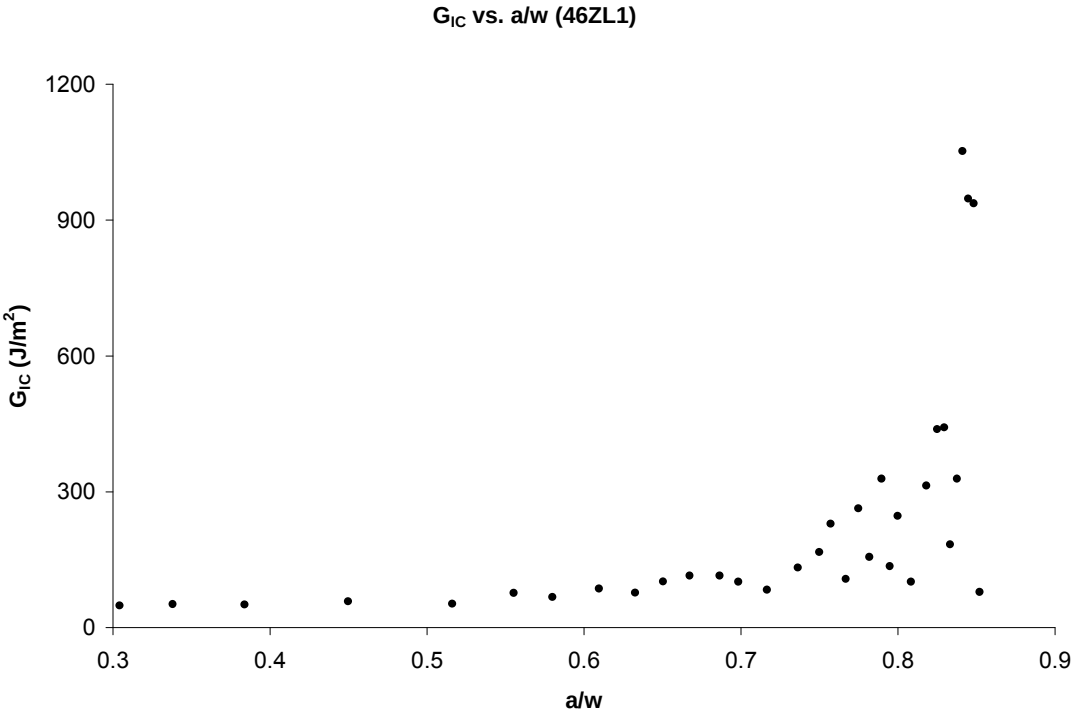

Figure B20. G_{IC} vs. a/w (46ZL1)

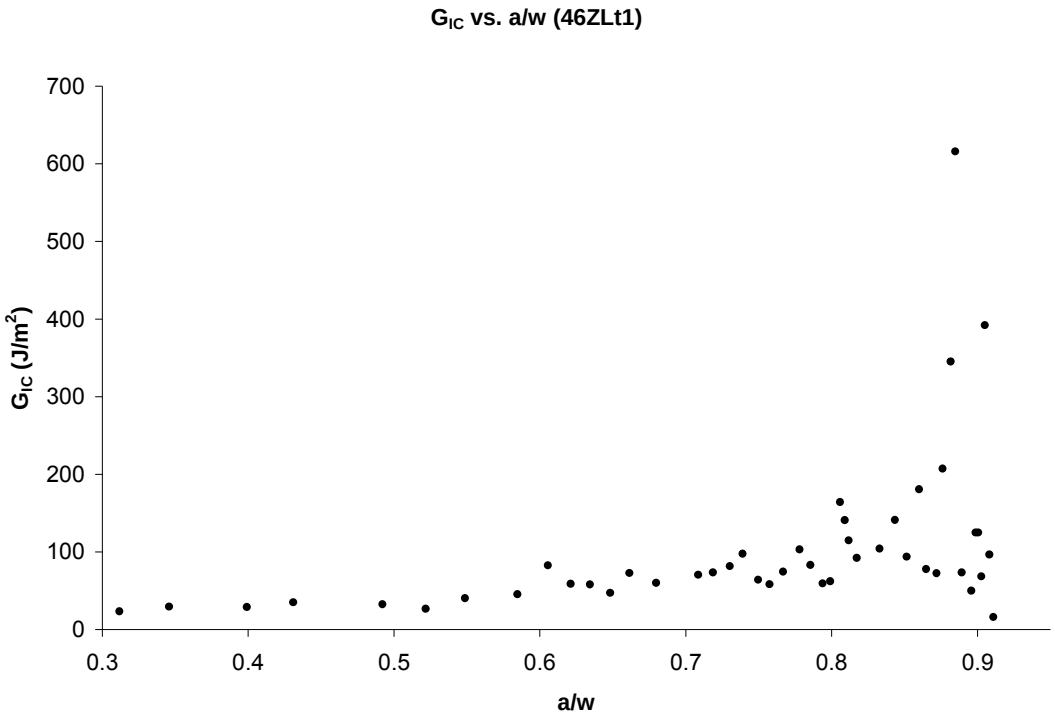

Figure B21. G_{IC} vs. a/w (46ZLt1)

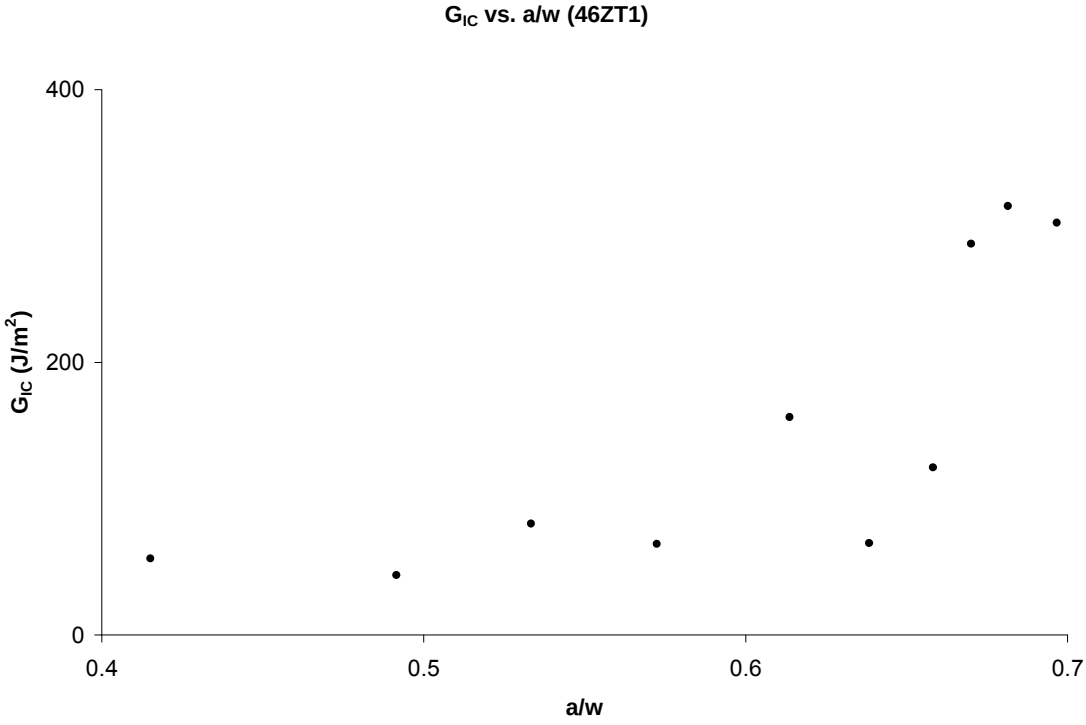

Figure B22. G_{IC} vs. a/w (46ZT1)

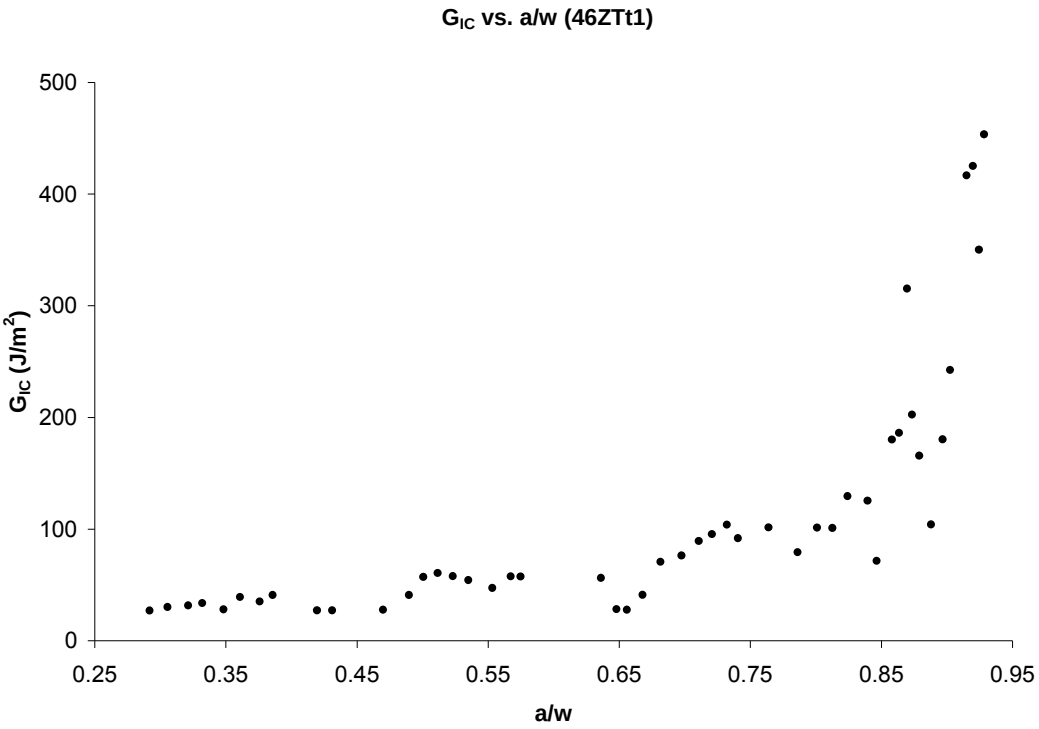

Figure B23. G_{IC} vs. a/w (46ZTt1)

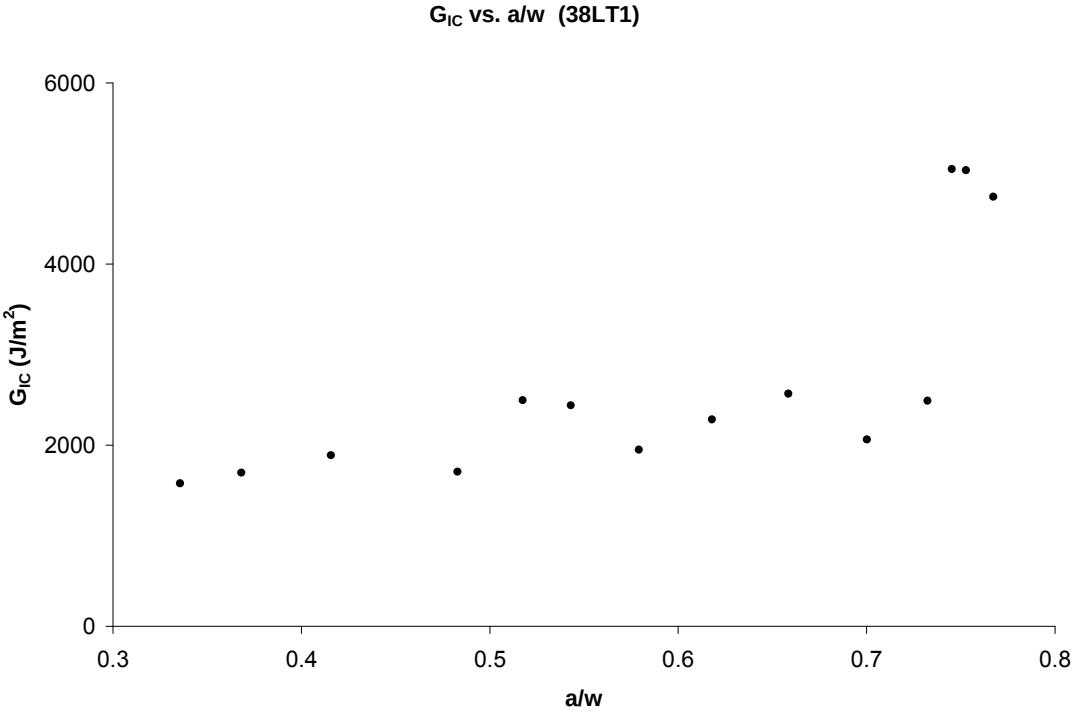

Figure B24. G_{IC} vs. a/w (38LT1)

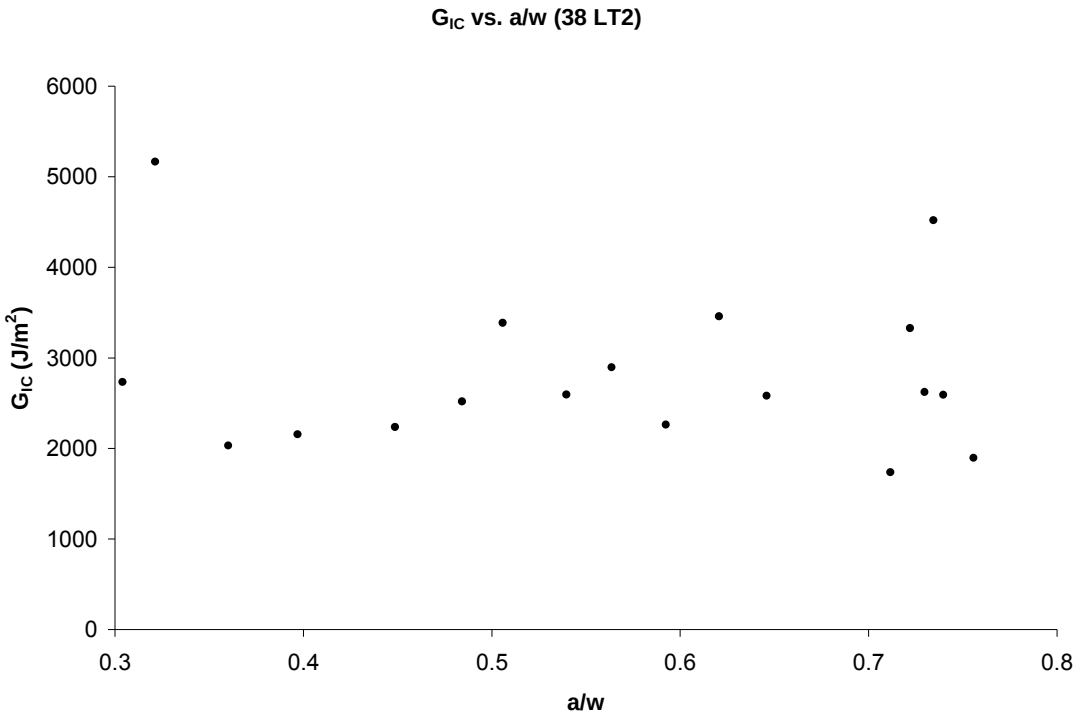

Figure B25. G_{IC} vs. a/w (38LT2)

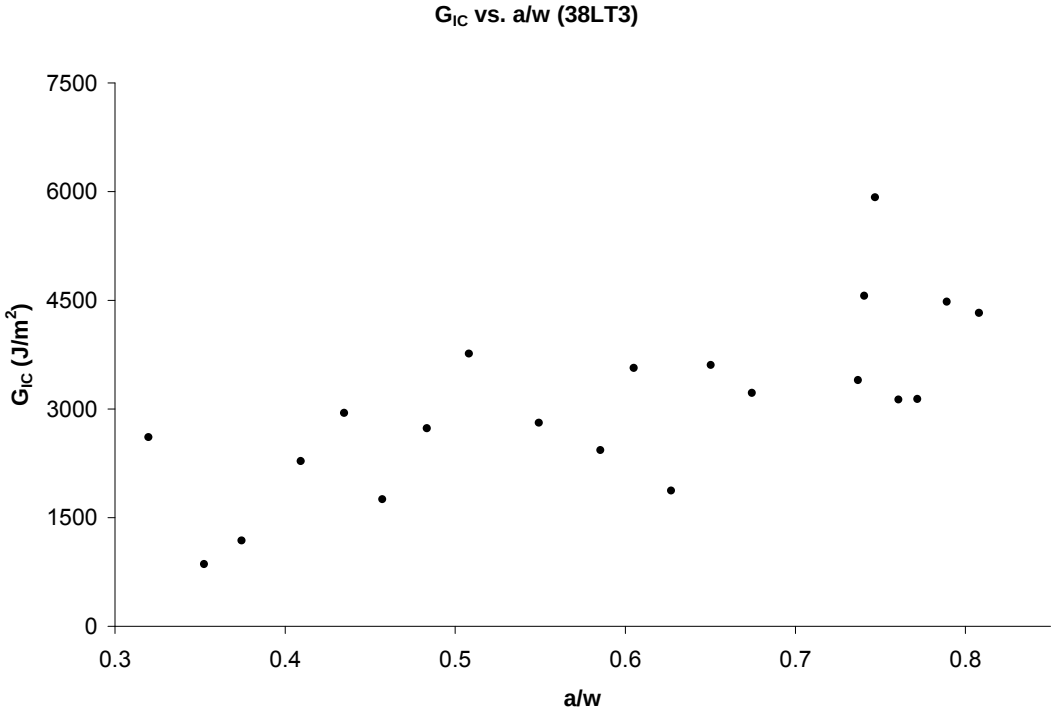

Figure B26. G_{IC} vs. a/w (38LT3)

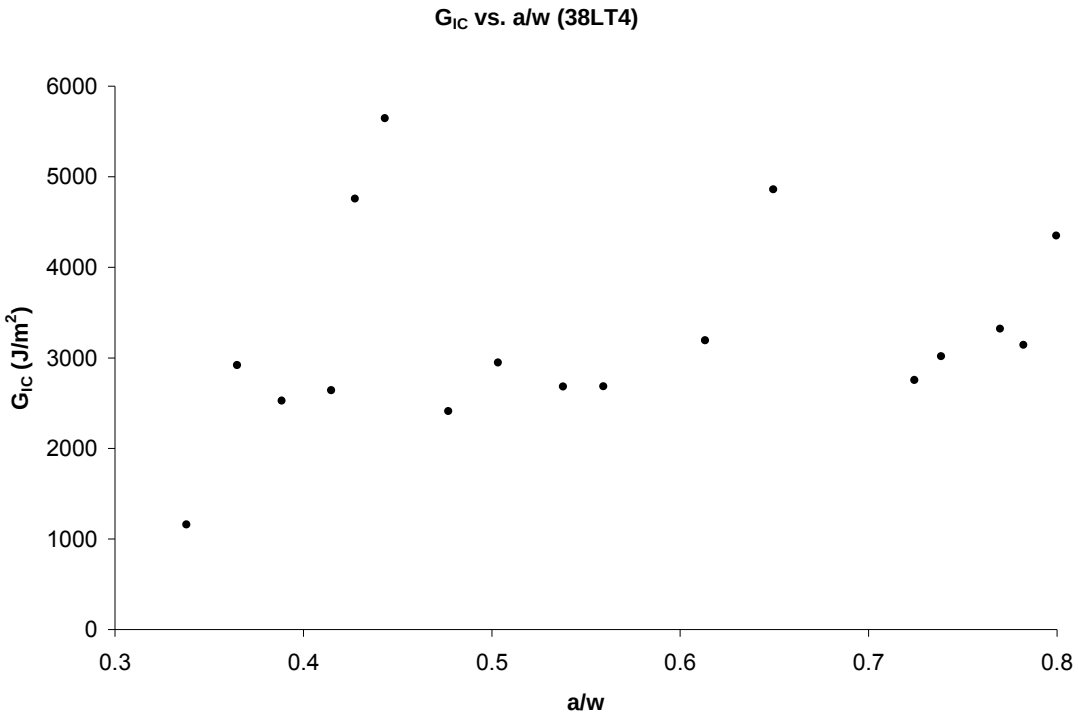

Figure B27. G_{IC} vs. a/w (38LT4)

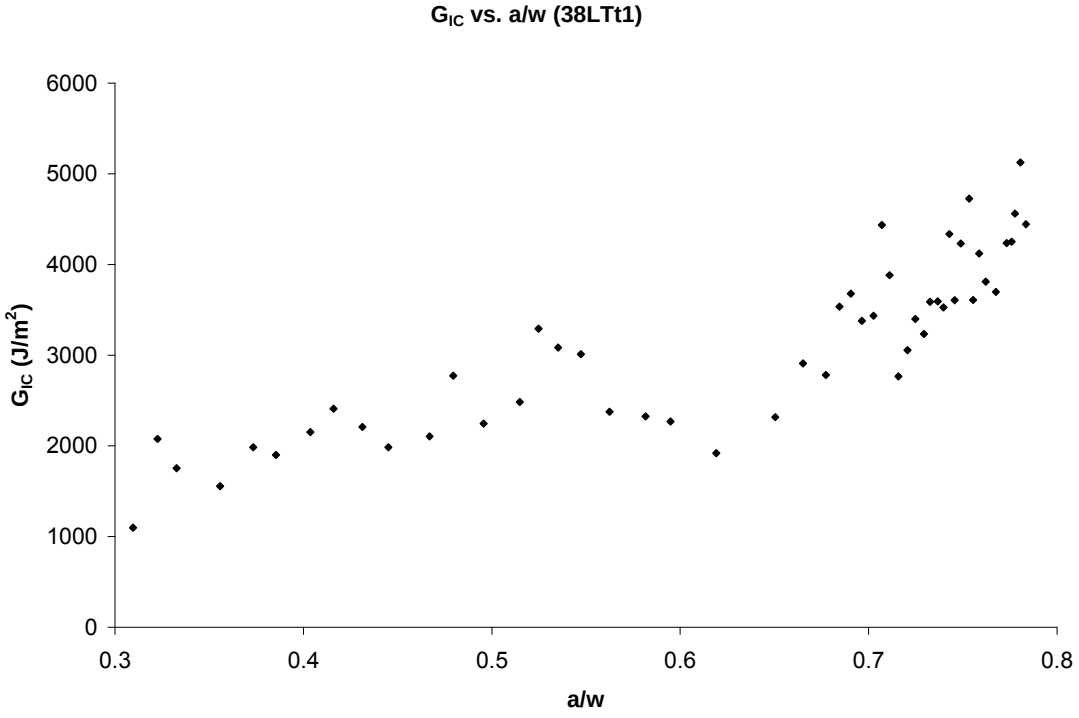

Figure B28. G_{IC} vs. a/w (38LTt1)

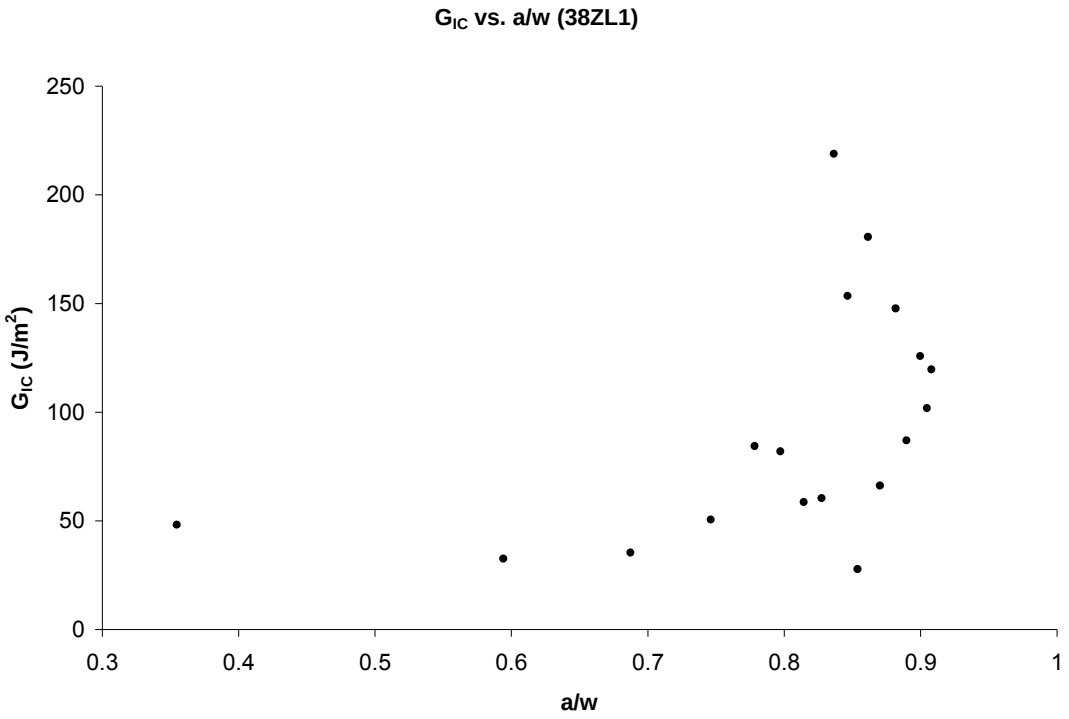

Figure B29. G_{IC} vs. a/w (38ZL1)

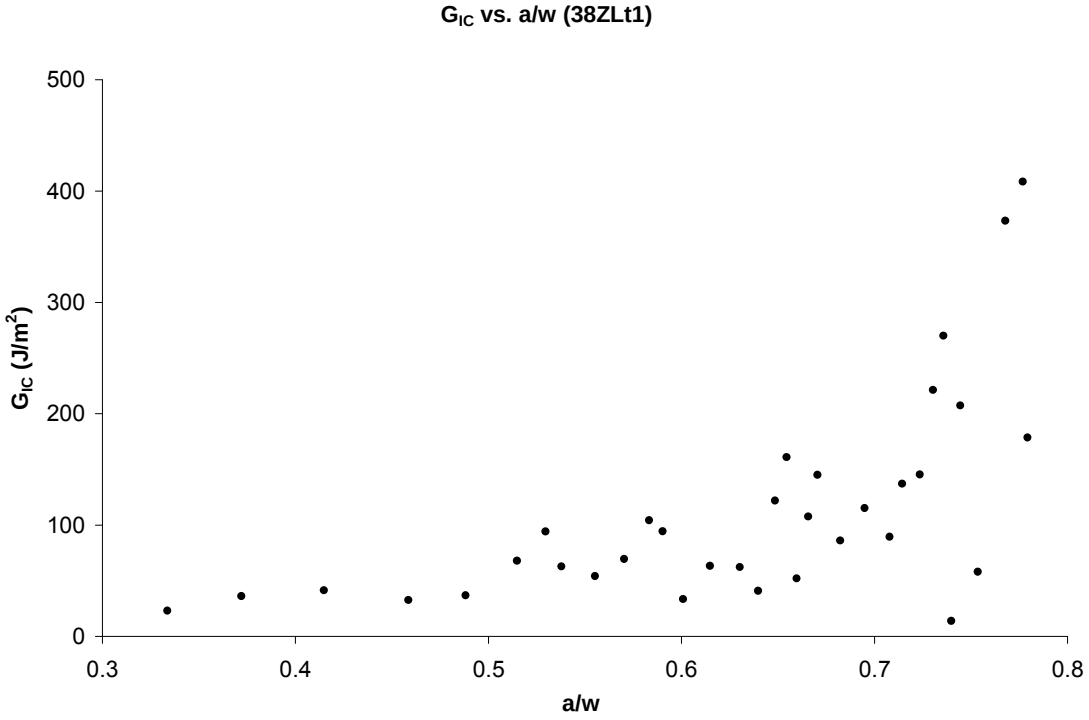

Figure B30. G_{IC} vs. a/w (38ZLt1)

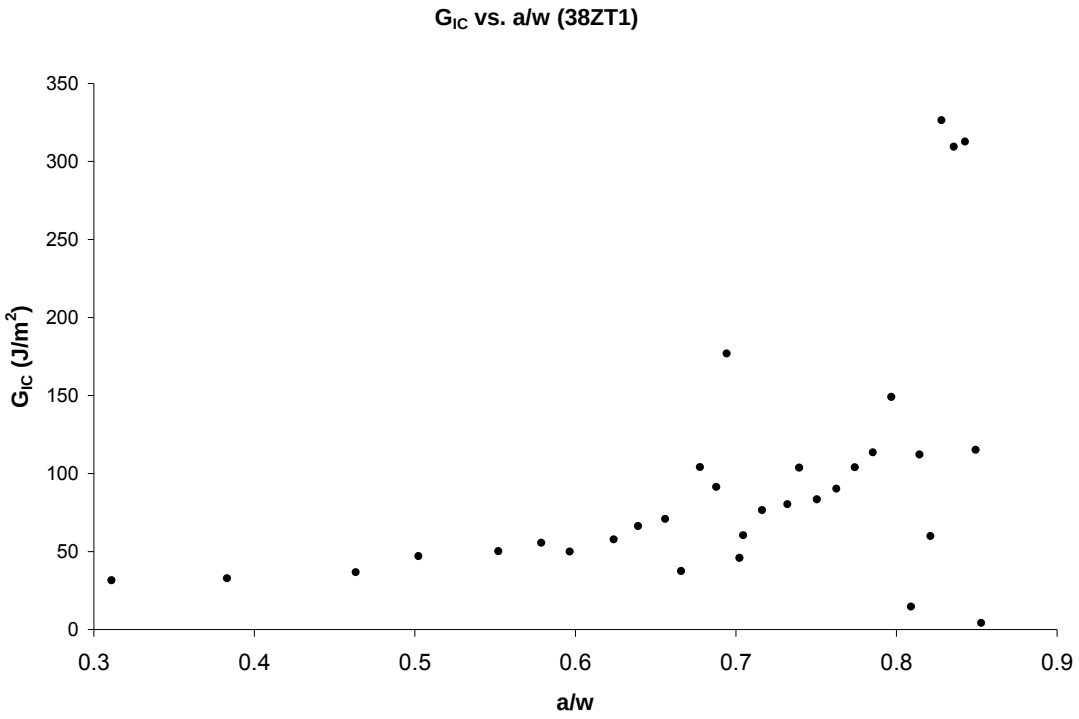

Figure B31. G_{IC} vs. a/w (38ZT1)

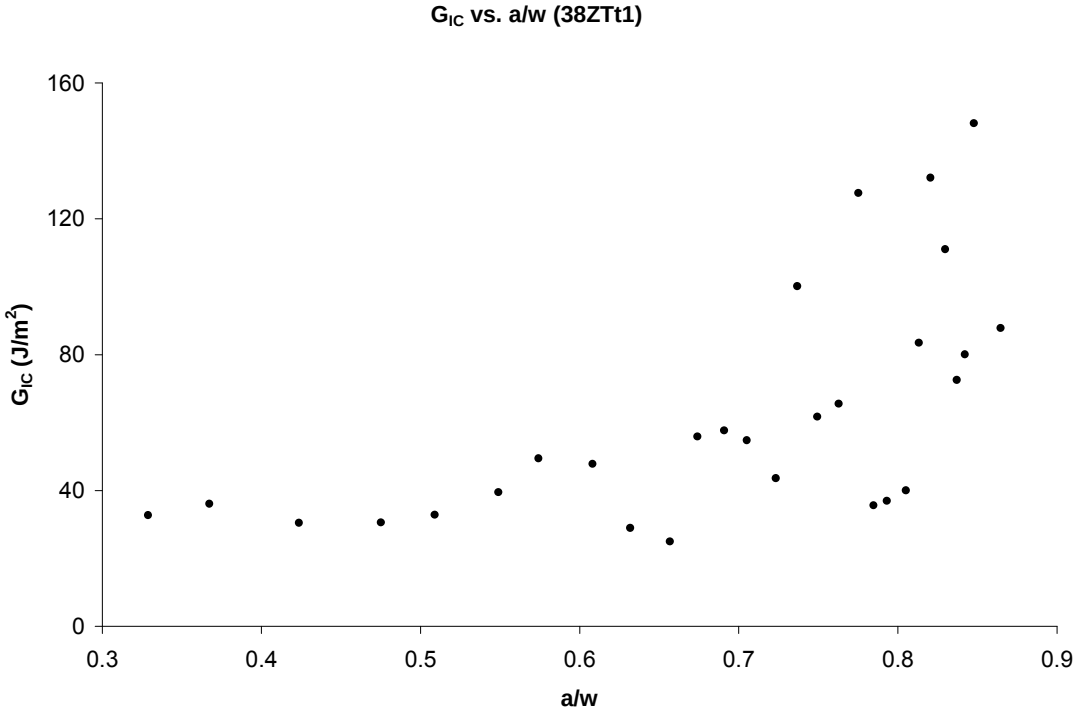

Figure B32. G_{IC} vs. a/w (38ZTt1)

Appendix C: Numerical Approach

Calibration Function for Extended Compact Tension Specimen (from FEA)

$$Y(a/w) = 7.55 - 33.67\frac{a}{w} - 49.23\left(\frac{a}{w}\right)^2 - 38.67\left(\frac{a}{w}\right)^3 + 137.35\left(\frac{a}{w}\right)^4$$

Calibration Functions for ASTM E399 Compact Tension Specimen

ASTM E399 (2006)

$$Y(a/w) = \frac{\left(2+\frac{a}{w}\right)\cdot\left[0.886 + 4.64\cdot\left(\frac{a}{w}\right) - 13.32\left(\frac{a}{w}\right)^2 + 14.72\left(\frac{a}{w}\right)^3 - 5.6\left(\frac{a}{w}\right)^4\right]}{\left(1-\frac{a}{w}\right)^{3/2}\cdot\left(\frac{a}{w}\right)^{1/2}}$$

Note:

$$f(a/w) = Y(a/w)\cdot\left(\frac{a}{w}\right)^{1/2}$$

Knott (1973)

$$Y(a/w) = 29.6 - 185.5\cdot\left(\frac{a}{w}\right) + 655.7\cdot\left(\frac{a}{w}\right)^2 - 1017\cdot\left(\frac{a}{w}\right)^3 + 638.9\cdot\left(\frac{a}{w}\right)^4$$

From FEA approach used

$$Y(a/w) = -17.62 + 173.51\cdot\left(\frac{a}{w}\right) - 356.4\left(\frac{a}{w}\right)^2 + 232.43\left(\frac{a}{w}\right)^3 + 69.45\left(\frac{a}{w}\right)^4$$

Table C1. ASTM CT specimen strain energies (from FEA) as a function of crack length (*a/w*), corresponding compliance, change in compliance and associated value of calibration function.

a/w	*From FEA Strain Energy x10^{-3} (J)	Compliance x10^{-4} (mm/N)	dc/da x10^{-6}(m/N)	FEA *Y(a/w)*
0.275	7.05	4.82	1.48	9.394
0.314	8.15	5.57	2.13	10.537
0.367	9.98	6.82	2.68	10.935
0.400	11.40	7.80	3.12	11.312
0.406	11.70	8.00	3.22	11.405
0.459	14.60	10.00	4.34	12.446
0.498	17.50	10.19	5.51	13.463
0.537	21.10	14.40	7.07	14.686
0.564	24.10	16.50	8.45	15.674
0.590	27.70	18.90	10.20	16.864
0.616	32.10	22.00	12.60	18.325
0.629	34.70	23.70	14.10	19.180
0.642	37.60	25.70	15.90	20.127
0.669	44.60	30.50	20.30	22.330
0.695	53.50	36.60	26.50	24.982
0.721	65.30	44.60	34.80	28.116
0.747	81.20	55.50	46.00	31.755
0.774	103.00	70.60	60.90	35.908
0.800	135.00	92.50	80.40	40.580
0.826	184.00	126.00	106.00	45.772
0.852	262.00	179.00	138.00	51.483
0.879	398.00	272.00	179.00	57.711
0.905	666.00	455.00	229.00	64.452

*E = 2300 MPa ,v = 0.33 and *thickness* = 12.7 mm, P = 171.07 N

Table C2. Extended CT specimen strain energies (from FEA) as a function of crack length (*a/w*), corresponding compliance, change in compliance and associated value of calibration function.

a/w	*From FEA Strain Energy $x10^{-3}$(J)	Compliance $x10^{-4}$(mm/N)	dc/da $x10^{-3}$(mm/N)	FEA Y(a/w)
0.185	2.90	1.99	1.26	10.59
0.194	6.46	4.41	1.53	11.37
0.222	7.24	4.95	2.13	12.54
0.231	7.53	5.15	2.28	12.71
0.240	7.84	5.36	2.41	12.83
0.259	8.50	5.81	2.66	12.97
0.268	8.85	6.05	2.77	13.01
0.282	9.42	6.44	2.94	13.07
0.287	9.61	6.57	3.00	13.09
0.305	10.40	7.13	3.24	13.18
0.324	11.30	7.75	3.50	13.31
0.342	12.30	8.42	3.79	13.48
0.361	13.40	9.15	4.12	13.69
0.379	14.60	9.95	4.49	13.93
0.398	15.80	10.80	4.89	14.20
0.416	17.20	11.70	5.33	14.48
0.435	18.70	12.80	5.81	14.79
0.453	20.30	13.90	6.32	15.12
0.472	22.10	15.10	6.89	15.47
0.491	24.00	16.40	7.51	15.84
0.509	26.10	17.80	8.21	16.25
0.528	28.40	19.40	9.00	16.72
0.546	31.00	21.20	9.92	17.25
0.565	33.80	23.10	11.00	17.88
0.583	37.00	25.30	12.30	18.60
0.602	40.50	27.70	13.90	19.45
0.620	44.50	30.40	15.80	20.45
0.639	49.10	33.50	18.20	21.61
0.657	54.40	37.20	21.10	22.94
0.676	60.50	41.30	24.70	24.45
0.694	67.70	46.30	29.00	26.16
0.713	76.40	52.20	34.30	28.07
0.731	86.80	59.30	40.70	30.19
0.750	99.70	68.10	48.40	32.51
0.768	116.00	79.20	57.50	35.03
0.787	136.00	93.30	68.50	37.76
0.805	164.00	112.00	81.40	40.70
0.824	200.00	137.00	96.60	43.84
0.843	250.00	171.00	114.00	47.18
0.861	323.00	221.00	135.00	50.71

*E = 2300 MPa ,v = 0.33 and *thickness* = 12.7 mm, P = 171.07 N